Institute of Nuclear Physics

Master's Thesis

Partial Wave Analysis of f_J-Resonances via the $\phi\pi\pi$ Final State in $\psi(2S)$ Decays at BESIII

Nikolai in der Wiesche

First Supervisor: Apl. Prof. Dr. Alfons Khoukaz
Second Supervisor: Prof. Dr. Anton Andronic

March 2, 2023

»To raise new questions, new possibilities, to regard old problems from a new angle, requires creative imagination and marks real advance in science.«

Albert Einstein

Contents

1. Introduction

The desire to research particle physics is the desire to understand the most fundamental laws of this universe that govern everything that we experience. To gain insight into these secrets, particle physics uses the philosophical approach of Reductionism, the idea that everything can be reduced to a set of elementary pieces. This way of thinking is not new, in fact, records can be found dating it back to the ancient Greeks [1]. Recapitulating all the discoveries that led to our current understanding of particle physics would certainly be insightful, but make this more of a thesis in history, than a physics one. Therefore, the next paragraph will only focus one some of the fundamental discoveries of the last centuries, which formed our current understanding of particle physics, and laid the foundation for this thesis.

A major contribution to the foundation of modern particle physics was made by J.J. Thompson, which in 1897 discovered very light, negatively charged particles in cathode rays, he called "corpuscles" [2]. These "corpuscles" would later more commonly be called electrons, and their discovery would mark the first observation of what is today understood as an elementary particle. Seven years later, in 1904 Thompson proposed the "plum pudding model" [3], which, for the first time, described the substructure of the atom, and predicted the electron as the first subatomic particle. To further research the substructure of the atom, between 1908 and 1913, H. Geiger and E. Marsden measured the scattering angle of ionized Helium atoms, also called α particles, which were shot onto a thin gold foil, under the supervision of E. Rutherford. In 1911, E. Rutherford used this scattering data to disprove Thompson's model, and postulated his own model, describing the atom as a very small, charged nucleus, which is orbited by electrons [4]. Later, he would also prove, that the nucleus of the hydrogen atom is present in other nuclei, calling the hydrogen nucleus proton [5]. Similar kinds of collision experiments would later become a staple for the investigation of the substructure of particles and lay the foundation for the methods used in this work. By shooting α particles onto Beryllium and measuring the resulting γ rays, J. Chadwick discovered a neutral constituent of the nucleus with about the mass of the proton, which he called neutron in 1932 [6], thus gaining further insights into the substructure of the nucleus. The proton and neutron are the first observations, which would be later classified as hadronic matter, but their composition and interaction were still unknown. To explain their interaction, in 1934, H. Yukawa proposed a new type of massive

matter, the meson, which in his model mediated a strong short-ranged force, later called the strong force, that binds the protons and neutrons together in the nucleus [7]. His predicted meson, which would later be called pion, was discovered in 1947 by C. Lattes et al. using the photo emulsion method [8]. Over the following years, further new particles were found, like the kaon, first seen by G. Rochester and C. Butler in 1947 [9] and lambda, discovered by V. D. Hopper and S. Biswas in 1950 [10]. Both of these particles could be easily produced as pairs by particle collisions but decayed much slower than expected. To explain this strange behavior, both M. Gell-Mann [11], and T. Nakano together with K. Nishijima [12] published papers independent from each other in 1953, postulating a new charge-like quantum number, called strangeness, which was conserved in the production of the strange particles, but not in their decay. As the next step to understand the new particles that were experimentally discovered, Gell-Mann, in 1961, proposed the "eightfold way" for the classification of particles with identical spin [13], which he extended in 1964 to the quark model using group theory [14]. The model suggests a triplet consisting of spin 1/2 particles, called quarks, and a triplet of their anti-matter with opposite charge-like quantum numbers, called anti-quarks. Using this model, the easiest way to construct bound states is to multiply both triplets, making quark anti-quark states called mesons, or to multiply three times the same triplet, leading to states either consisting of three quarks, or three anti-quarks, called (anti-)baryons. Initially, the quark triplet was introduced only as a tool to use group theory for the description of the observed particles, but over time became more and more established as the elementary particles as which they are known today. Then, in November 1974, the groups of B. Richter at the Stanford Linear Accelerator Center and S.C.C. Ting at the Brookhaven National Laboratory independently from each other observed an extremely narrow resonance at a mass of about 3.1 GeV [1] [15, 16]. In the publication of Ting the new resonance was called J, while the group of Richter chose the name ψ, leading to the commonly used name J/ψ for the particle. Due to the high mass of the J/ψ and its strong coupling to electromagnetic decays into leptons, it was interpreted as a bound state of two new quarks, the charm, and the anti-charm quark, confirming the existence of a fourth quark flavor as predicted by B.J. Bjørken and S.L. Glashow in 1964 [17]. Its discovery triggered the so called "November Revolution" of particle physics, leading to the discovery of numerous further hadrons containing charm quarks, and significantly contributed to the creation of the standard model, that describes particle physics as we know it today.

Until this date states consisting of a charm and an anti-charm quark, called charmonia, play a significant role for the research in particle physics. A major contributor to this research is the BESIII Collaboration, which was established in 2005 and now includes 89 scientific institutes from around the world [18]. At the heart of the collaboration is the eponymous Beijing spectrometer III (BESIII) experiment, located at the Beijing electron positron collider II (BEPCII) in China. BEPCII facilitates e^+e^- collisions at center-of-mass energies between 2−5 GeV [19] allowing for in-depth analyses of the charmonium and light-quark regions. Over

[1] Throughout this thesis, natural units ($c = \hbar = 1$) are used.

the last 15 years the BESIII collaboration collected data in this energy region and acquired the world's largest J/ψ and $\psi(2S)$ data sets. The charmonium $\psi(2S)$ is the first excitation of the J/ψ meson with a mass of about 3686 MeV, which can, similar to the J/ψ directly be produced in electron positron collisions.

For this work, about 2.3 billion events of the BESIII $\psi(2S)$ data set were used to gain further insight into the physical properties of the f_0 resonances at masses up to 2 GeV. These f_0 states are characterized by their isospin and total angular momentum of zero, as well as their positive parity and charge conjugation quantum numbers. The existence of what is known today as the $f_0(500)$ was already predicted as early as 1955 [20], but to this day its true nature is controversial, and its physical properties have only been determined with great uncertainties (cf. Ref. [21]). For the other f_0 resonances, namely the $f_0(980)$, $f_0(1370)$, $f_0(1500)$, and $f_0(1710)$ the situation is similar, making an analysis of f_0 states more than worthwhile, but anything but trivial. Due to their broad width, overlapping line shapes and positions at multiple production thresholds of their possible decay channels, sophisticated analysis methods using high statistics data are necessary, with models that account for analyticity and unitarity. Another aspect that makes the analysis of these states even more interesting, and equivalently more challenging, is their unknown substructure. Mixing with non-conventional hadrons, so-called exotic states, is predicted for all five f_0 states. Both the $f_0(500)$ and $f_0(980)$ are discussed to mix with states consisting of four bound quarks [22], or two bound mesons [23]. It is also strongly suggested that the rest of the mentioned f_0 states mix with the lightest glueball [24]. These glueballs are bound states of gluons, the elementary particles that mediate the strong interaction, which have the property of coupling themselves to the strong interaction. Learning more about these resonances, and consequently more about the strong interaction that governs the construction of these states, is the motivation for this work.

The analysis presented in this work can be divided into two parts. In the first part, events from the $\psi(2S)$ data set will be selected, that contain the signal reaction $\psi(2S) \to (\phi \to K^+K^-)\pi\pi$ with $\pi\pi$ being either $\pi^+\pi^-$, or $\pi^0\pi^0$. During the selection process, it will be possible to determine the branching ratio for the yet unlisted reaction $\psi(2S) \to \phi\pi^0\pi^0$, as well as determining a value with less uncertainty for the already measured branching ratio of $\psi(2S) \to (\phi \to K^+K^-)\pi^+\pi^-$. Resulting from the choice of the signal reactions, only f_J states can appear as the intermediate resonance of the $\pi\pi$ system, with $J = 0, 2, 4, ...$ being the total angular momentum of the states, thus including the desired f_0 resonances. Another feature of this approach is that states with high strange quark content are preferably produced as intermediate resonances, resulting from the large strangeness content of the ϕ meson. These selection criteria will yield $\pi\pi$ invariant mass spectra with enough statistics for further analysis of the f_0 resonances.
In the second part, a model based on scattering theory will be implemented to describe the complete signal reaction. To simplify the complex problem of finding a function that is able to describe the whole process, the reaction will be decomposed into a sum of its partial waves

[25]. For the description of the $\pi\pi$ invariant mass spectra, the so-called K-matrix parameterization will be used [26], allowing for a unitary and analytical incorporation of f_0 resonances into the model. With the information provided by the model, it will then be possible to gain further insights into the properties and inner structure of the f_0 states.

2. Standard Model of Particle Physics

This chapter starts with a general description of the standard model of particle physics, and then goes more into detail covering mesons and exotic states, with their corresponding quantum numbers. The goal of these sections is to give a clear motivation for researching light meson resonances and lay a foundation for the following analysis.

The standard model of particle physics unites the strong, weak, and electromagnetic interactions into one quantum field theory with the gauge group:

$$\mathrm{SU(3)_c} \times \mathrm{SU(2)_L} \times \mathrm{U(1)_Y}.$$

This product includes the color gauge symmetry $\mathrm{SU(3)_c}$, which is part of quantum chromodynamics (QCD) and describes the strong interaction. It also includes the weak isospin group $\mathrm{SU(2)_L}$ and the weak hypercharge group $\mathrm{U(1)_Y}$, which together describe the unified electroweak interaction [27, 28].
Three generations of fermions are included in the standard model, each generation consisting of two quarks and two leptons, as well as their anti-particles, which have the same mass, but opposite charge-like quantum numbers. Quarks couple to all three interactions, while leptons only couple to the weak and electromagnetic interaction. Also included in the model are the gauge bosons and Higgs boson, resulting from its construction as a gauge theory with spontaneous symmetry breaking. These gauge bosons function as force carriers for the three interactions. Photons are the force carrier of the electromagnetic interaction, the Z^0, $W^\pm$ bosons carry the weak interaction, and eight gluons carry the strong interaction. There is only one scalar boson, the Higgs, which is an excitation of the Higgs field, giving mass to all charged elementary particles, and the Z^0 boson. All the particles mentioned before can be seen in Fig. 2.1 with their corresponding spin and electric charge [29].
The construction of the standard model results in nineteen free parameters. One way of assigning these parameters is as follows: One coupling constant for each interaction, one angle to describe CP-violation in the strong interaction, nine masses of the charged fermions, four mixing angles of the Cabibbo-Kobayashi-Maskawa matrix, which gives the strength of the quark-flavor changing weak interaction, one vacuum expectation value for the Higgs field, and one mass of the Higgs particle [27].

While this model has been remarkably successful in predicting the data collected by numerous experiments, there are still a lot of aspects that are not understood. Some examples would be the inclusion of gravity, the description of dark energy and dark matter, or an explanation for the baryon asymmetry in the universe [28, 29].
The standard model has become the motivation of many works in modern particle physics which e.g., try to determine its parameters, test its predictions and limits, and find theories that expand the model to include aspects that are currently not described. This work focuses on testing the prediction of QCD by investigating the properties of states bound by the strong interaction. For the classification of such bound states, the quark model is used, which will be introduced in the next section.

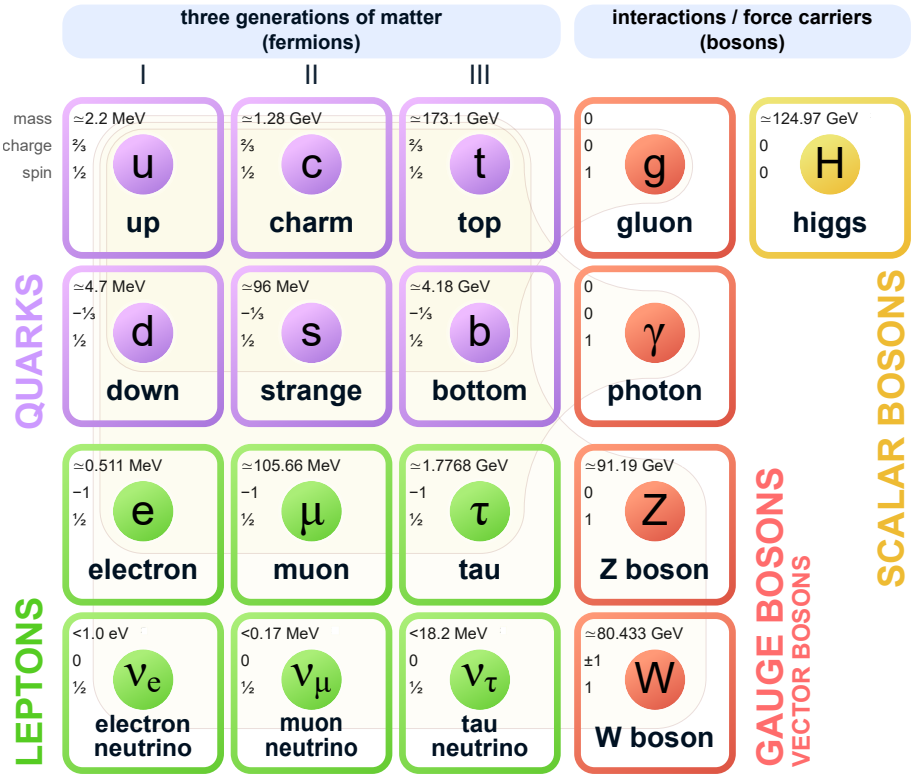

Figure 2.1: All elementary particles predicted by the standard model grouped into quarks, leptons, gauge bosons, and scalar bosons (excluding anti-particles). For each particle the spin, electric charge as well as their current estimated mass is given. The fermions are ordered in terms of their generation. Edited version of Ref. [30].

2.1 Quark Model

The quark model is used for the classification and description of states bound by the strong interaction consisting of quarks and gluons. As mentioned in the last section, QCD is the quantum field theory that describes the strong interaction. QCD has a SU(3) gauge symmetry corresponding to three colors, three anti-colors, and eight gluons. Quarks carry a color charge,

while anti-quarks carry an anti-color and gluons carry a color and an anti-color [31, Reviews Chapter 9]. Even if not explicitly included in the theoretical description of QCD, experimental results strongly imply that only color neutral states can exist freely. This phenomenon is called confinement [31, Reviews Chapter 15]. Color neutrality can be achieved by combining all three (anti-)colors, or by coupling a color and its anti-color. This concept is visualized in the upper half of Fig. 2.2.
With this restriction, it is now possible to construct strongly interacting bound states made of quarks and gluons, called hadrons. The construction and classification of these hadrons will be discussed in the next sections.

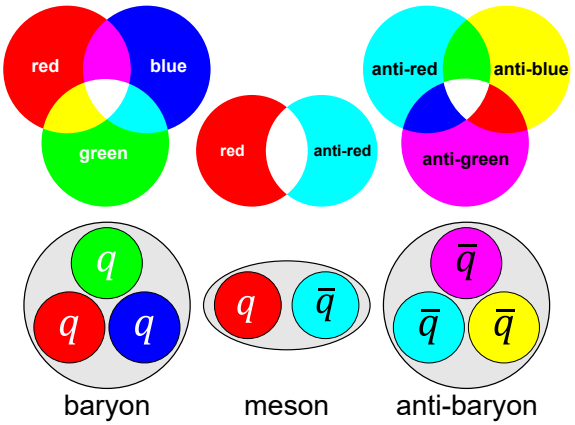

Figure 2.2: Visualization of the color charge (top) and the three easiest color neutral bound quark states (bottom). The combination of color charges is shown as the overlapping of the colored circles white being color neutral combinations.

2.2 Hadrons

Strongly interacting color neutral bound states made of quarks are called hadrons. The two easiest ways to combine quarks while respecting color neutrality are quark anti-quark ($q\bar{q}$) states, called mesons, and states made of three (anti-)quarks, called (anti-)baryons. A simple visualization of such states, only showing the so-called constituent quarks, can be seen in the lower half of Fig. 2.2. In the field of the strong interaction, which binds the constituent quarks, virtual quark anti-quark pairs are constantly created and annihilate each other. These so-called sea quarks and anti-quarks, together with the gluons, which mediate the interactions inside the hadrons, influence the mass, spin, momentum, and magnetic moment of hadrons. All charge-like quantum numbers of the hadrons only depend on their constituents. In addition to the electric charge and spin quantum numbers of the quarks, which can be seen in Fig. 2.1, all quarks by convention have a parity of $+1$ and a baryon quantum number of $+1/3$. All other flavor dependent quantum numbers are listed in Table 2.1 [32].
A majority of particles investigated in this work are mesons, therefore the next section will give a detailed description of their properties.

Table 2.1: Additive quantum numbers depending on the quark flavor according to [31, Summary Tables].

	d	u	s	c	b	t
I - isospin	1/2	1/2	0	0	0	0
I_z - isospin z-component	−1/2	1/2	0	0	0	0
S - strangeness	0	0	−1	0	0	0
C - charm	0	0	0	1	0	0
B - bottomness	0	0	0	0	−1	0
T - topness	0	0	0	0	0	1

2.3 Mesons

Mesons are often classified by their J^{PC} quantum numbers. J is the meson's total angular momentum quantum number, which depends on the orbital angular momentum quantum number l and the spin coupling quantum number s of their constituent quarks, and can take values in the following range:

$$|l - s| \leq J \leq |l + s|. \tag{2.1}$$

P is the eigenvalue of the parity operator, which changes the signs of the spatial coordinates of a state. All mesons are parity eigenstates, with their parity eigenvalue being defined as $P = (-1)^{l+1}$. C is the eigenvalue of the charge conjugation operator, which transforms a state into its anti-state. Only mesons that are their own anti-particle are eigenstates of the charge conjugation operator, and their eigenvalues can be written as $C = (-1)^{l+s}$ [32].
Often, in addition to the J^{PC} quantum numbers, the so called G-parity is defined as $G = (-1)^{I+l+s}$. It is a conserved property of mesons that are their own anti-particle, and of $u\bar{d}$ and $\bar{u}d$ states, given that isospin is conserved in the interaction. It is currently assumed, that parity and charge conjugation are conserved in the strong and electromagnetic interaction, while isospin is only approximately conserved in the strong interaction [31, Reviews Chapter 15].

2.3.1 Light Mesons

Light mesons are mesons only containing the three lightest quarks (u, d, s), and which can be grouped into nonets made out of a singlet and octet states [27]:

$$3 \otimes \bar{3} = 8 \oplus 1. \tag{2.2}$$

The pseudoscalar ($J^{PC} = 0^{-(+)}$), and vector ($J^{PC} = 1^{-(-)}$) meson nonets, containing the lightest mesons, can be seen in Fig. 2.3.

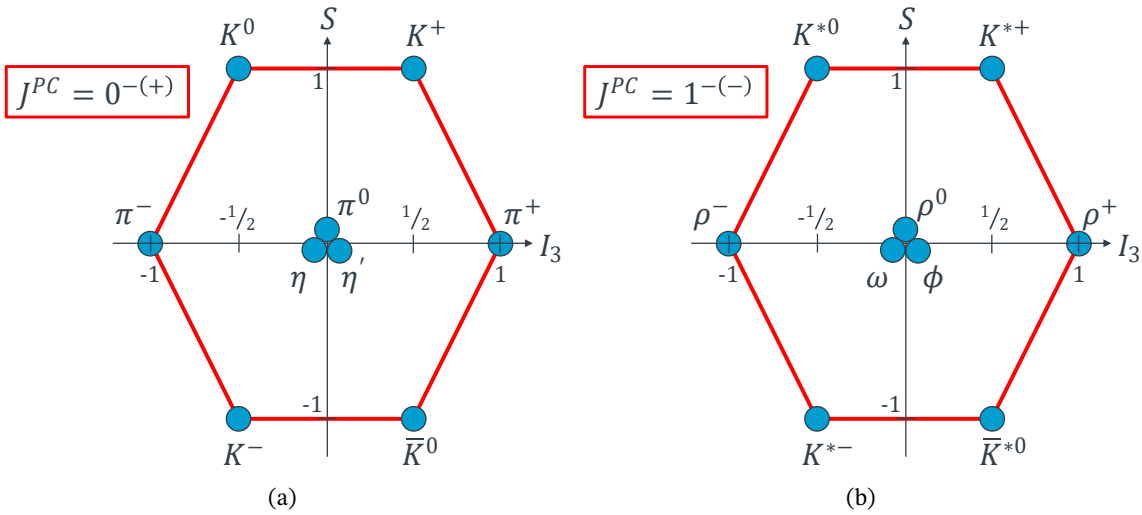

Figure 2.3: The pseudoscalar (a), and vector (b) meson nonet according to Ref. [31, Summary Tables].

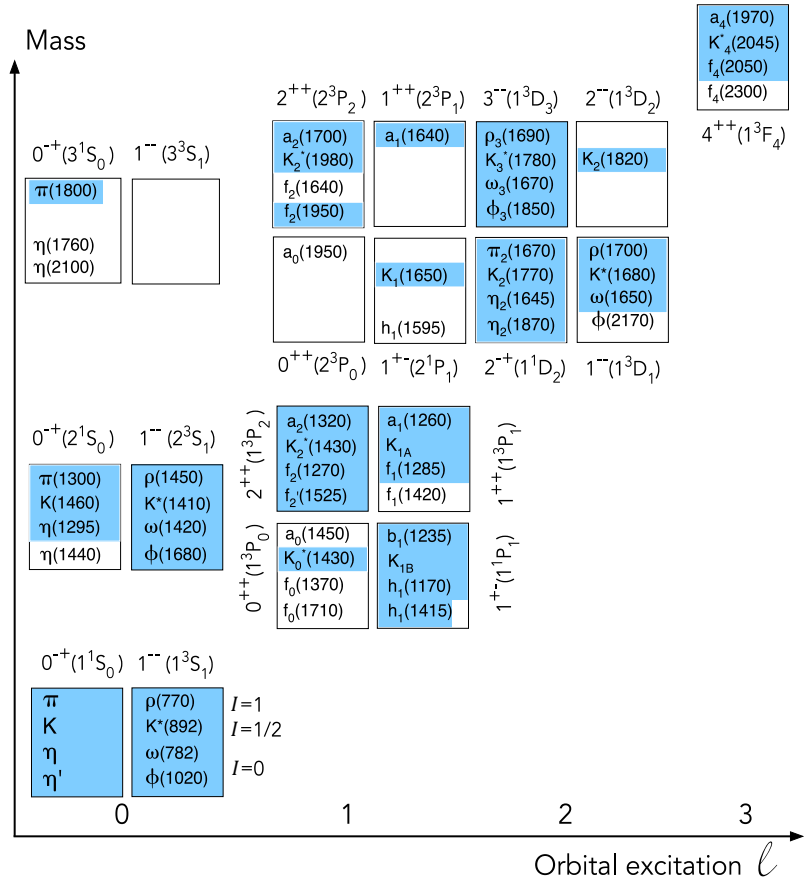

Figure 2.4: Spectrum of light meson nonets ordered by their $J^{PC}(n^{2s+1}l_J)$ quantum numbers. Inside the nonets the nine particles are ordered according to their isospin I (three $I = 1$ states, two times two $I = 1/2$ states). Mesons highlighted in blue are established, while the others are controversial entries. Edited version of Figure 63.1 in Ref. [31, Reviews Chapter 63].

An attempt to order the currently experimentally seen and established light mesons up to $\sim$ 2 GeV, listed by the Particle Data Group (PDG) [31, Summary Tables], into one coherent spectrum of nonets can be seen in Fig. 2.4. In this spectrum the meson nonets are not only ordered according to their J^{PC} quantum numbers, but also depending on their radial excitation n, orbital excitation l and spin coupling s quantum numbers. Similar to atomic physics the letters S, P, D, F,... are used for the description of the angular excitation $l = 0, 1, 2, 3, ...$, leading to the full classification of the nonets by their $J^{PC}(n^{2s+1}l_J)$ quantum numbers [31, Reviews Chapter 64].
Not all known light mesons, which are listed by the PDG, are shown in the spectrum. Some of them have controversial properties, which makes their categorization into the spectrum difficult, like the isoscalar scalar ($I^G(J^{PC}) = 0^+(0^{++})$) $f_0(500)$, $f_0(980)$ and $f_0(1500)$ mesons. For the listed f_0 mesons it is not clear if they are conventional mesons or are so-called exotic states [31, Reviews Chapter 63 and 64]. See Section 2.4 for more information on exotic states. The numbers in the brackets behind the particle names corresponds to their approximate mass in MeV.
A general property of isoscalar ($I = 0$) mesons with equal J^{PC} quantum numbers is, that they mix with each other. While this would also include heavier states with c and b quark content, as well as excited states, the mixing between states of different nonets is assumed to be negligible. The quark flavor wave functions for generic isoscalar states f and f' with the meson mixing angle θ can be written as [31, Reviews Chapter 15]:

$$f = \psi_8 \sin\theta + \psi_1 \cos\theta, \tag{2.3}$$

$$f' = \psi_8 \cos\theta - \psi_1 \sin\theta, \tag{2.4}$$

with the flavor singlet wave function ψ_1 and the flavor octet wave function ψ_8 being defined as:

$$\psi_1 = \frac{1}{\sqrt{3}}(u\bar{u} + d\bar{d} + s\bar{s}), \tag{2.5}$$

$$\psi_8 = \frac{1}{\sqrt{6}}(u\bar{u} + d\bar{d} - 2s\bar{s}). \tag{2.6}$$

For an "ideal" mixing angle of $\theta = 35.3°$, f' would be a pure $s\bar{s}$ state and f would be a pure $u\bar{u} + d\bar{d}$ state. This is almost the case for the mesons $f = \omega(782)$ and $f' = \phi(1020)$ with a mixing angle of about 36.5°, implying that $\phi(1020)$ is almost a pure $s\bar{s}$ state [31, Reviews Chapter 15].
This concludes the discussion of light mesons. Another important kind of mesons, for particle physics, as well as for this work, are states consisting of a charm and an anti-charm quark. These charmonium(-like) states will be presented in the next section.

2.3.2 Charmonium(-like) States

In 1974 two research groups found a new particle with a mass of about 3097 MeV, which would later be called J/ψ [15, 16]. The inner structure of the J/ψ meson is similar to that of a positronium, but instead of an electron and positron it contains a charm and anti-charm quark. Due to this similarity pure $c\bar{c}$ mesons are called charmonium states. After this discovery further states containing $c\bar{c}$ quarks were found, including the $\psi(2S)$ meson, which results from the excitation of the main quantum number of the J/ψ state. The $\psi(2S)$ state is the starting point for the analysis performed in this work. Like the vector meson J/ψ, the $\psi(2S)$ meson has J^{PC} quantum numbers of 1^{--} but has a higher mass of (3686.10 ± 0.06) MeV, and a width of (294 ± 8) keV, according to the PDG [31, Summary Tables]. A spectrum of the currently known states with $c\bar{c}$ content can be seen in Fig. 2.5 [29, 31].

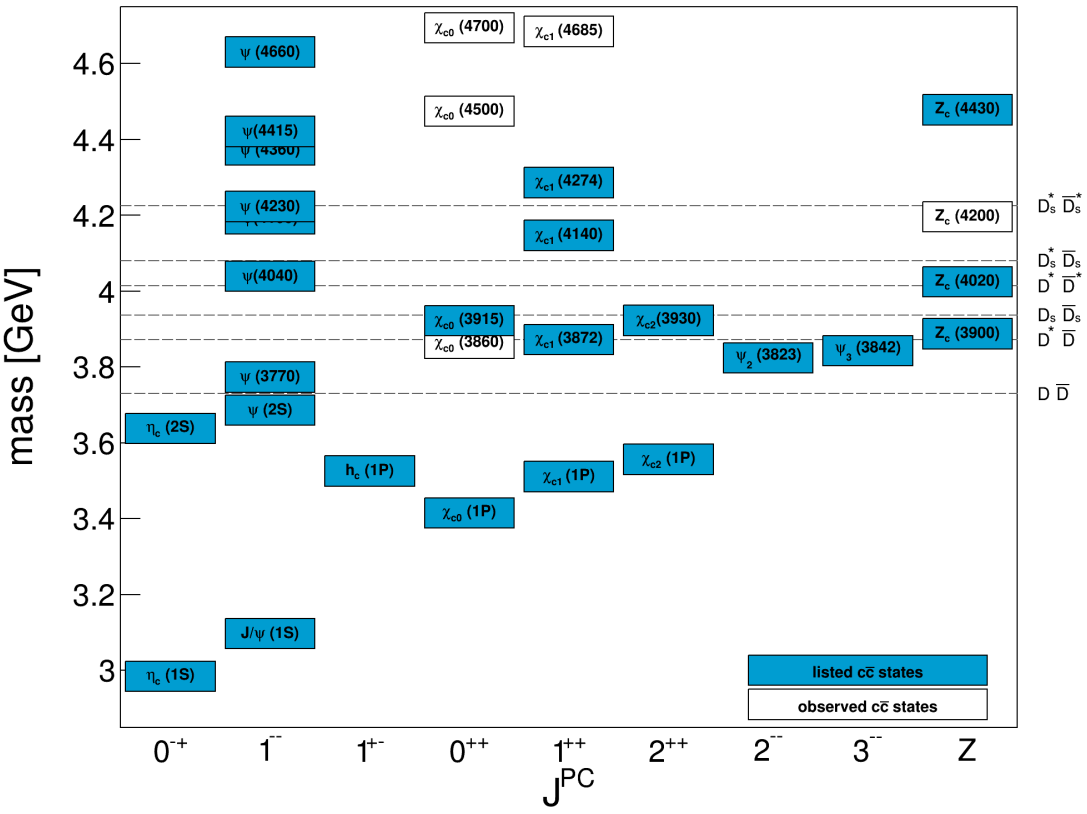

Figure 2.5: Mass spectrum of states containing $c\bar{c}$ content, including states which may be non-$q\bar{q}$ states like the $\chi_{c1}(3872)$, sorted by their J^{PC} quantum number, with an extra column for the Z_c states. States with blue boxes are established according to the particle data group (PDG) [31, Summary Tables], while the states with white boxes are controversial, but have assigned quantum numbers. The gray dotted lines indicate the energy thresholds, above which different $D\bar{D}$ meson combinations can be produced. A D meson always contains a charm quark, while $\bar{D}$ contains an anti-charm quark, making $D\bar{D}$ pairs dominant decay channels for $c\bar{c}$ states above the threshold.

It has to be noted that not all $c\bar{c}$ states shown are conventional charmonia, but also charmonium-like states are included, which contain $c\bar{c}$ content but are expected to be exotic states. The Z_c states would be examples of such exotic states. They decay into charmonia, but carry isospin, strongly indicating a non-conventional hadronic substructure [31, Reviews Chapter 15]. A more detailed description of the exotic states will be presented in the next section.

2.4 Exotic States

In general, all states which cannot be identified as conventional mesons, or baryons, are called exotics. Color neutrality is the only constraint for strongly bound states, thus infinitely many combinations of quarks and gluons would theoretically be possible. Some examples would be states made of more than three quarks, like tetraquarks, which are made of four quarks, or molecules, which are bound meson, or baryon states. Other possibilities would include states where gluons actively contribute to the charge-like quantum numbers (hybrids), and states entirely made out of gluons (glueballs) [31, Reviews Chapter 15]. A simple visualization of such states can be seen in Fig. 2.6. There already are candidates for all mentioned exotics. Certain candidates for tetraquarks, molecules and glueballs in the light meson sector are of special interest for this work, and thus will now be discussed in more detail.
It is strongly suggested that the nine scalar states $f_0(500)$, $K_0^*(700)$, $f_0(980)$ and $a_0(980)$ are exotic states. There are two promising theories on the exotic content of these states [31, Reviews Chapter 64].

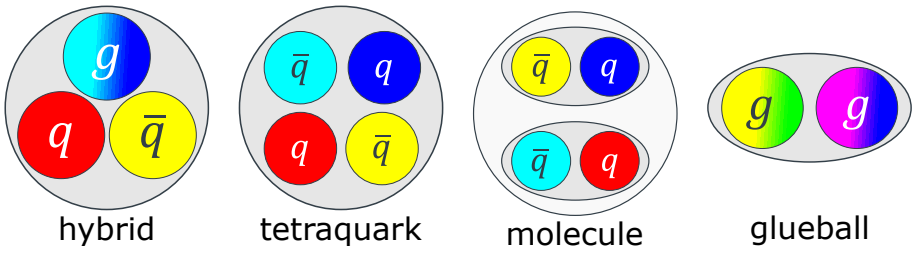

Figure 2.6: Depiction of four examples of exotic states, made of gluons and quarks and bound by the strong interaction.

The first one suggests that these nine states correspond to the lightest tetraquark nonet. To get the lightest tetraquark multiplet one must combine two triplets of light quarks with two triplets of light anti-quarks:

$$3 \otimes 3 \otimes \bar{3} \otimes \bar{3} = 9 \oplus 36 \oplus 18 \oplus \overline{18}.$$

After some reduction steps, one can split all tetraquark states into a nonet, a multiplet with 36 tetraquarks, and one with 18 tetraquarks, as well as a multiplet with 18 anti-tetraquarks. From symmetry considerations and spin and color conservation follows that the tetraquark

ground states are a nonet of scalar mesons with masses around 900 MeV [22]. This theoretical description would conveniently fit the aforementioned mesons leading to the following assignment of their quark content [31, Reviews Chapter 15]:

$$f_0(500) = \bar{u}\bar{d}ud,$$
$$f_0(980) = \frac{1}{\sqrt{2}}(u\bar{u} + d\bar{d})s\bar{s},$$
$$a_0^0(980) = \frac{1}{\sqrt{2}}(u\bar{u} - d\bar{d})s\bar{s},$$

$$a_0^+(980) = \bar{d}\bar{s}us, \qquad a_0^-(980) = \bar{u}\bar{s}ds,$$
$$K_0^{*+}(700) = \bar{s}\bar{d}ud, \qquad K_0^{*-}(700) = \bar{u}\bar{d}ds,$$
$$K_0^{*0}(700) = \bar{s}\bar{u}ud, \qquad \bar{K}_0^{*0}(700) = \bar{u}\bar{d}us.$$

The other proposal for the description of these states would be that they are molecules made of pions and kaons. Looking at their masses one would expect that the $f_0(500)$ is a $\pi\pi$ bound state, the $K_0^*(700)$ are $K\pi$ molecules and the $f_0(980)$ and $a_0(980)$ are $K\bar{K}$ states [31, Reviews Chapter 63].

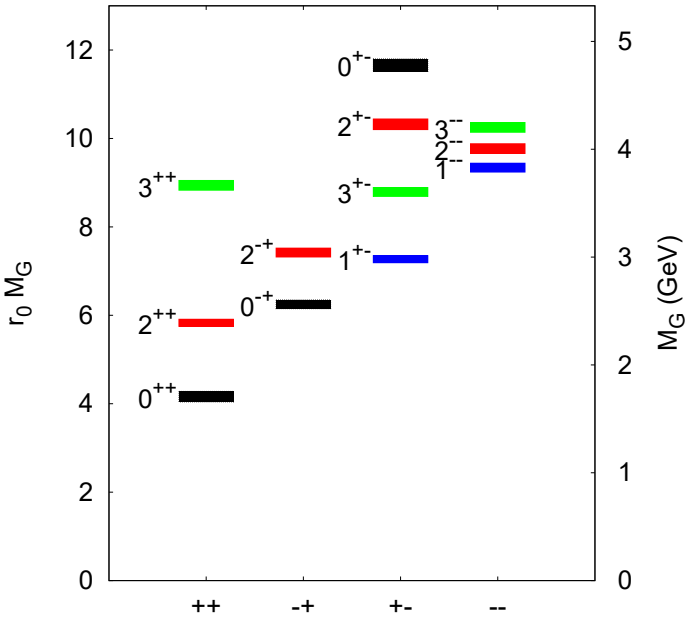

Figure 2.7: Glueball spectrum predicted by lattice QCD calculations using the quenched approximation. On the abscissa are the signs of the parity and charge conjugation eigenvalues. The mass of the glueball states in terms of the hadronic scale factor r_0 (left), and in GeV (right), are given on the ordinates. Figure taken from Ref. [24].

In Fig. 2.7 the mass and J^{PC} quantum number predictions for possible glueballs can be seen. The masses were determined by lattice QCD calculations using the so-called quenched approximation, neglecting $q\bar{q}$ loops [24]. According to multiple theories the glueball ground

state has the J^{PC} quantum numbers 0^{++} and lies in a mass range between 1600 MeV and 1700 MeV, while the first excited glueball state with $J^{PC} = 2^{++}$ is expected to be at a mass around 2300 MeV [24, 33–35].
When looking at the isoscalar mesons in the $0^{++}(1^3P_0)$ scalar nonet depicted in Fig. 2.8, it can be seen that one of the f_0 states appears to be supernumerary. With their $I^G(J^{PC}) = 0^+(0^{++})$ quantum numbers and masses between 1.3 GeV and 1.8 GeV these f_0 states are perfect candidates for carrying at least admixtures of the lightest glueball. There also already exist theories proposing mixing strength between the f_0 resonances and the glueball, like in Refs. [36, 37] which have to be tested using experimental data.

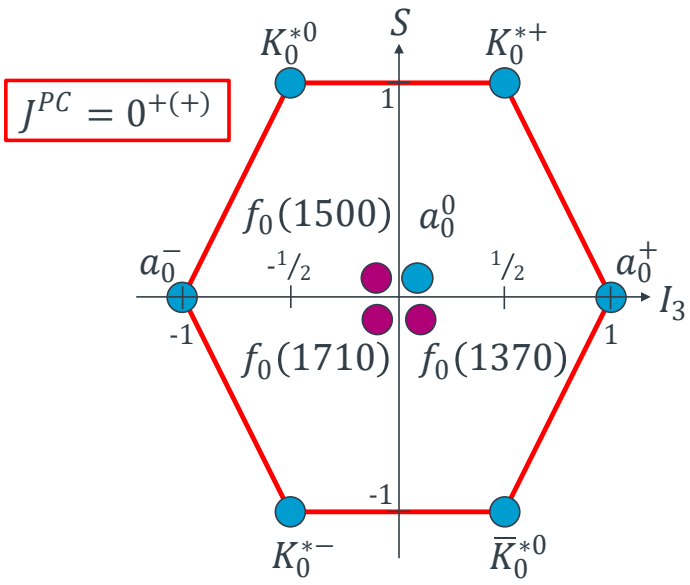

Figure 2.8: The scalar meson nonet ($0^{++}(1^3P_0)$) with a supernumerary isoscalar f_0 state according to [31, Reviews Chapter 63, summery tables].

Now that multiple theories have been laid out for the contents of the f_0 resonances it is the experimentalist's task to extract the real nature of these states. Due to their large widths and position near production thresholds of their possible decay channels ($\pi\pi$, 4π, $K\bar{K}$, $\eta\eta$, and $\eta\eta'$), the analysis of these states has proven to be rather challenging. Models respecting unitarity and analyticity are needed to describe the invariant mass spectra of the possible f_0 decay channels. An approach that satisfies all criteria, and is thus used in this work, will be introduced in the next chapter.

3. Quantum Mechanical Scattering Theory

One of the most successful ways to gain information about the substructure of quantum mechanical particles and the forces that dictate their interactions are collision experiments. To extract this information from the results of such experiments, a comprehensive quantum mechanical scattering theory is needed that connects the measurable observables with the parameters of more fundamental theoretical models, like the standard model. On the most basic level, the scattering theory, which will be presented in the next sections, describes the interaction of particles. This includes the easiest case of elastic scattering, but also more complicated scattering, like resonant production and decay processes.
To introduce the fundamental aspects of scattering theory, the first section of this chapter will give a detailed description of the non-relativistic elastic scattering problem. After this introduction, the second section will provide an overview of the various aspects that are needed to formulate a relativistic scattering model for the data analyzed in this work. Also, methods will be introduced to extract physical parameters from the scattering model.

3.1 Non-Relativistic Scattering

Before being able to discuss more complex scattering models, which can describe the data analyzed in this work, the fundamental framework of scattering theory must be introduced. To simplify the following discussion, the quantum mechanical scattering problem is reduced to its simplest case, being non-relativistic elastic scattering of two non-identical particles without substructure. To fully characterize this scattering process, the solution of the Schrödinger equation has to be determined. Three different approaches will be shown to solve the Schrödinger equation. The first two approaches start with the stationary Schrödinger equation, and then use differential equations, in the first case, and integral equations, in the second one, to find its solutions. In the third approach the time dependent Schrödinger equation is chosen as a starting point, and time propagation operators are used to find solutions to the equation.

It will be shown that all three approaches give equivalent results, but each of them provides a new way of solving the scattering problem. These results from each approach will then be combined to define a model that can describe experimental data with the results from scattering theory.

3.1.1 Differential Equations

The starting point for the first approach is the spatial representation of the stationary Schrödinger equation, which describes the two-particle scattering problem [25]:

$$\left(-\frac{\Delta_1}{2m_1} - \frac{\Delta_2}{2m_2} + w(\vec{r}_1, \vec{r}_2)\right) \phi(\vec{r}_1, \vec{r}_2) = \epsilon\ \phi(\vec{r}_1, \vec{r}_2), \tag{3.1}$$

with Δ being the Laplace operator and ϕ being the wave function describing the scattering process. This equation also contains the masses of the two scattering particles m_1 and m_2, their position vectors $\vec{r}_1$ and $\vec{r}_2$, as well as the potential of the interaction w and the energy of the process ϵ. If the interaction potential is spatially confined, and energy is conserved, ϵ can be written as the sum of kinetic energies $E_{\text{kin},1}$ and $E_{\text{kin},2}$ of the two particles, before and after the interaction takes place:

$$\epsilon = (E_{\text{kin},1} + E_{\text{kin},2})_{\text{before}} = \frac{|\vec{p}_1|^2}{2m_1} + \frac{|\vec{p}_2|^2}{2m_2} = (E_{\text{kin},1} + E_{\text{kin},2})_{\text{after}}, \tag{3.2}$$

with $\vec{p}_1$ and $\vec{p}_2$ being the momenta of the two scattering particles. Equation (3.1) can be split into one equation describing the dynamics of the center of mass system, which is of no further interest for the following discussion, and one describing the relative dynamics between both particles [25]:

$$\left(-\frac{\Delta_r}{2\mu} + w(\vec{r})\right) \phi_{\text{rel}}(\vec{r}) = \epsilon_{\text{rel}}\ \phi_{\text{rel}}(\vec{r}), \tag{3.3}$$

with the reduced mass $\mu = m_1 m_2/(m_1 + m_2)$, and the energy ϵ_{rel} being defined as:

$$\epsilon_{\text{rel}} = \frac{1}{2(m_1 + m_2)} \left(\frac{m_2}{m_1} p_1^2 - 2\vec{p}_1 \cdot \vec{p}_2 + \frac{m_1}{m_2} p_2^2\right). \tag{3.4}$$

Equation (3.3) effectively describes the scattering of one particle with the mass μ on an external potential $w(\vec{r})$. To formalize this observation, Eq. (3.3) can be redefined as the stationary Schrödinger equation of the wave function $\psi(\vec{r})$:

$$\left(-\frac{\Delta}{2m} + v(\vec{r})\right) \psi(\vec{r}) = E\ \psi(\vec{r}), \tag{3.5}$$

with the potential $v(\vec{r})$, energy E, and the mass m.
The next step will be to solve Eq. (3.5), using the boundary conditions that the wave function must be analytical for $r \to 0$, and can be written as a superposition of an incoming wave ψ_i, and a scattered wave ψ_s for $r \to \infty$. The wave function for $r \to \infty$, which will be referred to as the asymptotic wave function from this point on, is defined as follows:

$$\psi(\vec{r}) \xrightarrow{r\to\infty} \psi_{\text{asymp}}(\vec{r}) = \psi_{\text{i}}(\vec{r}) + \psi_{\text{s}}(\vec{r}). \tag{3.6}$$

In the case of a particle with no inner structure the incoming wave ψ_i can be defined as a plane wave. If this is the case, the scattered wave function ψ_s can be defined using Huygens principle [38], which says that a plain wave scattering on a point-like potential results in a spherical wave. For the incorporation of spatially distributed potentials, the so-called scattering amplitude $f(\theta, \varphi)$ has to be introduced, which, in combination with the results of Huygens principle, results in the following scattered wave function:

$$\psi_s(\vec{r}) = f(\theta, \varphi)\frac{e^{ikr}}{r}, \tag{3.7}$$

with the wave number $k = \sqrt{2mE}$. A spatially distributed potential can be interpreted as infinitely many point-like potentials with varying strengths. The scattering amplitude, which only depends on the scattering angles θ and φ, contains the information about all possible scattering processes, and includes their interference effects into the scattered wave function. Together with the plane wave one gets the following asymptotic wave function:

$$\psi_{\text{asymp}}(\vec{r}) = e^{ikz} + f(\theta, \varphi)\frac{e^{ikr}}{r}. \tag{3.8}$$

Now the goal is to connect the scattering amplitude with the cross section. In general, the differential cross section can be written in terms of the incoming particle current density j_i and scattered particle current density j_s [25]:

$$\left(\frac{d\sigma}{d\Omega}\right) = \frac{r^2 j_s}{j_i}. \tag{3.9}$$

Then the classical particle current densities can be replaced by quantum mechanical probability current densities, which are defined as follows:

$$\vec{j} = \frac{i}{2m}\left(\psi\vec{\nabla}\psi^* - \psi^*\vec{\nabla}\psi\right). \tag{3.10}$$

By inserting the wave function for the plane wave in j_i and Eq. (3.7) in j_s, one gets the following relation for the differential cross section:

$$\left(\frac{d\sigma}{d\Omega}\right) = |f(\theta, \varphi)|^2, \tag{3.11}$$

The total cross section can then be calculated by integrating the differential cross section over all angles θ and φ:

$$\sigma = \iint |f(\theta, \varphi)|^2 \, \mathrm{d}\theta \, \mathrm{d}\varphi. \tag{3.12}$$

In the next step probability conservation will be introduced into the definition of the cross section by requiring that every current that enters a reasonably large sphere must eventually leave it again. This condition can be written as:

$$\iint_{\text{large sphere}} \vec{j} \cdot d\vec{f} = 0. \tag{3.13}$$

By inserting Eq. (3.10) into this integral equation, and using the asymptotic wave function (cf. Eq. (3.8)) to calculate the probability current density, one gets the so-called optical theorem:

$$\sigma = \frac{4\pi}{k}\mathrm{Im}f(0,\varphi). \tag{3.14}$$

This theorem incorporates probability conservation by requiring that all waves that scatter, thus having a scattering angle $\theta \neq 0$, are excluded from the outgoing wave that did not scatter, having an angle of $\theta = 0$. Mathematically this is facilitated by interference effects resulting from the imaginary part of the scattering amplitude.
Until this point, with Eqs. (3.11) and (3.12) a way was found to connect the experimentally accessible cross section to the theoretical scattering amplitude, and thus the asymptotic wave function. Furthermore, with Eqs. (3.2) and (3.14) conditions were derived for the incorporation of energy and probability conservation into the approach. The next challenge is now to find a parameterization for the scattering amplitude, which can be used to solve the integral and gain a direct relation to the total cross section. In the next section one such approach will be presented for a simplified potential.

Partial Wave Decomposition

In this section, a method will be introduced, that can be used to decompose the scattering process into partial waves. In the following paragraphs, this decomposition will be used to solve the scattering problem for a radially symmetrical potential $v(\vec{r}) = v(r)$, to establish the method. Later in Sections 3.1.3 and 3.2.5 a similar method will be used for different descriptions of the scattering process.
In case of a radially symmetrical potential, the dependency of the wave function on the azimuth angle φ can be eliminated by demanding that the incoming wave propagates in z-direction. It is thus possible to expand the wave function as follows [25]:

$$\psi(k,\vec{r}) = \sum_{l=0}^{\infty} \frac{R(k,r)}{kr} \cdot P_l(\cos\theta), \tag{3.15}$$

with $R(k,r)$ being the radial wave function and $P_l(\cos\theta)$ being Legendre polynomials. When inserting this wave function into Eq. (3.5) one gets the following differential equation for the radial wave function:

$$\frac{d^2R_l(k,r)}{dr^2} + \left(k^2 - \frac{l(l+1)}{r^2} - 2m\cdot v(r)\right)R_l(k,r) = 0. \tag{3.16}$$

The problem can now be split into three concentric spherical regions around the scattering center at $r = 0$, still assuming that the potential $v(r)$ is spatially confined.

1. The scattering region with $v(r) \neq 0$, including the analyticity boundary condition for $r \to 0$.

2. The intermediate region with $v(r) = 0$, but the asymptotic boundary condition does not apply.

3. The asymptotic region with $v(r) = 0$ and $r \to \infty$, where the asymptotic boundary condition applies, which means Eq. (3.8) can be used.

To solve the Schrödinger equation in the first region, the potential has to be known, which is not the case for this general discussion, thus this step will be skipped. For $v(r) = 0$, Eq. (3.16) can be solved in the intermediate region using the Bessel-Riccati functions [39]. The exact solution is of no further interest, but for $r \to \infty$ the wave function in the intermediate region can be written as:

$$\psi_{\text{inter}}(\vec{r}) \xrightarrow{r\to\infty} \sum_{l=0}^{\infty} \frac{(2l+1)i^l e^{i\delta_l}}{k} \sin\left(kr - l\frac{\pi}{2} + \delta_l\right) \frac{P_l(\cos\theta)}{r}, \tag{3.17}$$

with δ_l being the so-called scattering phases, which at this point are just constants resulting from solving Eq. (3.16).
Now, the asymptotic wave function (cf. Eq. (3.8)) will be brought to the form of Eq. (3.15). This is achieved by expanding the plain wave function using the asymptotic representation of the Bessel functions:

$$e^{ikz} \xrightarrow{r\to\infty} \sum_{l=0}^{\infty} \frac{(2l+1)i^l}{k} \sin\left(kr - l\frac{\pi}{2}\right) \frac{P_l(\cos\theta)}{r}. \tag{3.18}$$

By comparing this equation with Eq. (3.17), it can be seen that both are representations of a plain wave but have a phase shift δ_l between them, giving δ_l the name scattering phase. To get the full partial wave decomposition of the asymptotic wave function, the scattering amplitude must be expanded in respect to partial scattering amplitudes f_l [39]:

$$f(\theta) = \sum_{l=0}^{\infty} f_l \cdot P_l(\cos\theta). \tag{3.19}$$

Now, both Eqs. (3.18) and (3.19) can be inserted into Eq. (3.8) to get the following representation of the asymptotic wave function:

$$\psi_{\text{asymp}} = \sum_{l=0}^{\infty} \left(\frac{(2l+1)i^l}{k} \sin\left(kr - l\frac{\pi}{2}\right) + f_l \cdot e^{ikr} \right) \frac{P_l(\cos\theta)}{r}. \tag{3.20}$$

By demanding an analytical transition from Eq. (3.17) to Eq. (3.20), one gets the following relation between the partial scattering amplitude and the scattering phase [25]:

$$f_l = \frac{2l+1}{2ik} \left(e^{2i\delta_l} - 1\right). \tag{3.21}$$

To get the connection between the cross section and the partial scattering amplitude, Eq. (3.19) has to be inserted into Eq. (3.12). Then, the relation between the cross section and the scattering phase can be derived by substituting f_l using Eq. (3.21):

$$\sigma = 4\pi \sum_{l=0}^{\infty} \frac{|f_l|^2}{2l+1} = \frac{4\pi}{k^2} \sum_{l=0}^{\infty} (2l+1) \sin^2 \delta_l, \tag{3.22}$$

This kind of partial wave decomposition allows for the inclusion of angular momentum conservation, by only allowing specific angular momentum quantum numbers in the sum. For

this simple example, using a radially symmetric potential, it is now possible to fully characterize the asymptotic wave function for a reaction, using the results of a cross section measurement.
This concludes the approach of using differential equation to solve the stationary Schrödinger equation of the scattering problem. In the next section, an approach using integral equations will be introduced to find a way to characterizing the scattering amplitude for an arbitrary potential.

3.1.2 Integral Equations

The second approach also starts with the stationary Schrödinger equation from Eq. (3.5), but this time written in bra-ket notation:

$$(E - \hat{H})\,|\psi\rangle = \hat{V}\,|\psi\rangle\,, \tag{3.23}$$

with the potential operator $\hat{V}$, which is related to the potential $v(\vec{r})$ over:

$$\langle\vec{r}|\hat{V}|\vec{r}'\rangle = \delta(\vec{r} - \vec{r}')v(\vec{r}). \tag{3.24}$$

For the scattering problem at hand, the Hamilton operator is defined as the kinematic energy operator in spatial representation:

$$\hat{H} = \frac{\Delta}{2m}. \tag{3.25}$$

The homogeneous solution ($\hat{V} = 0$) of Eq. (3.23) is a plain wave:

$$|\psi_{\text{hom}}\rangle = |\vec{k}\rangle\,, \tag{3.26}$$

which in spatial representation is defined as:

$$\langle\vec{r}|\vec{k}\rangle = \psi(\vec{r})_{\text{hom}} = \frac{1}{(2\pi)^{3/2}} e^{i\vec{k}\vec{r}}. \tag{3.27}$$

The solution of the inhomogeneous part can be expressed using the Green's operator $\hat{G}$ [25]:

$$|\psi_{\text{inhom}}\rangle = \hat{G}(E)\hat{V}\,|\psi\rangle\,. \tag{3.28}$$

Then, using Eqs. (3.26) and (3.28), the formal solution for Eq. (3.23) can be written as:

$$|\psi\rangle = |\psi_{\text{hom}}\rangle + |\psi_{\text{inhom}}\rangle = |\vec{k}\rangle + \hat{G}(E)\hat{V}\,|\psi\rangle\,. \tag{3.29}$$

This equation is called Lippmann-Schwinger equation and can be explicitly written as an integral equation in spatial representation for the state $|\psi\rangle$:

$$\langle\vec{r}|\psi\rangle = \langle\vec{r}|\vec{k}\rangle + \int d^3r' \int d^3r''\,\langle\vec{r}|\,\hat{G}(E)\,|\vec{r}'\rangle\,\langle\vec{r}'|\,\hat{V}\,|\vec{r}''\rangle\,\langle\vec{r}''|\psi\rangle \tag{3.30}$$

$$\Leftrightarrow \psi(\vec{r}) = \frac{e^{i\vec{k}\vec{r}}}{(2\pi)^{3/2}} + \int d^3r'\, G(\vec{r},\vec{r}';E)\cdot v(\vec{r}')\cdot\psi(\vec{r}') \tag{3.31}$$

Using the boundary conditions that were introduced in the last section the following representation of the Greens function can be derived for $r \to \infty$ [25]:

$$G(\vec{r},\vec{r}') \xrightarrow{r\to\infty} -\frac{m}{2\pi r} e^{ik_0 r} \cdot e^{-i\vec{k}\vec{r}'}, \tag{3.32}$$

with $\vec{k}_0$ being the wave vector of the incoming wave, and $\vec{k}$ being the wave vector of the scattered wave. This asymptotic definition of the Greens function can now be inserted into Eq. (3.31) resulting in the following definition for the asymptotic wave function in spatial representation:

$$\psi_{\text{asymp}}(\vec{r}) = \frac{1}{(2\pi)^{3/2}} \left\{ e^{i\vec{k}_0\vec{r}} + \left[-m\sqrt{2\pi} \int \mathrm{d}^3 r' e^{i\vec{k}\vec{r}'} \cdot v(\vec{r}') \cdot \psi(\vec{r}') \right] \frac{e^{ik_0 r}}{r} \right\} \tag{3.33}$$

$$= \frac{1}{(2\pi)^{3/2}} \left\{ e^{i\vec{k}_0\vec{r}} + \left[-m\sqrt{2\pi} \langle \vec{k}|\hat{V}|\psi\rangle \right] \frac{e^{ik_0 r}}{r} \right\}. \tag{3.34}$$

Then, by comparing with Eq. (3.8) the scattering amplitude can be identified as:

$$f(\theta,\varphi) = -m\sqrt{2\pi}\,\langle \vec{k}|\hat{V}|\psi\rangle\,. \tag{3.35}$$

Hence, the whole information of the scattering process is contained in the matrix element $\langle \vec{k}|\hat{V}|\psi\rangle$, which includes the still unknown wave function $\psi(\vec{r})$. To gain further insight into the scattering amplitude without knowing the scattering wave function, one can define the so-called transition operator $\hat{T}$, which has the following property [25]:

$$\hat{T}\,|\vec{k}_0\rangle = \hat{V}\,|\psi\rangle\,. \tag{3.36}$$

By using this definition, the information about the scattering process is transferred from the state $|\psi\rangle$, to the operator $\hat{T}$. Inserting this definition into Eq. (3.35) results in:

$$f(\theta,\varphi) = -m\sqrt{2\pi}\,\langle \vec{k}|\hat{T}|\vec{k}_0\rangle\,|_{k=k_0}. \tag{3.37}$$

The matrix element $T = \langle \vec{k}|\hat{T}|\vec{k}_0\rangle$ can be interpreted as the probability that an incoming plane wave $|\vec{k}_0\rangle$ transitions to an outgoing plane wave $|\vec{k}\rangle$. For elastic scattering processes, the energy is conserved, thus the condition $k = k_0$ must be fulfilled. T matrix elements which satisfy this condition are called on-shell T matrix elements. By multiplying Eq. (3.29) from the left with $\hat{V}$ and inserting $\hat{T}$ into Eq. (3.31) one gets the Lippmann-Schwinger equation for the $\hat{T}$ operator:

$$\hat{T}\,|\vec{k}_0\rangle = \hat{V}\,|\vec{k}_0\rangle + \hat{V}\hat{G}(E)\hat{T}\,|\vec{k}_0\rangle\,, \tag{3.38}$$

which can be written as the following operator equation:

$$\hat{T} = \hat{V} + \hat{V}\hat{G}\hat{T}. \tag{3.39}$$

The $\hat{T}$ operator connects the potential, which governs the scattering process, with the scattering amplitude, which is directly connected to the experimental cross section. Hence, solving Eq. (3.38) for a given potential operator $\hat{V}$, provides a direct way to parameterize the scattering amplitude over Eq. (3.37).

But more often than not, the Lippmann-Schwinger equation for the $\hat{T}$ operator cannot be solved exactly, and approximation methods have to be used. These approximated solutions do not necessarily fulfill the optical theorem (cf. Eq. (3.14)) and thus violate probability conservation. A way to resolve this problem will be presented in the next section.

3.1.3 Time Dependent Approach

Until now only the solutions of the time independent stationary Schrödinger equation were discussed. To gain further insight into the scattering problem, in the third approach, the time evolution of the particle states will be considered. The transition of an initial state $|\psi_\mathrm{i}(t_\mathrm{i})\rangle$ into a final state $|\psi_\mathrm{f}(t_\mathrm{f})\rangle$ can generally be described by time evolution operators $\hat{U}(t_f, t_i)$. A common approach to describe the time evolution of the scattering process is to assume that the initial and final states at $t_\mathrm{i} = -\infty$ and $t_\mathrm{f} = \infty$ are free, while the interaction takes place at around $t = 0$ [25, 40]. The operator describing the whole-time evolution of the scattering process is the unitary $\hat{S}$ operator, which is defined over the Møller operators $\hat{\Omega}_+$ and $\hat{\Omega}_-$ as [25]:

$$\hat{S} = \hat{\Omega}_-^\dagger \hat{\Omega}_+. \tag{3.40}$$

The Møller operators are connected to the time dependent potential via:

$$\Omega_\pm = \lim_{t \to \mp\infty} \mathcal{T}\left\{\exp\left[i \int_0^t \mathrm{d}t'\, \hat{V}(t')\right]\right\}, \tag{3.41}$$

with $\mathcal{T}$ implying a time ordered product, which ensures the time sequence of the process is not broken. To determine a more direct relation between the $\hat{S}$ operator and the $\hat{V}$ operator, again assuming that the scattering potential is spatially confined, perturbation theory can be used. To make such an approach possible, one uses the adiabatic theorem [41] by introducing the following small continuous perturbation in the potential $\hat{V}$:

$$\hat{V}(t) \to \hat{V}_\epsilon(t) = e^{-\epsilon \cdot |t|} \cdot \hat{V}(t), \tag{3.42}$$

using the small positive perturbation parameter ϵ. This new potential can now be inserted into the definition of the Møller operators, and the exponential function can be expanded according to its power series, which yields:

$$\Omega_\pm = \lim_{t \to \mp\infty} \lim_{\epsilon \to 0} \sum_{n=0}^{\infty} (-i)^n \int_0^t \mathrm{d}t_1\, \hat{V}_\epsilon(t_1) \int_0^{t_1} \mathrm{d}t_2\, \hat{V}_\epsilon(t_2) \ldots \int_0^{t_{n-1}} \mathrm{d}_n\, \hat{V}_\epsilon(t_n). \tag{3.43}$$

Inserting this definition into Eq. (3.40) results in the following equation:

$$\hat{S} = \lim_{\epsilon \to 0} \sum_{n=0}^{\infty} (-i)^n \int_{-\infty}^{\infty} dt_1 \hat{V}_\epsilon(t_1) \int_{-\infty}^{t_1} dt_2 \hat{V}_\epsilon(t_2) \cdots \int_{-\infty}^{t_{n-1}} dt_n \hat{V}_\epsilon(t_n). \tag{3.44}$$

The calculation of the matrix element $\langle \vec{k}' | \hat{S} | \hat{k} \rangle$ can then be split into orders of ϵ. Solving up to the first order results in:

$$\langle \vec{k}' | \hat{S} | \vec{k} \rangle = \delta(\vec{k} - \vec{k}') - 2\pi i \delta(E(k) - E(k')) \langle \vec{k}' | \hat{V} | \vec{k} \rangle . \tag{3.45}$$

Starting from this equation it can be shown that the S matrix element are connected to the T matrix elements via:

$$\langle \vec{k}' | \hat{S} | \vec{k} \rangle = \delta(\vec{k} - \vec{k}') - 2\pi i \delta(E(k) - E(k')) \langle \vec{k}' | \hat{T} | \vec{k} \rangle . \tag{3.46}$$

A detailed derivation for this relation can be found in [25, Section 3.6.5]. This equation shows the new features which were introduced by this approach. The S matrix element not only describes the interacting part of the process, which is included in the T matrix element, but also incorporates the cases in which no interaction takes place, which is facilitated by the first part of the sum. Energy and momentum conservation are intrinsically ensured by the δ-functions, only allowing for on-shell T matrix elements. That the T matrix elements, which resulted from solving the time-independent Schrödinger equation, are directly connected to the results of the time-dependent formulation, show the equivalence of the two approaches. Eq. (3.46) can also be written as an operator equation:

$$\hat{S} = \hat{1} - 2\pi i \delta(E_{\text{in}} - \hat{H})\hat{T}, \tag{3.47}$$

with $\hat{H}$ being the kinetic energy operator, which was defined in Eq. (3.25). By defining the T matrix elements using Eq. (3.46), which includes the unitary $\hat{S}$ operator, it can be ensured, that the T matrix elements fulfill the optical theorem, and thus conserve probability. However, this approach requires that the S matrix elements are known, which is a problem in itself. Nevertheless, there exists a very successful approach to derive the T matrix elements, using the unitarity of the $\hat{S}$ operator, which will be introduced in the next section.

The K Operator

As addressed at the end of Section 3.1.2, often only approximate solutions for the Lippmann-Schwinger equation of the $\hat{T}$ operator can be derived, which not necessarily fulfill the optical theorem. In this section, a new operator will be introduced, which uses the unitarity of the $\hat{S}$ operator and its connection to the $\hat{T}$ operator to formulate a new approach for solving the scattering problem. This new operator is called the $\hat{K}$ operator, and is defined over the $\hat{S}$ operator as follows [25]:

$$\hat{S} = \left(\hat{1} - i\pi\delta(E - \hat{H})\hat{K}\right) \frac{1}{\hat{1} + i\pi\delta(E - \hat{H})\hat{K}}. \tag{3.48}$$

From the unitarity of the $\hat{S}$ operator it can be derived that the $\hat{K}$ operator has to be hermitian, and thus has to fulfill the following relation:

$$\hat{K}^\dagger = \hat{K}. \tag{3.49}$$

By inserting Eq. (3.48) into Eq. (3.47) one gets a relation that connects the $\hat{T}$ and the $\hat{K}$ operators:

$$\hat{T} = \hat{K} - i\pi\hat{T}\delta(E - \hat{H})\hat{K}. \tag{3.50}$$

This equation is called Heitler's damping equation. In the next step, Eq. (3.50) can be inserted into the Lippmann-Schwinger equation for the $\hat{T}$ operator, defined in Eq. (3.38), to get the following integral equation:

$$\hat{K} = \hat{V} + \hat{V}\left(\frac{1}{E - \hat{H} + i\epsilon} + i\pi\delta(E - \hat{H})\right)\hat{K} \tag{3.51}$$

$$\hat{K} = \hat{V} + \hat{V}\hat{G}_s\hat{K}. \tag{3.52}$$

The argument in brackets can be identified as the Green's function for the boundary condition of standing waves $\hat{G}_s$. Now, the only difference between Eq. (3.52) and Eq. (3.39) is the Green's function, which for the $\hat{K}$ operator equation has a real matrix representation $\langle\vec{r}|\hat{G}_s|\hat{r}'\rangle$, resulting in hermitian $\hat{K}$ operators for every (approximate) solution of Eq. (3.52). After a solution for Eq. (3.52) is found, Eq. (3.50) can be used to determine the on-shell T matrix elements, which intrinsically fulfill the optical theorem. Thus, an approach was found that allows for an energy and probability conserving definition of the T matrix elements, which can then be used to parameterize the experimentally approachable cross section.
As the last step of the discussion of non-relativistic scattering theory, the partial wave decomposition of the T and K matrix elements will be presented.

Partial Wave Decomposition

In this section the partial wave decomposition of the T and K matrix elements will be presented and used to derive relations between the two matrix elements, as well as between partial T matrix elements and the cross section. Like in Section 3.1.1, a spherical symmetric potential $v(\vec{r}) = v(r)$ is assumed for the following discussions. Using the partial wave decomposition of the on-shell T matrix element [39]:

$$\langle\vec{k}'|\hat{T}|\vec{k}\rangle = \sum_l \frac{2l+1}{4\pi} T_l(k) P_l(\cos\theta), \tag{3.53}$$

as well as the partial wave decomposition of the scattering amplitude in Eq. (3.19), and insert them in Eq. (3.37), one gets the following equation:

$$f_l = -\frac{2l+1}{\sqrt{8\pi}} m T_l. \tag{3.54}$$

This definition of the partial scattering amplitude can now be inserted into Eq. (3.22) to gain the direct relation between the cross section and the partial T matrix element:

$$\sigma = \frac{m^2}{2\pi} \sum_l (2l+1)|T_l|^2. \tag{3.55}$$

The partial T matrix elements shall now be expressed in terms of the partial K matrix elements which are defined as follows [39]:

$$\langle\vec{k}'|\hat{K}|\vec{k}\rangle = \sum_l \frac{2l+1}{4\pi} K_l(k', k) P_l(\cos\theta). \tag{3.56}$$

As the first step, Heitler's damping equation (cf. Eq. (3.50)) must be written as an integral equation in its on-shell momentum representation:

$$\langle\vec{k}'|\hat{T}|\vec{k}\rangle = \langle\vec{k}'|\hat{K}|\vec{k}\rangle - i\pi mk \int \mathrm{d}k'' \, \langle\vec{k}'|\hat{K}|\vec{k}''\rangle \langle\vec{k}''|\hat{T}|\vec{k}\rangle . \tag{3.57}$$

By inserting the on-shell partial wave decomposition of the T and K matrix element into this equation one gets:

$$T_l(k) = K_l(k) - i\pi mk K_l(k) T_l(k). \tag{3.58}$$

This equation is not an integral equation, but an algebraic one, which means that one can simply solve for T_l resulting in the following equation:

$$T_l(k) = [1 + i\pi m k K_l(k)]^{-1} K_l(k). \tag{3.59}$$

The last step is now to find a definition for the partial K matrix element. As a starting point one uses the momentum representation of the integral equation resulting from Eq. (3.52) [25]:

$$\langle \vec{k}' | \hat{K} | \vec{k} \rangle = \langle \vec{k}' | \hat{V} | \vec{k} \rangle - 2m \cdot \mathcal{P} \int \mathrm{d}k''\, k''^2 \langle \vec{k}' | \hat{V} | \vec{k}'' \rangle \left(\frac{1}{k^2 - k''^2} \right) \langle \vec{k}'' | \hat{K} | \vec{k} \rangle, \tag{3.60}$$

with $\mathcal{P}$ indicating that Cauchy's principal value is used for this improper integral. Now the last thing missing for the definition of an integral equation for the partial K matrix elements is the partial wave decomposition of the potential matrix elements, which is defined as follows [39]:

$$\langle \vec{k}' | \hat{V} | \vec{k} \rangle = \sum_l \frac{2l+1}{4\pi} v_l(k', k) P_l(\cos\theta). \tag{3.61}$$

The partial waves of the potential are defined in the following way [25]:

$$v_l(k', k) = \frac{2}{\pi} \int \mathrm{d}r\, r^2 j_l(k'r) v(r) j_l(kr), \tag{3.62}$$

with j_l being the spherical Bessel functions. By inserting Eqs. (3.56) and (3.61) into Eq. (3.60) the definition for the on-shell partial K matrix element can be derived:

$$K_l(k) = v_l(k) + 2m \cdot \mathcal{P} \int \mathrm{d}k''\, k''^2 v_l(k, k'') \left(\frac{1}{k^2 - k''^2} \right) K_l(k'', k). \tag{3.63}$$

Equation (3.63) can now be solved for a given potential, which was e.g., derived from theoretical considerations of the particle's interaction, yielding the partial K matrix element. This element can then be inserted into Eq. (3.59) to directly get the partial T matrix elements, which are connected to the cross section over Eq. (3.55). Using this approach incorporates energy and probability conservation, while the decomposition into partial waves, dependent on the angular momentum quantum number l, allows for the inclusion of angular momentum conservation. This concludes the non-relativistic approach to the scattering problem. In the next section, the established framework will be extended to fit the requirements for the analysis performed in this work.

3.2 Relativistic Scattering

In this section, Lorentz invariance, multiple scattering channels and spin will be introduced into the description of the non-relativistic scattering theory introduced in Section 3.1. Furthermore, different parameterizations for the scattering problem, as well as methods to extract the physical parameters of interest from such parameterizations will be presented.
As the first step, the Lorentz invariant representation of the two-particle scattering problem will be established. The following discussion considers two asymptotic states $|p_1, p_2\rangle$ and $|p_1', p_2'\rangle$ each state consisting of two non-interacting particles with four-momenta p_1 and p_2, and p_1' and p_2' respectively. The transition between the two states is facilitated by the $\hat{S}$ operator leading to the following S matrix element:

$$\langle p_1', p_2'|\hat{S}|p_1, p_2\rangle = S(p_1, p_2; p_1', p_2'). \tag{3.64}$$

For the following discussions only the interacting part of the S matrix elements is of interest. It is described by the T matrix elements, which can be connected to the S matrix elements using Eq. (3.47) and by applying the relativistic normalization [31, Reviews Chapter 50]:

$$\langle p'|p\rangle = (2\pi)^3 2E(p)\delta(\vec{p}' - \vec{p}) \tag{3.65}$$

$$E(p) = \sqrt{|\vec{p}|^2 + m^2}, \tag{3.66}$$

with $\vec{p}$ being the three-momentum, and m being the invariant mass of the state. This results in the following relation between the two matrix elements:

$$S(p_1, p_2; p_1', p_2') = (2\pi)^3 2E(\vec{p}_1 + \vec{p}_2)\delta(\vec{p}_1 + \vec{p}_2 - \vec{p}_1' - \vec{p}_2') \tag{3.67}$$

$$- i(2\pi)^4\delta(p_1 + p_2 - p_1' - p_2')\langle p_1', p_2'|\hat{T}|p_1, p_2\rangle, \tag{3.68}$$

with the T matrix element being defined as:

$$\langle p_1', p_2'|\hat{T}|p_1, p_2\rangle = T(p_1, p_2; p_1', p_2'). \tag{3.69}$$

To ensure Lorentz invariance, the so-called Mandelstam variables will be used from this point on. The Mandelstam variables can be defined via the four-momenta p_i and masses m_i as [42]:

$$s = (p_1 + p_2)^2 \tag{3.70}$$

$$t = (p_1 - p_3)^2 \tag{3.71}$$

$$u = (p_1 - p_4)^2 \tag{3.72}$$

$$s + t + u = m_1^2 + m_2^2 + m_3^2 + m_4^2. \tag{3.73}$$

For two-body scattering processes the total energy is given by $\sqrt{s}$ and the scattering angle is related to t, allowing for the matrix element $T(p_1, p_2; p_1', p_2')$ to be written in dependence of the Mandelstam variables as $T(s, t)$ [31, Reviews Chapter 50]. This Lorentz invariant representation of the T matrix element can now be used for all further discussions of the relativistic scattering problem.

3.2.1 Multi Channel Scattering

Until now only two particle scattering processes were considered, where the particles of the initial state $|p_1, p_2\rangle$ are the same as in the final state $|p_1', p_2'\rangle$, like in Fig. 3.1b. However, for the description of the processes which are analyzed in this work, it is necessary to include multiple channels, each containing two particles which participate in the scattering. The most general case is depicted in Fig. 3.1a, and one example for different incoming and outgoing channels can be seen in Fig. 3.1c.

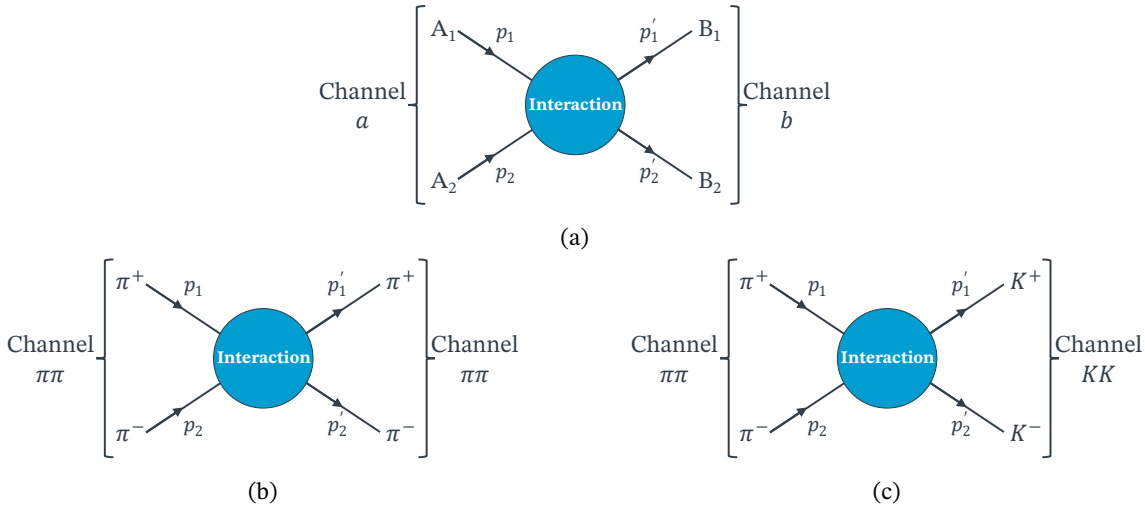

Figure 3.1: Schematic depictions of two-particle scattering processes. In (a) the process of an arbitrary channel a containing the particles A_1 and A_2 transitioning to a channel b containing the particles B_1 and B_2 is shown. In (b) and (c) the scattering of two specific channels is depicted. Figure (a) depict a scattering process for which the incoming and outgoing channels are the same. Figure (b) depicts a process in which the incoming $\pi\pi$ channel transitions to a KK channel.

Due to time symmetry and the cases where the interaction does not change the channel, every incoming channel a is also a possible outgoing channel b, and vice versa. The inclusion of multiple channels can be formalized by redefining the T matrix elements from Eq. (3.69) as follows [31, Reviews Chapter 50]:

$$\langle p_1', p_2'|\hat{T}|p_1, p_2\rangle \to \langle p_1', p_2'; b|\hat{T}|p_1, p_2; a\rangle = T_{ba}(s,t). \tag{3.74}$$

For a scattering process including the transitions depicted in Figs. 3.1b and 3.1c the T matrix which describes the entire process can then be written as:

$$T(s,t) = \begin{pmatrix} T_{\pi\pi,\pi\pi}(s,t) & T_{KK,\pi\pi}(s,t) \\ T_{\pi\pi,KK}(s,t) & T_{KK,KK}(s,t) \end{pmatrix}. \tag{3.75}$$

From this point on the relativistic T matrix elements can be connected to the cross section and parameterized using the partial wave method presented in Section 3.1.3. Explicit parameterizations for the T matrix elements will be presented in Section 3.2.4. A property that every parameterization has in common is its multi-valued character. Understanding the multi-valued

character of the T matrix elements is elementary for the extraction of physical quantities from the parameterizations. As such, the next section will give a general introduction into multi-valued complex functions.

3.2.2 Multi-Valued Complex Functions

To understand the multi-valued character of the T matrix element it is helpful to consider the definition of the square root first. The square root is inherently multi-valued, as it is defined as the solution of the equation $w^2 = x$. In case of a positive real argument inside the square root, it is possible to distinguish between two cases:

$$f_+ : \mathbb{R}^+ \to \mathbb{R}^+, x \mapsto +\sqrt{x} \tag{3.76}$$

$$f_- : \mathbb{R}^+ \to \mathbb{R}^-, x \mapsto -\sqrt{x}. \tag{3.77}$$

The two cases are shown in Fig. 3.2. For complex valued arguments, the definition is not as straight forward.
As the first step for understanding the properties of the complex square root, the complex coordinate z is transformed into polar coordinates, leading to the following definition:

$$f(z) = \sqrt{z} = \sqrt{|z|}e^{i\frac{\varphi}{2}}. \tag{3.78}$$

From this equation the multi-valued characteristic can directly be seen. When starting at an arbitrary point on the complex plane with the distance $|z|$ from the origin and an angle φ to the real axis and going along a full circle $\Delta\varphi = 2\pi$ around the origin, one ends up on the same point as before. But by using the substitution $\varphi \to \varphi + 2\pi$ for Eq. (3.78) the function changes the sign, leading to two possible values for the same point on the z plain.

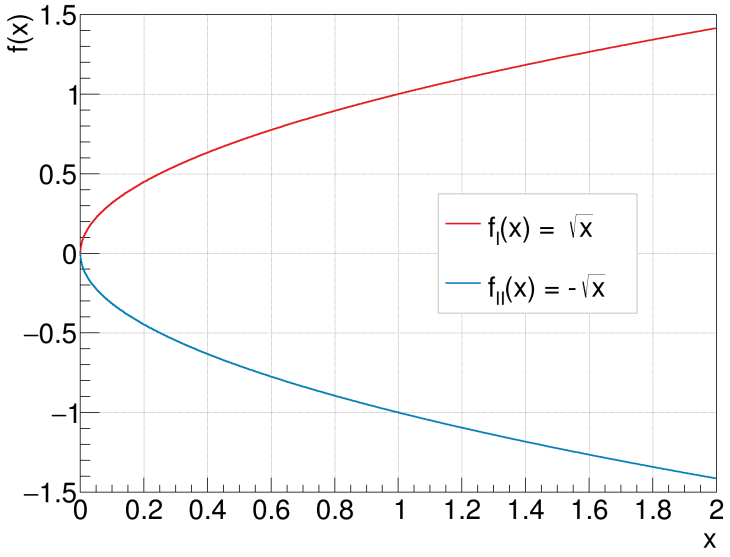

Figure 3.2: The two branches of the square root function with positive real arguments.

Characteristic points of multi-valued functions are the so-called branch points. A branch point is defined as a point where all neighboring points have more function values than the function at the point itself [43]. In the case of the square root the only branch point is the origin.
A possible solution to redefine multi-valued complex functions, so that they become single valued, is to set so-called branch cuts. Branch cuts stop functions from performing a 2π rotation on the complex plain by creating a border no function can pass. To achieve the wanted effect for the square root, the cut must start at the branch point at the origin and has to end at infinity. The shape or direction of the branch cut is completely arbitrary, but in scattering theory it is usually chosen to be along the positive real axis [43].

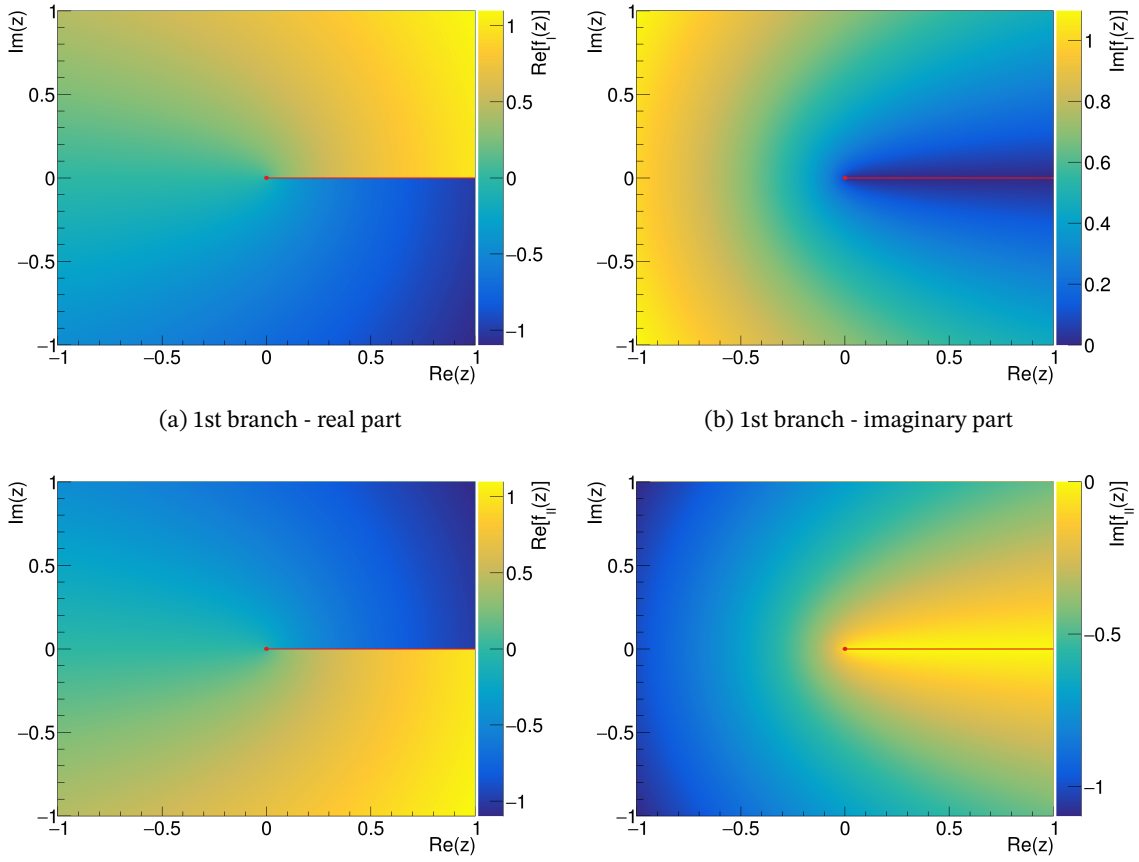

(a) 1st branch - real part

(b) 1st branch - imaginary part

(c) 2nd branch - real part

(d) 2nd branch - imaginary part

Figure 3.3: Real and imaginary parts of the two branches $f_{\mathrm{I}}(z)$ and $f_{\mathrm{II}}(t)$ of the square root function on the complex plane. The branch point of the square root is indicated as a red dot, and the chosen branch cut can be seen as a red line along the positive real axis. A 3d depiction of these plots can be seen in Fig. A.1.

Using this cut for the square root, again leads to two single valued functions, called the branches of the square root function. The two branches, as well as the branch cut of the square root function can be seen in Fig. 3.3. One chooses the first branch, also called principal branch, in such a way that $\sqrt{z} = +i\sqrt{|z|}$ holds for negative real z. When going back to

Eq. (3.78) this would mean, that the polar angle of the first branch is defined for $0 < \varphi \leq 2\pi$. The polar angle of the second branch is defined for $2\pi < \varphi \leq 4\pi$, completing the full cycle on the plane of the square root.
While the cut solves the ambiguity of the function, by design, the function becomes non-analytic along the cut, in this case for all positive real numbers. The problem with such non-analyticity is that the Cauchy integral and residue theorem, which are needed to extract the physical parameters from the T matrix elements, are no longer applicable. Methods for the extraction of these parameters will be presented in Section 3.2.3.
To overcome this problem one introduces an analytical continuation at the branch cuts. To achieve such a continuation, one defines the different branches of the square root not as different functions, but as different so-called Riemann sheets of that function [44]. By doing so, the Riemann sheet number k becomes a parameter of the function and the branch cut becomes a connection between the different Riemann sheets. If integrating along a path that crosses a branch cut, one now just changes the sheet, making the multi-valued function fully analytical. For example, the complex square root function would then become a fully analytical function with its two branches corresponding to two Riemann sheets.
Now that the analytical handling of multi-valued functions by introducing Riemann sheets has been established, the concept can be used for the discussion of the T matrix elements.

3.2.3 Properties of Reaction Amplitudes

The T matrix elements are reaction amplitudes describing the transition of a two-particle initial state into a two-particle final state. These kinds of reactions can be written as follows:

$$P_1 + P_2 \to R \to P_3 + P_4,$$

including possible resonances R appearing during the transition. Other reaction amplitudes will be introduced later, but the following applies for all of them. Reaction amplitudes are multi-valued functions on the complex s-plane. For the case of channels containing two particles, square root-like branch points appear at the two-particle production threshold of every channel, meaning the number of Riemann sheets doubles for every contributing channel. Poles of the reaction amplitude on the first Riemann sheet, also called the physical sheet, correspond to bound states, while poles on all other Riemann sheets, also called unphysical sheets, refer to resonances. For resonances, the poles on the unphysical sheet nearest to the physical one, contribute the most to the observable properties, like the measured cross section. So, it is crucial for the search of resonances to find the right unphysical sheet on the complex s plane, which smoothly connects to the physical sheet in the right energy region [31, Reviews Chapter 50].

The position of a pole corresponding to a resonance on the unphysical sheet of the complex s plane are model- and parameterization independent. From the position of the pole s_R, the physical mass M_R and width Γ_R of the resonance can be directly determined [31, Reviews Chapter 50]:

$$\sqrt{s_\mathrm{R}} = M_\mathrm{R} - i\Gamma_\mathrm{R}/2. \tag{3.79}$$

Another important property of the pole is its residue $\mathcal{R}_{ba}$, which for the T matrix element can be determined using Cauchy's residue theorem [44]:

$$\mathcal{R}_{ba} = -\frac{1}{2\pi i}\oint \mathrm{d}s T_{ba}. \tag{3.80}$$

With this residue, the parameter $\tilde{g}_a$ can be introduced, which gives the strength of the coupling of the pole to the channel a [31, Reviews Chapter 50]:

$$\tilde{g}_a = \mathcal{R}_{ba}/\sqrt{\mathcal{R}_{bb}}. \tag{3.81}$$

For narrow resonances, which only couple to channels, which energetically lie below the rest mass of the resonance, and which decay without angular momentum transfer (S-wave), the partial width for a two-body channel a can be defined as follows [31, Reviews Chapter 50]:

$$\Gamma_{\mathrm{R}\to a} = \frac{|\tilde{g}_a|^2}{M_R}\rho_a(M_\mathrm{R}^2), \tag{3.82}$$

with ρ_a being the two-body phase space factor, which is defined as [31, Reviews Chapter 49]:

$$\rho_a(s) = \frac{1}{8\pi}\frac{|\vec{p}_a|}{\sqrt{s}}. \tag{3.83}$$

The momentum of the two particles of channel a in their center-of-momentum frame is defined as [31, Reviews Chapter 49]:

$$|\vec{p}_a| = \frac{\sqrt{\lambda(s, m_{1,a}^2, m_{2,a}^2)}}{2\sqrt{s}}, \tag{3.84}$$

with $\lambda(x,y,z) = x^2 + y^2 + z^2 - 2xy - 2yz - 2xz$ being the Källén function [45]. The phase space factor, or rather the momentum contributing to this factor is the reason for the multi-valued character of reaction amplitudes. $|\vec{p}_a|$ has two branch points for complex s, one at the production threshold $s_\mathrm{th} = (m_1 + m_2)^2$, and one unphysical branch point at $s_\mathrm{unphy} = (m_1 - m_2)^2$. The branch point at the production threshold leads to the already mentioned doubling of Riemann sheets at each channel opening. How the unphysical branch points are treated will be explained at the end of the next section.

As mentioned before there are several ways to define a reaction amplitude. One of them is the production amplitude $\mathcal{A}_c$ for the two-particle decay channel c, which contains the particles C_1 and C_2. The production amplitude describes processes like:

$$P_1 + P_2 \to R + S \to (C_1 + C_2) + S,$$
$$I \to R + S \to (C_1 + C_2) + S,$$

introducing spectator particles S, which are produced together with the resonance, and single particle initial states I. The partial width of such a resonant production process can be calculated by [31, Reviews Chapter 50]:

$$\Gamma_{R\to a} = \frac{(2\pi)^4}{2M_R} \int |\mathcal{A}_a|^2 \mathrm{d}\Phi_a, \tag{3.85}$$

where $\int \mathrm{d}\Phi_a$ is the integral over the two-body phase space.
In the next section parameterizations for reaction amplitudes used in this work will be presented.

3.2.4 Amplitude Parameterizations

First the relativistic Breit-Wigner parameterization shall be introduced. It can be used for the description of narrow, isolated resonances. The corresponding decay amplitude reads [31, Reviews Chapter 50]:

$$\mathcal{A}_a(s) = \frac{\alpha \cdot g_a \cdot (p_a(s)/p_0)^l \cdot B_l(p_a(s)/p_0)}{M_{BW}^2 - s - iM_{BW}\Gamma(s)}. \tag{3.86}$$

If the nominal resonance mass lies above the production threshold of the channel a, then the energy-dependent width of the resonance can be written as follows:

$$\Gamma(s) = \Gamma_{BW} \cdot \frac{\rho_a(s)}{\rho_a(M_{BW}^2)} \cdot \left(\frac{p_a(s)}{p_a(M_{BW})}\right)^{2l} \cdot \left(\frac{B_l(p_a(s)/p_0)}{B_l(p_a(M_{BW})/p_0)}\right)^2. \tag{3.87}$$

The description of the components of this parameterization can be seen in Table 3.1.

Table 3.1: Description of the parameters and functions used in Eq. (3.86).

Parameter	Description
α	coupling strength to the resonance
g_a	coupling strength to channel a
p_0	scale parameter (0.2 GeV to 1 GeV)
l	relative angular momentum of channel a
M_{BW}	Breit-Wigner mass
Γ_{BW}	Breit-Wigner width
$B_l(p/p_0)$	Blatt-Weisskopf factors (Eq. (A.2))
$p_a(s)$	absolute momentum (Eq. (3.84))
$\rho_a(s)$	phase space factor (Eq. (3.83))

The s dependent momentum implements the correct behavior of the function at the production threshold, while the Blatt-Weisskopf factors compensate for the rapid growth of $(p_a)^l$ for $l > 0$.

As mentioned in the beginning of this section, the Breit-Wigner distribution can only describe narrow, isolated resonances. The Breit-Wigner parameters M_{BW} and Γ_{BW} only agree with the pole parameters M_R and Γ_R if there are no other resonances present in the partial wave of the channel, and if the resonance's line-shape is not distorted by uneven background levels, like at a production threshold. It also has to be mentioned that trying to describe multiple resonances in a channel as a sum of Breit-Wigner distributions leads to a violation of unitarity. Hence, a more sophisticated approach has to be used to describe more complex situations [31, Reviews Chapter 50].

By using the definition of the partial K matrix element in Eq. (3.63) and generalizing it for the multi-channel case, it is possible to construct a reaction amplitude, which guarantees unitarity. Analogously to Eq. (3.59) one can define the unitary T matrix as [31, Reviews Chapter 50]:

$$T = n\left[\mathbb{1} - i\rho K n^2\right]^{-1} K n, \tag{3.88}$$

with ρ being the diagonal phase space matrix with elements $\rho_{aa} = \rho_a(s)$ (cf. Eq. (3.83)), and n being a diagonal matrix, where the matrix elements are defined as:

$$n_{aa} = (p_a(s)/p_0)^l \, B_l(p_a(s)/p_0). \tag{3.89}$$

As for the Breit-Wigner parameterization, n incorporates the threshold and high energy behavior for partial waves with $l > 0$. One possible parameterization for the K matrix, being a hermitian solution of Eq. (3.63), is:

$$K_{ba}(s) = \sum_{\mathrm{R}} \frac{g_b^{(\mathrm{R})} g_a^{(\mathrm{R})}}{m_{\mathrm{R}}^2 - s} + \sum_{i=1}^{N_{\mathrm{NR}}} b_{ba}^{(i)} s^i, \tag{3.90}$$

where $g_a^{(\mathrm{R})}$ and $g_a^{(\mathrm{R})}$ are the coupling strengths between a resonance R and a channel a, and channel b respectively, m_{R} is the so called bare mass of R, and $b_{ab}^{(i)}$ are non-resonant coupling parameters [31, Reviews Chapter 50]. In order for the K matrix to be hermitian, leading to a unitary T matrix, all aforementioned parameters need to be real. This definition of the K matrix consists of two parts, the first part being the resonant one, describing the resonant scattering from channel a to channel b and being deeply connected to the poles of the T matrix. The second part consists of a polynomial whose order is given by N_{NR}, and which describes the non-resonant part of the scattering process.

Due to the multi-channel character of this parameterization, it is possible that the momentum p_a has to be calculated in the unphysical region below the production threshold of channel a. To stay on the physical sheet, one may employ the analytic continuation:

$$p_a = i\sqrt{p_a^2}, \text{ for } p_a^2 < 0. \tag{3.91}$$

This continuation results in Flatté-like line-shapes around the threshold [46].

The K matrix approach can now be modified in order to parameterize production amplitudes. So instead of a channel of two particles scattering into two particles, the amplitudes describe the production of a two-particle channel c resulting from the decay of one particle. One possible parameterization uses the so-called projection vector [31, Reviews Chapter 50]:

$$P_c = \sum_{\mathrm{R}} \frac{\alpha^{(\mathrm{R})} g_c^{(\mathrm{R})}}{m_{\mathrm{R}}^2 - s} + \sum_{i=0}^{\tilde{N}_{\mathrm{NC}}} \tilde{b}_c^{(i)} s^i. \tag{3.92}$$

The elements of the projection vector exhibit the same resonant, and non-resonant structure as the K matrix, but only in respect to a decay channel c. It also contains the new parameter $\alpha^{(R)}$, which gives the resonance's production strength. Analogously to Eq. (3.88), the production amplitude can be defined as

$$\vec{\mathcal{A}}(s) = n\left[\mathbb{1} - i\rho K n^2\right]^{-1} \vec{P}. \tag{3.93}$$

Again, for the amplitude to be unitary, $\alpha^{(R)}$ and $\tilde{b}_c^{(i)}$ have to be real.
One problem with the parameterizations presented in Eqs. (3.88) and (3.93) is the behavior of the phase space factor ρ_a below the production threshold of channel a. The factor is non-analytical at $s = 0$ (c.f. Eq. (3.83)) and due to its branch point at $s_{\mathrm{unphy}} = (m_1 - m_2)^2$ develops an unphysical cut at positive energies for two-particle channels with unequal masses. As a solution, one can substitute the arguments of the phase space matrix $-i\rho_a$ with the so called Chew-Mandelstam functions Σ_a, which are defined to have the same imaginary part above threshold, but are fully physical and analytical [47]. The Chew-Mandelstam functions are defined as follows:

$$\begin{aligned}\Sigma_a(s) = \frac{1}{16\pi}\Bigg[& \frac{2p_a}{\sqrt{s}} \log\left(\frac{m_{1,a}^2 + m_{2,a}^2 - s + 2\sqrt{s}p_a}{2m_{1,a}m_{2,a}}\right) \\ & - (m_{1,a}^2 - m_{2,a}^2)\left(\frac{1}{s} - \frac{1}{(m_{1,a}+m_{2,a})^2}\right)\log\left(\frac{m_{1,a}}{m_{2,a}}\right)\Bigg]\end{aligned} \tag{3.94}$$

The fully analytical amplitude then reads:

$$\vec{\mathcal{A}}(s) = n\left[1 + \Sigma K n^2\right]^{-1} \vec{P}, \tag{3.95}$$

with Σ being a diagonal matrix containing the Chew-Mandelstam functions $\Sigma_{aa} = \Sigma_a(s)$.
With these definitions, the only thing missing for a complete treatment of the two-particle scattering problem is the incorporation of the spin. For this, the next chapter will introduce the helicity formalism.

3.2.5 Helicity Formalism

Several reactions relevant for this work contain particles with excited angular momenta J. The angular momentum directly influences the angular distribution of the final state particles, and thus it is of utmost importance to find a model that introduces angular dependence into the reaction amplitude.

One possible representation that can be used for relativistic scattering and production processes is the helicity formalism. In the center of this formalism stands the name-giving helicity operator, which is defined as:

$$h = \frac{\vec{J}\,\vec{p}}{|\vec{p}|}, \tag{3.96}$$

with $\vec{J}$ and $\vec{p}$ being the total angular momentum and linear momentum [48].
The helicity operator has relativistic eigenstates together with either the total angular momentum operator $\hat{\vec{J}}$, or the momentum $\hat{\vec{p}}$, and the moduli of its eigenstates are conserved in relativistic processes. As an example, one can now construct the reaction amplitude of the angular momentum eigenstates for the reaction $R \to P_1 + P_2$, in the rest frame of the initial state R, as follows:

$$A(\vec{p}_f) = \langle \vec{p}_f, \lambda_1; -\vec{p}_f, \lambda_2 | \hat{U} | J, \tilde{\lambda} \rangle \,, \tag{3.97}$$

with $\vec{p}_f$ and $\lambda_{1,2}$ being the momentum and helicity eigenvalues of the final state, containing P_1 and P_2, and J and $\tilde{\lambda}$ being the total angular momentum and helicity eigenvalues of the initial state R. $\hat{U}$ is the time-evolution operator, which describes the transition between the states, and can be substituted with the scattering operator $\hat{S}$ in the case of asymptotic initial and final states [48].
Because the absolute momenta of the final state particles have to be identical, and the momentum vectors must be anti-parallel in the rest frame of the initial state R, it is possible to fully define the amplitude using the polar and azimuthal angles θ and φ. Hence, the amplitude can be written as:

$$A(\theta, \varphi) = \langle \theta, \varphi, \lambda_1, \lambda_2 | \hat{U} | J, \tilde{\lambda} \rangle \,. \tag{3.98}$$

The reference frame for the angles is called the helicity frame. The z axis is defined in the direction of the momentum of the mother particle R, while the orthogonal x and y axes are arbitrary chosen to be in the laboratory frame, with y being in vertical direction. The resulting reference frame with the corresponding angles for P_1 can be seen in Fig. 3.4 [48].
To further simplify the amplitude, a complete set of helicity final states, with a total angular momentum of j and helicity $\tilde{\lambda}'$, can be inserted into Eq. (3.98). Then by using the orthogonality of the angular momentum states, one gets:

$$\begin{aligned} A(\theta, \varphi) &= \sum_{j, \tilde{\lambda}', \lambda_1', \lambda_2'} \langle \theta, \varphi, \lambda_1, \lambda_2 | j, \tilde{\lambda}', \lambda_1', \lambda_2' \rangle \langle j, \tilde{\lambda}', \lambda_1', \lambda_2' | \hat{U} | J, \tilde{\lambda} \rangle & (3.99) \\ &= \sum_{j, \tilde{\lambda}', \lambda_1', \lambda_2'} \langle \theta, \varphi, \lambda_1, \lambda_2 | j, \tilde{\lambda}', \lambda_1', \lambda_2' \rangle \, \delta_{\tilde{\lambda}', \tilde{\lambda}} \delta_{j,J} A_{\lambda_1', \lambda_2'} & (3.100) \\ &= \sum_{\lambda_1', \lambda_2'} \langle \theta, \varphi, \lambda_1, \lambda_2 | J, \tilde{\lambda}, \lambda_1', \lambda_2' \rangle A_{\lambda_1', \lambda_2'}, & (3.101) \end{aligned}$$

with $A_{\lambda_1', \lambda_2'}$ being the constant helicity amplitude, which gives the coupling between the initial state and the helicity states of the final state particles. This result can be further simplified by using the complex conjugate of the Wigner D-matrix, which describes the transformation of angular momentum eigenstates under rotation.

By using Eq. (A.4) the amplitude can be written as [48]:

$$A(\theta,\varphi) = \sqrt{\frac{2J+1}{4\pi}} \cdot D^{J*}_{\tilde{\lambda},\lambda_1-\lambda_2}(\varphi,\theta,-\varphi) A_{\lambda_1,\lambda_2}. \tag{3.102}$$

While this approach is Lorentz invariant, the helicity states are not eigenstates of the parity operator and thus do not conserve parity. In the following a definition for the reaction amplitude $A(\theta,\varphi)$ will be derived which intrinsically conserves parity.

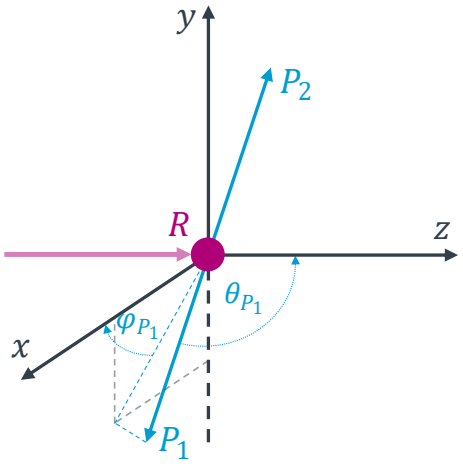

Figure 3.4: The polar angle θ and the azimuthal angle φ of P_1 from the decay $R \to P_1 + P_2$ in the helicity frame. In this frame the particle R is resting, the light magenta arrow indicates the momentum direction of R in the laboratory frame.

If l and s are good quantum numbers of the process $R \to P_1 + P_2$, it is possible to use Eq. (A.3) to get:

$$|J,\tilde{\lambda},\lambda_1,\lambda_2\rangle = \sum_{l,s} \sqrt{\frac{2l+1}{2J+1}} \langle l,0;s,\lambda|J,\lambda\rangle \langle s_1,\lambda_1;s_2,-\lambda_2|s,\lambda\rangle |J,\tilde{\lambda},l,s\rangle, \tag{3.103}$$

with $\lambda = \lambda_1 - \lambda_2$, s_1 and s_2 being the spins of the daughter particles, and $\langle l,0;s,\lambda|J,\lambda\rangle$ and $\langle s_1,\lambda_1;s_2,-\lambda_2|s,\lambda\rangle$ being Clebsch-Gordan coefficients [49]. Inserting this relation into Eq. (3.99) results in:

$$\begin{aligned} A(\theta,\varphi) = & \sum_{j,\tilde{\lambda}',l,s,\lambda_1',\lambda_2'} \langle \theta,\varphi,\lambda_1,\lambda_2|j,\tilde{\lambda}',\lambda_1',\lambda_2'\rangle \sqrt{\frac{2l+1}{2j+1}} \\ & \cdot \langle l,0;s,\lambda'|j,\lambda'\rangle \langle s_1,\lambda_1';s_2,-\lambda_2'|s,\lambda'\rangle \langle j,\tilde{\lambda}',l,s|\hat{U}|J,\tilde{\lambda}\rangle, \end{aligned} \tag{3.104}$$

$$\begin{aligned} = & \sum_{j,\tilde{\lambda}',\lambda_1',\lambda_2',l,s} \langle \theta,\varphi,\lambda_1,\lambda_2|j,\tilde{\lambda}',\lambda_1',\lambda_2'\rangle \sqrt{\frac{2l+1}{2j+1}} \\ & \cdot \langle l,0;s,\lambda'|j,\lambda'\rangle \langle s_1,\lambda_1';s_2,-\lambda_2'|s,\lambda'\rangle \delta_{\tilde{\lambda}',\tilde{\lambda}} \delta_{j,J} A_{l,s}, \end{aligned} \tag{3.105}$$

$$\begin{aligned} \overset{\text{Eq. (A.4)}}{=} & \sum_{l,s} \sqrt{\frac{2l+1}{4\pi}} \cdot D^{J*}_{\tilde{\lambda},\lambda}(\varphi,\theta,-\varphi) \cdot \langle l,0;s,\lambda|J,\lambda\rangle \\ & \cdot \langle s_1,\lambda_1;s_2,-\lambda_2|s,\lambda\rangle \cdot A_{l,s}, \end{aligned} \tag{3.106}$$

with $A_{l,s}$ being the constant canonical amplitude [49]. This definition of the angular dependent reaction amplitude now intrinsically incorporates Lorentz invariance, as well as parity conservation. Together with the parameterizations of the energy dependent reaction amplitudes presented in Section 3.2.4, the total reaction amplitude for a relativistic two body scattering processes can be defined.

This concludes the theory part of this thesis. The concepts introduced in the last chapters lay the groundwork for the following analysis of reactions detected by the BESIII detector. The next chapter will now go into detail about the experimental setup, which was used for the collection and processing of the data analyzed in this work.

4. Experimental Setup

In this chapter, the soft- and hardware components used for data acquisition, processing and analysis will be presented. The data acquisition is facilitated by the BESIII (Beijing Spectrometer III) experiment at the Institute of High Energy Physics (IHEP). All different acceleration and detection systems will be introduced, giving information about their general architecture and design parameters. Then the soft- and hardware used for the different steps of the analysis will be specified, starting with the framework used at the BESIII computing platform. Subsequently, the data and Monte-Carlo (MC) samples used in this work will be presented. And finally, the framework used for the analysis outside the BESIII computing platform will be introduced.

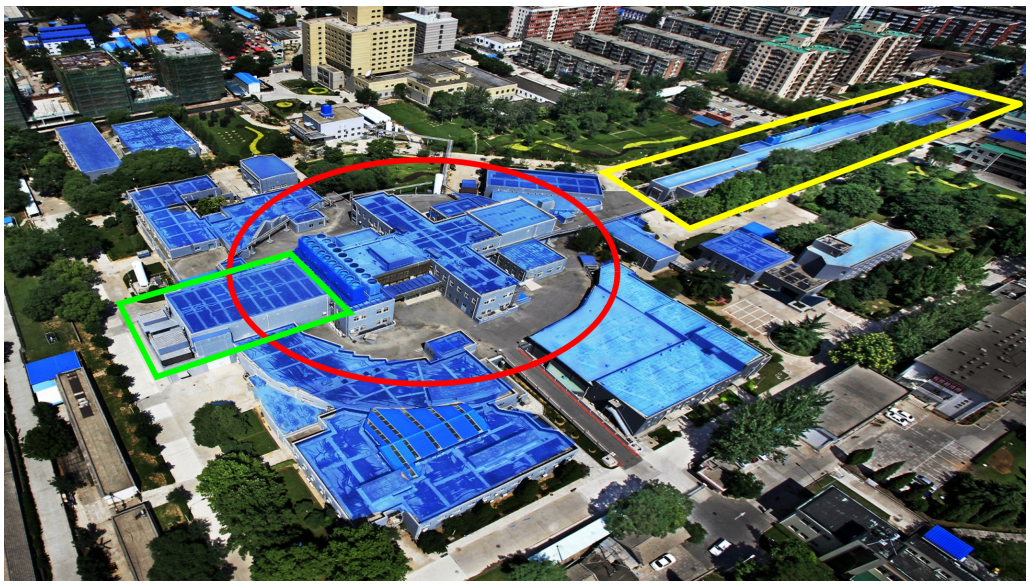

Figure 4.1: Areal view of the research facility containing the LINAC (yellow), the BEPCII collider ring (red), and the BESIII experiment (green). Adapted from Ref. [50].

4.1 Data Acquisition

All data analyzed in this work was collected by the BESIII experiment, detecting particles created in electron positron collisions at the IHEP of the Chinese Academy of Sciences in Beijing. The research facility can be seen in Fig. 4.1. Data acquisition can be split into two steps, which both will be presented in the next sections. Step one is the acceleration and collision of electrons and positrons, facilitated by the BEPCII (Beijing Electron Positron Collider II). The second step is the detection of the particles resulting from the collision by the BESIII detector.

4.1.1 BEPCII

Before collisions at high energies can occur, the electrons and positrons must be accelerated. The acceleration and collision process takes place at the BEPCII. In the first step, a linear accelerator (LINAC) accelerates electrons and positrons up to 1.89 GeV and injects electrons with a rate of 200 mA/min and positrons with 50 mA/min into the collider rings [51]. The collider itself consists of two separate rings, one for electrons and one for positrons, which circulate through the rings in opposite directions. In the rings, 93 bunches can be stored, which can be brought to collision at the interaction point with a horizontal crossing-angle of ± 11 mrad [51]. The BEPCII is designed for center-of-mass energies between 2 GeV and 4.6 GeV, with an optimized luminosity at 2×1.89 GeV of $1 \cdot 10^{33}\,\mathrm{cm}^{-2}\mathrm{s}^{-1}$ [51]. Through several updates after the commissioning, to date, center-of-mass energies up to almost 5 GeV are possible [19, 52]. All design parameters of the BEPCII are listed in Table A.1, and a schematic drawing of the collider ring can be seen in Fig. 4.2.

4.1.2 BESIII

Using the beams provided by BEPCII, the BESIII detector is designed to collect high precision and high statistics data in the τ-charm energy region. The detector system is built symmetric around the interaction point, covering 93 % of the solid angle [51]. As depicted in Fig. 4.3, the spectrometer consists of multiple layers of detector systems, which will be explained in detail in the next subsections. A superconducting solenoid, that provides an magnetic field of 1 T, is positioned between the electromagnetic calorimeter and the muon identifier. The corresponding magnetic flux return yoke is located in the outer layer of BESIII with the muon identifier between its steel plates.

Multilayer Drift Chamber

The multilayer drift chamber (MDC) is the nearest detector system to the interaction point. It encases the beam pipe, starting at in inner radius of 59 mm and ending at an outer radius of 810 mm [51]. The chamber is filled with a 60:40 He/C_3H_8 gas mixture and 43 radially distributed layers of azimuthal distributed wires [51]. While the ionization of the gas allows for

an energy loss measurement, the wires detecting the ionized gas also provide information on the positions of particles. Thus, this detector allows for the reconstruction of the paths of charged particles, as well as the measurement of their momentum and energy loss. Radially, the position of a particle can be measured with a resolution of 130 µm, while the resolution along the beam pipe is approximately 2 mm [51]. The uncertainty of the momentum measurement is 0.5 % and that of the energy loss amounts to 6 % [51]. The detector is also used for the reconstruction of hadrons with long enough lifetimes, that they decay inside the detector volume, like the K_S^0 meson, or the Λ baryon. Reconstructed charged tracks can also be extrapolated to provide positional information in the outer detectors, and can be used as a trigger signal to reject background tracks.

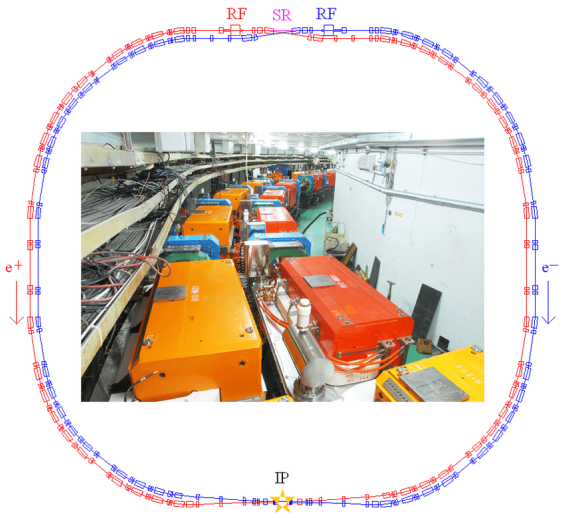

Figure 4.2: Schematic drawing of the BEPCII collider ring, with a picture in the middle of some of the ion optics elements along the beam lines. The orange elements are dipole magnets, and the blue ones are quadrupoles. These magnets can also be seen as rectangles in the schematic drawing. The positions of the radio frequency cavities (RF), the interaction point (IP), and the synchrotron radiation monitor (SR) are marked in the schematic drawing. Also indicated are the circulation directions and corresponding beam pipes, of the positrons and electrons. Figure taken from Ref. [53].

Time-of-Flight System

The time-of-flight (TOF) system consists of a barrel and two end caps. The barrel has two layers of 88 staggered trapezoidal plastic scintillators, while the end caps are each built up from a single layer of 48 fan-shaped scintillators [51]. Fine mesh photomultiplier tubes are attached to each of the 5 cm thick counters [51]. This design allows for a time resolution of 68 ps in the barrel [52] and 60 ps in the end caps [55], but leaves a blind spot for polar angles with $0.83 < |\cos\theta| < 0.85$ [51]. The TOF system is used as a trigger for charged particles and can be used together with the information from the MDC for particle identification. This is particularly useful for the separation of charged kaons and pions.

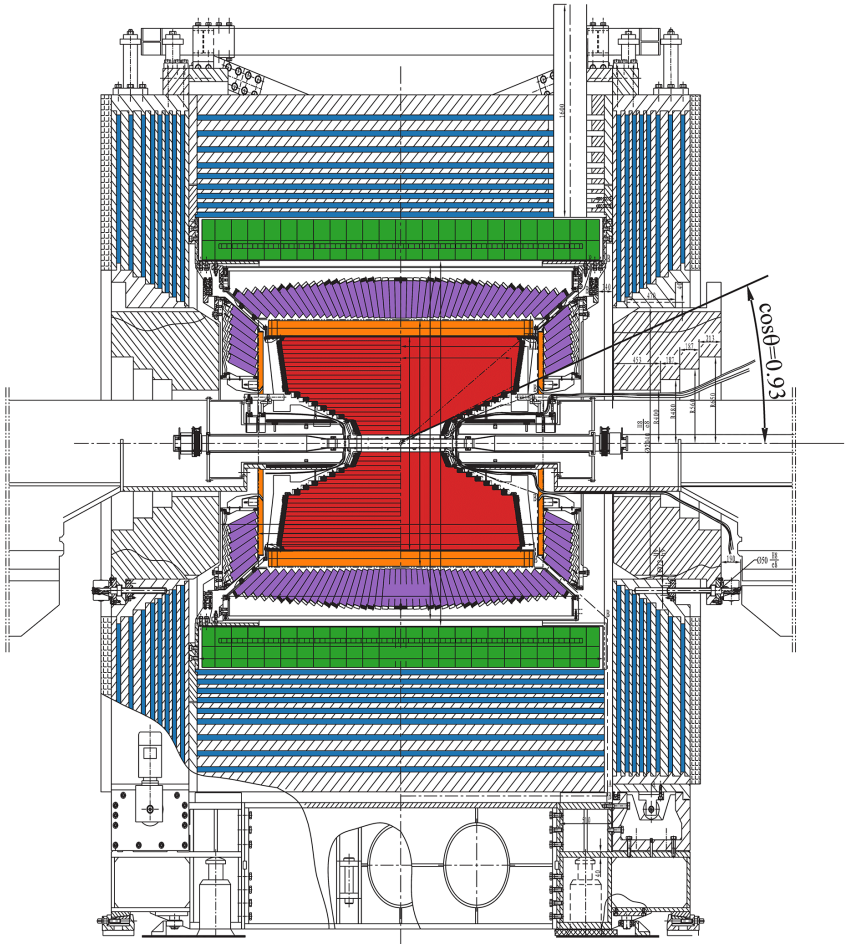

Figure 4.3: Schematic drawing of the BESIII detector. The distinct parts of the spectrometer are colored as follows: Multilayer drift chamber (red), time-of-flight system (orange), electromagnetic calorimeter (purple), superconducting solenoid (green), muon identifier (blue). Also depicted is the maximum polar angle at which the multilayer drift chamber and electromagnetic calorimeter can detect particles. Adapted from Ref. [51].

Electromagnetic Calorimeter

The electromagnetic calorimeter (EMC) consists of 6240 CsI(Tl) crystals placed between the TOF system and the solenoid coil [51]. This sub-detector provides an angular coverage of $|\cos\theta| < 0.83$ for the barrel part, and of $0.85 < |\cos\theta| < 0.95$ for the end caps [51]. Photons, which are produced in the scintillators by electromagnetic showers, are then detected by photo diodes, which are attached to the ends of the crystals. With this design, the detection of photons and electrons with energies between 20 MeV and 2 GeV is made possible [51]. In this range, it reaches energy resolutions of 2.5% at 1 GeV and 4 % at 100 MeV [51]. Due to its layered crystal arrangement, the EMC also possesses an energy dependent position resolution of under $6\,\text{mm}/\sqrt{E(\text{GeV})}$ [51]. With these parameters, an accurate separation of electrons and charged pions is realized, and the precise reconstruction of the invariant mass of the π^0 is made possible.

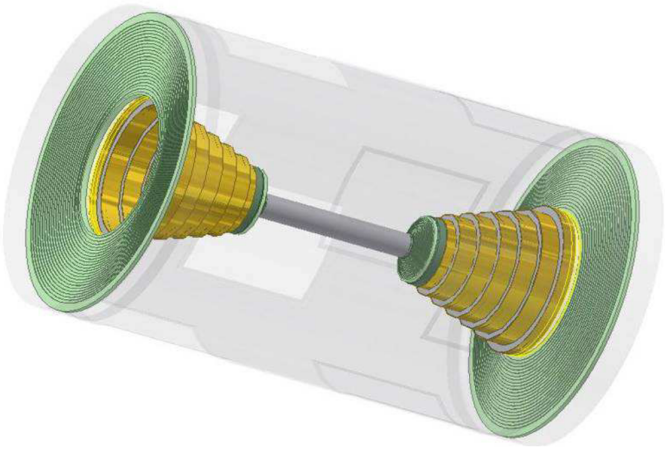

Figure 4.4: Schematic view of the multilayer drift chamber. Figure taken from Ref. [54].

Muon Identifier

Outside the solenoid coil and inside the flux return yoke, the resistive plate counters (RPC) of the muon detector are located. Nine layers of RPCs are placed between the yoke's steel plates at the barrel, and eight layers are placed in the end caps [51]. To provide position information, the RPCs have 4 cm wide readout strips in polar and azimuthal direction, in which the momentum of muons can be measured [51]. Muons can be identified via the RPCs, starting at a cut-off momentum at 400 MeV, using the track reconstruction of the MDC and the energy measurement of the EMC [51].

Trigger & Data Acquisition Systems

The trigger and data acquisition (DAQ) systems are designed to read out and process data taken by all the detector systems in the 8 ns between bunch collision. A two-level trigger system is employed to reduce the data traffic by filtering out background reactions. The hardware trigger uses the trigger information of the MDC, TOF, and EMC sub-triggers to reduce cosmic ray, and beam related background events. To ensure (nearly) dead-time free data processing, the read-out electronics operate at a frequency of 41.65 MHz and are synchronized with the RF cavities of the LINAC [51]. The DAQ system then collects the data from all the sub-detector systems, sending them to a computer cluster. After reaching the cluster, the data gets reconstructed and filtered by the software trigger system. Then the remaining reconstructed events get written down into permanent storage with a final event rate of about 2 kHz signal events, and 1 kHz background events [51].

4.2 Analysis Framework

After the acquisition of data, multiple steps of data processing and analysis follow. The next sections will introduce the different soft- and hardware components used in this work.

4.2.1 Computing at the IHEP Grid

The first steps are performed on the BESIII computing platform, which includes the IHEP computing grid in Beijing [56], as well as remote connections to multiple other high performance computing clusters in China. Data processing and analysis, as well as the simulation of Monte-Carlo (MC) events, are implemented using the GAUDI based BESIII offline software system (BOSS) [57, 58]. Information about the detector material and geometry, and the strength of the magnetic field inside the detectors, are contained within BOSS.
To generate Monte-Carlo events, the software package KKMC is used in the framework of BesEvtGen, which includes a wide range of generation models [59, 60]. First, the KKMC package is used to simulate the production of $c\bar{c}$ states, including initial state radiation effects. Then, the models included in BesEvtGen are used to simulate the decay processes of the $c\bar{c}$ states, including final state radiation effects. The thus generated events are then fed into a detector simulation created with the Geant4 based BESIII object-oriented simulation tool (BOOST) [61, 62].
For data events, as well as simulations, the BOSS framework provides the possibility to select specific events from the raw reconstructed samples. For this purpose, the final state filter (FSFilter) software tool, written by Ryan Mitchel, was used. The tool allows for the selection of events which belong to a given set of final state particles, using the information proved by the detectors, and incorporating the results of particle identification, as well as vertex and kinematic fits. More information on the event selection can be found in Chapter 5. Selected events are then written into ROOT files, which can be used for further analysis.

4.2.2 BESIII Datasets & Simulations

For this work, the 2021 $\psi(2S)$ data set was used, containing (2.264 ± 0.009) billion $\psi(2S)$ events [63, internal communication]. For simulations, 5 million events each were generated for the reactions:

$$\psi(2S) \to (\phi \to K^+K^-)\pi^+\pi^-,$$
$$\psi(2S) \to (\phi \to K^+K^-)\pi^0\pi^0,$$

using the BesEvtGen "PHSP" model, which generates all reactions evenly distributed in their phase space [60]. From now on, these two Monte-Carlo samples will be referred to as signal

Monte-Carlo. Additionally, about 10 million events each were generated for the reactions:

$$\psi(2S) \to K^+K^-\pi^+\pi^-,$$
$$\psi(2S) \to K^+K^-\pi^0\pi^0,$$

using the "PhspStpf" model, which also generates reactions evenly distributed in their phase space, but allows for an invariant mass window, in which events are generated (N. Hüsken, private communication, August 19, 2022). In this case, a mass window for the two-kaon system was chosen to be $0.9\,\text{GeV} < m(KK) < 1.1\,\text{GeV}$. Furthermore, 41 million events of the reaction $\psi(2S) \to K^+K^-\pi^+\pi^-$ were generated using the "PHSP" model. These three Monto-Carlo samples will be referred to as phase space Monte-Carlo. The exact number of generated Monte-Carlo events can be found in Table A.2.
In addition to these exclusive Monte-Carlo samples, one inclusive Monte-Carlo sample, containing all listed reactions, was used for each final state. Listed reactions are included in these samples using the physical properties provided by the PDG, and EvtGen models, while reactions with unknown branching fractions are generated using the Lundcharm model [64–66]. In this work, 0.5 billion inclusive Monte-Carlo $\psi(2S)$ events, provided by the BESIII collaboration, were used. The reconstruction and initial event selection of all aforementioned samples was performed in BOSS version 7.0.7p1.

4.2.3 Analysis Software and Hardware

After selecting the data and simulation samples on the IHEP cluster, the results are accessible as ROOT-files. ROOT is an object-oriented computation framework, using the C++ interpreter cling [67, 68]. It is specialized for the fast handling and analysis of high statistics data samples, and thus was used for a significant part of the analysis.
As part of this work, a partial wave analysis (PWA) was performed using the object-oriented partial wave interactive analysis software (PAWIAN), which is written in C++ [69]. PAWIAN is highly customizable, allowing for the implementation of the models described in Chapter 3. For fitting, PAWIAN, as well as ROOT, use the minimization package MINUIT2, which is a C++ package based on the FORTRAN package MINUIT [70, 71]. Due to the considerable number of data points and fit parameters used in PWAs, an equivalently large amount of computation power is needed to get results in a reasonable time. For efficient computations, PAWIAN uses MPI (massage passing interface), and OpenMP (Open Multi-Processing) parallelization methods, allowing for the parallel fitting of data on multiple processors and processor cores. To use the full potential of such parallelization, PAWIAN computations were performed on the PALMA II ("Paralleles Linux-System für Münsteraner Anwender") computer cluster, located in Münster, which includes over 18000 processor cores amounting to a computing power of over 800 TFlops.
This concludes this chapter, introducing the hard- and software used to acquire, process, and analyze data, and generate and simulate MC samples. In the next two chapters, the presented tools will be used to perform a rigorous analysis of the data, starting with the event selection.

5. Initial Event Selection

This chapter will show the steps taken to create the data and Monte-Carlo samples, which will be analyzed in the next chapter, using the software tools introduced in the previous chapter. In Section 4.2.1 it was mentioned that custom selection criteria can be introduced, when converting the raw data into ROOT files using the FSFilter software tool. Possible final state particles, implemented by the FSFilter are: $\Lambda, \bar{\Lambda}, e^{\pm}, \mu^{\pm}, p, \bar{p}, \eta, \gamma, K^{\pm}, K_S^0, \pi^{\pm}$, and π^0.
For this work the two final states

$$K^+K^-\pi^+\pi^-,$$

$$K^+K^-\pi^0\pi^0,$$

were chosen to be analyzed. The next sections will go into detail for the selection criteria applied for charged tracks, and neutral particles. These criteria were chosen to maximize the probability, that the events in the data set correspond to the aforementioned final state particles, resulting from the decay of $\psi(2S)$.

5.1 Charged Track Selection

As the first step, all charged tracks belonging to an event have to be identified as specific particles. For this purpose, the particle identification (PID) system assigns a probability to each charged track for it to be a $e^{\pm}, \mu^{\pm}, \pi^{\pm}, K^{\pm}, p$, or $\bar{p}$. To calculate this probability, the PID system uses the measured momentum in the MDC, and the time-of-flight determined by the TOF system. The only requirement for a track to be identified as one of the aforementioned particles is that the probability for the particle hypothesis is higher than 10^{-5}, meaning that one charged track can be identified as multiple particles. Due to the geometry of the detector system, no charged tracks with a polar angle of $|\cos\theta| > 0.93$ are accepted. All charged tracks fulfilling the previously mentioned criteria are written into a list, with their corresponding particle hypotheses. All selection criteria for charged tracks can be found in Table A.3.

5.2 Neutral Particle Selection

Multiple restrictions are implemented to maximize the ratio between photons, resulting from the decay of the π^0 final state particles, and other neutral tracks. For a neutral particle to be accepted, the time between the start of the event and the detection of the showers in the EMC, resulting from said particle, has to be shorter than 700 ns. All neutral particles coming from the collision should be detected after this time, resulting in a reduction of neutral background events coming from other sources if this criterion is applied. Additionally, the particles are required to deposit an energy of above 25 MeV in the barrel part of the detector ($|\cos\theta| < 0.8$), or above 50 MeV in the end caps ($0.86 < |\cos\theta| < 0.92$). This criterion is applied to account for the geometry of the detector, only accepting particles which have angles that lie within the detection range and implements a higher energy threshold for the less sensitive end caps. Another requirement is that the angle between the neutral particles and the next charged track has to be larger than 10°, to reduce the photon background, resulting from the interaction of charged particles with matter.
For the final states analyzed in this work, all photons have to be produced in $\pi^0 \to \gamma\gamma$ decays. Given this restriction, every combination of two accepted neutral particles is written into a list as a possible π^0 candidate.
For every event now exists a list of possible final state particles, from which the desired final state can be assembled. Because some tracks appear multiple times on that list, the only restriction for the combination of particles is, that no track appears more than once in the final state. All selection criteria for neutral particles can be found in Table A.4.

5.3 Vertex Fit

Due to the width of the electron and positron beams, the exact position, at which the collision takes place, is unknown. To determine the position of this so-called primary vertex, a vertex fit is performed if at least two charged tracks form a common vertex. The fit varies the parameters of the reconstructed charged tracks within their uncertainties to form a common vertex that has a minimal distance d to the interaction point, which is given for each run. This fit yields the position of the primary vertex and updates the three-momenta of the contributing particles. Assuming only short-lived resonances, one expects the primary vertex to be near to the interaction point. Thus, it is required that all resulting vertices have to be inside a cylindrical volume around the interaction point, with a height of 20 cm in the direction of the beam pipe, and a radius of 1 cm perpendicular to the beam pipe. A depiction of the primary vertex, as well as the cylindrical volume, can be seen in Fig. 5.1.

5.4 Kinematic Fit

In the last step of the final state reconstruction, the four-momenta of the selected final state particles are varied within their uncertainties, to fit the four-momentum of the initial $\psi(2S)$ state. This kinematic fit thus is constrained to conserve momentum and energy. For each π^0 contained in the final state, an additional constraint is added for the invariant mass of the two-photon system corresponding to the neutral pion.
The four-momenta determined in this way are then written to a ROOT-file along with all the parameters used for the selection criteria and determined by the fits. But there still exist multiple entries of possible final state combinations per event. For the following analysis, for each event, only the entry with the lowest χ^2_{NC} was accepted, with χ^2_{NC} being the goodness-of-fit resulting from the kinematic fit with a certain number of constraints (NC). A detailed explanation of the χ^2 value can be found in Appendix A.1.7. For the $\pi^+\pi^-$ final state the number of constraints is N = 4, while the $\pi^0\pi^0$ final state has six constraints.

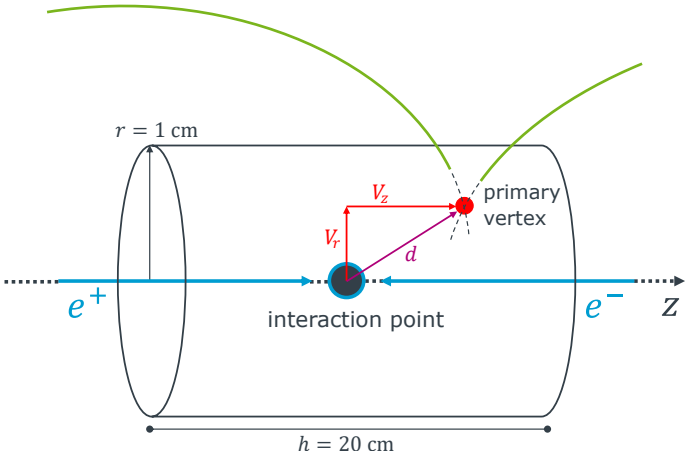

Figure 5.1: Schematic representation of the primary vertex resulting from two tracks, and the cylindrical volume around the interaction point, in which vertices are accepted.

6. Analysis

In this chapter, the methods used to analyze the $K^+K^-\pi\pi$ final states will be presented, and the obtained results will be discussed. The first section focuses on the selection of signal events, containing the reactions $\psi(2S) \to \phi\pi\pi$ and $\psi(2S) \to \phi(X \to \pi\pi)$, with an arbitrary intermediate resonance X. A method will be shown to maximize the signal yield from the data sample, using the fit quality of the kinematic fit. Then, a model will be introduced to separately determine the signal and background contributions in the K^+K^- invariant mass spectrum around the ϕ resonance. Using the results of the model, the branching ratios for the reactions $\psi(2S) \to \phi\pi\pi$ will be determined, and a signal region around the ϕ resonance will be selected. This signal region will be optimized using a similar method, as for the fit quality of the kinematic fit, and only events inside this region will be used for the subsequent analysis. Finally, background studies using the inclusive Monte-Carlo samples will be performed, leading to the implementation of a veto region around the $K^*(892)$ resonance in the $K\pi$ invariant mass spectra. Events inside this veto region will be rejected, concluding the signal selection.
In the second section, a so-called partial wave analysis will be performed, primarily to extract information from the $\pi\pi$ invariant mass spectra. First, the partial wave model will be introduced, which fulfills the conditions of analyticity and unitarity. Then the method will be presented, which was used to fit the model to both data samples simultaneously, by optimizing a select number of model parameters. And in the end of this section, the results of the fit will be discussed.

6.1 Signal Selection

After the initial event selection, which focuses on the extraction of the desired final states, further selection criteria were applied to extract the following signal reactions:

$$\psi(2S) \to (\phi \to K^+K^-)(X \to \pi\pi),$$
$$\psi(2S) \to (\phi \to K^+K^-)\pi\pi.$$

Both reactions contain the ϕ meson decaying into the final state particles K^+K^-, while the $\psi(2S)$ is supposed to either decay directly, or via an intermediate resonance X, into two final state pions, which can either be $\pi^+\pi^-$, or $\pi^0\pi^0$.
The chosen approach uses the conservation of the J^{PC} quantum numbers, and isospin I in the strong interaction, to restrict the possible quantum numbers for the X resonance. For both the ϕ, and the $\psi(2S)$ meson the quantum numbers are well known, leading to the following quantum numbers for X:

$$\begin{array}{lccccc} J^{PC} & 1^{--} & & 1^{--} & & 0^{++}, 2^{++}, \ldots \\ I & 0 & & 0 & & 0 \\ & \psi(2S) & \to & \phi & + & X. \end{array}$$

If this reaction is governed by the strong interaction, then the X resonance has an isospin of zero, positive charge conjugation and parity, and an even total angular momentum. In general, excitations of resonances with higher angular momenta require higher energies, leading to a smaller phase space, and consequently to lower probabilities for the reaction to occur. Therefore, this analysis focuses on isoscalar X resonances with angular momenta equal to zero, or two, assuming that contributions of X resonances with higher angular momenta are negligible. This approach leads to the aforementioned combinations of quantum numbers for possible X states, and was intentionally chosen to study the f_0 and f_2 resonances. Why these resonances are of special interest is motivated in Section 2.4.
Another advantage of this approach is that it leads to a preference of strange quark content in the X state, due to the almost 100% $s\bar{s}$ content of the ϕ meson (cf. Section 2.3). The reason why the quark content of the ϕ meson influences the content of the X state can be seen, when looking at the two lowest orders of Feynman diagrams, for which two examples can be seen in Fig. 6.1. If one assumes that the ϕ meson only has $s\bar{s}$ content, then three gluons participate in the lowest order signal reaction. These gluons can either create the ϕ meson, plus two mesons containing strangeness (cf. Fig. 6.1a), or the ϕ meson plus a pure $s\bar{s}$ state (cf. Fig. 6.1b). At the next order, one more gluon participates in the process, enabling the creation of all light quarks, for the two (cf. Fig. 6.1d), as well as the three-body process (cf. Fig. 6.1c). Each gluon vertex in the Feynman diagram corresponds to a factor of $\sqrt{\alpha_s}$ in the reaction amplitude, and consequently to a factor of α_s in the cross section [72]. Here, $\alpha_s(Q^2)$ is the QCD coupling parameter, which is dependent on the momentum transfer Q. An exact determination of α_s

would go beyond the scope of this work, but for the sake of the argument, the coupling constant can be roughly estimated as $\alpha_s \sim 0.5$ for a momentum transfers of $Q^2 \sim 1\,\text{GeV}$ [73]. This means, when considering the Feynman diagrams, X states with $u\bar{u}$ and $d\bar{d}$ content are suppressed by a factor of $\alpha_s^2 \sim 0.25$. It also follows that reactions, which directly produce two pions, are only possible in second order. The suppression of the two pion state can be directly verified, when comparing the branching fractions $\text{BR}(J/\psi \to \phi\pi\pi) = (1.4 \pm 0.1) \times 10^{-3}$ and $\text{BR}(J/\psi \to \phi KK) = (1.7 \pm 0.1) \times 10^{-3}$ given by the particle data group (PDG) [31, Summary Tables]. One can see that the branching fraction of the two-kaon decay is larger, even though the process has a smaller phase space. This argument can be further supported by exchanging the ϕ meson for a ω meson, and again looking at the branching fractions $\text{BR}(J/\psi \to \omega\pi\pi) = (1.0 \pm 0.1) \times 10^{-2}$ and $\text{BR}(J/\psi \to \omega KK) = (1.9 \pm 0.4) \times 10^{-3}$ [31, Summary Tables]. In this case the branching fraction for the two-pion process is one order of magnitude larger than that of the two-kaon process. Analogous to the processes involving ϕ mesons, this behavior can be explained when looking at the Feynman diagrams. Due to the large $u\bar{u}$ and $d\bar{d}$ content of the ω meson, one would expect a suppression of $s\bar{s}$ states in such processes. This selection of the flavor quantum numbers of the quarks making up the X resonance, in combination with the restrictions on the other quantum numbers mentioned above, provides an opportunity to obtain information about the flavor content of the f_0 and f_2 resonances. Combining the results of this work with the results of similar analyses, which substitute the ϕ meson with an ω meson, or the $\pi\pi$ system with a KK system, could be an important step to finally understand the nature of the f_J resonances.
Now that the definition of the signal process has been presented and motivated, the next steps will show the methods used to select signal events from the data sets of the $K^+K^-\pi\pi$ final states.

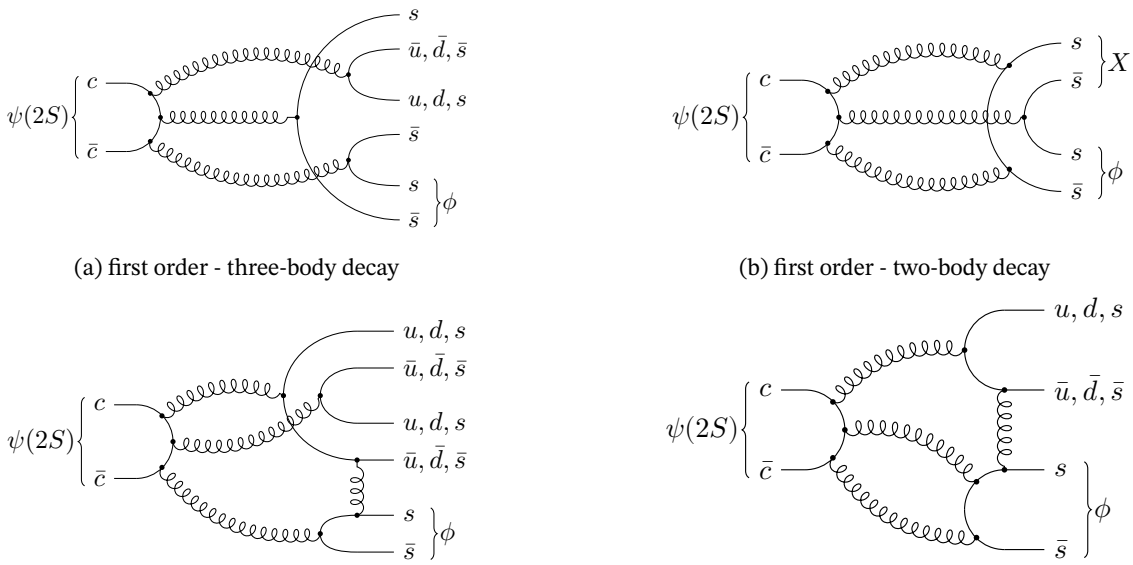

(a) first order - three-body decay

(b) first order - two-body decay

(c) second order - three-body decay

(d) second order - two-body decay

Figure 6.1: A selection of first and second order Feynman diagrams for possible signal processes.

6.1.1 Kinematic Fit Quality

For the first selection criterion, the quality of the kinematic fit, which was introduced in Section 5.4, was investigated. The goodness-of-fit resulting from the minimization of Eq. (A.12), is given by the χ^2_{NC} value, with the NC standing for the number of constraints used for the kinematic fit. It is expected that the χ^2_{NC} distribution of signal events is different, and in average at lower χ^2_{NC} values, than the distribution of background events containing an incorrectly reconstructed final state. To maximize the yield of signal events in respect to the number of data events, while still ending up with a statistically significant amount of events, a figure of merit (FOM) was used. The FOM was defined in dependence of a maximal χ^2_{NC} value χ^2_{max}:

$$\mathrm{FOM}(\chi^2_{\mathrm{max}}) = r \cdot s = S^2/N^{3/2}, \tag{6.1}$$

with $r = S/N$ being the ratio between signal events S and data events N, and $s = S/\sqrt{N}$ being the statistical significance. The number of data events is given by the integration over the χ^2_{NC} distribution of the data sample, while the number of signal events was calculated by integrating over the χ^2_{NC} distribution of the signal Monte-Carlo sample:

$$\mathrm{N}(\chi^2_{\mathrm{max}}) = \int_0^{\chi^2_{\mathrm{max}}} \mathrm{data}(\chi^2_{\mathrm{NC}})\mathrm{d}\chi^2_{\mathrm{NC}} \tag{6.2}$$

$$\mathrm{S}(\chi^2_{\mathrm{max}}) = \int_0^{\chi^2_{\mathrm{max}}} \mathrm{MC}_{\mathrm{sig}}(\chi^2_{\mathrm{NC}})\mathrm{d}\chi^2_{\mathrm{NC}}. \tag{6.3}$$

The rounded χ^2_{max} value, at which the FOM reaches its maximum, was chosen as the maximum χ^2_{NC} value, for which events get accepted. For the $\pi^+\pi^-$ final state the function reached its maximum at $\chi^2_{\mathrm{max}} = 25$, while the maximum for the $\pi^0\pi^0$ final state was found at $\chi^2_{\mathrm{max}} = 12$. The distributions corresponding to this method can be seen in Fig. 6.2.

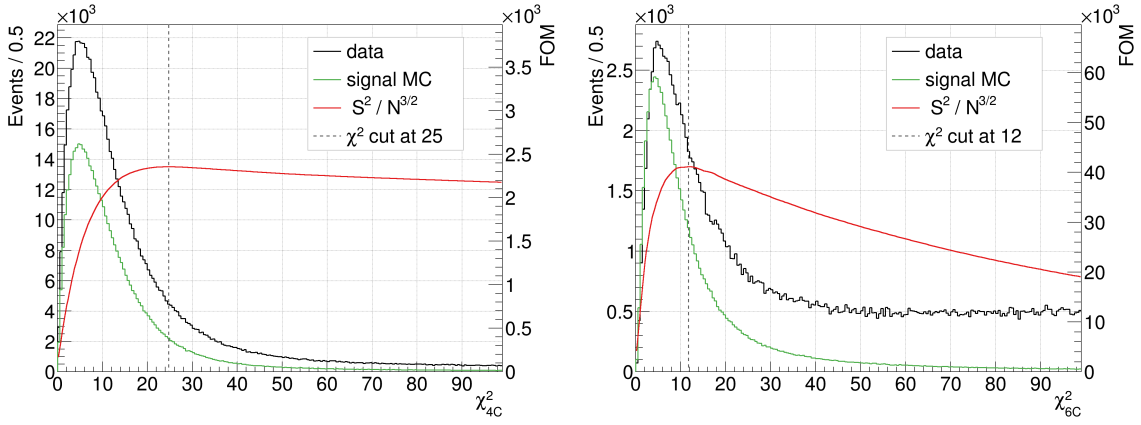

(a) $K^+K^-\pi^+\pi^-$ (b) $K^+K^-\pi^0\pi^0$

Figure 6.2: χ^2_{NC} distributions of the kinematic fit of the data sample (black) and the signal Monte-Carlo sample (green) for both final states. The NC, with N= 4, 6, stands for the number of constraints applied in the kinematic fit. The numeric results of the FOM (cf. Eq. (6.1)) are drawn in red, and their maxima are marked by gray dashed lines. All histograms shown are scaled for clarity.

6.1.2 Signal Region

As the next step of the signal selection, signal regions were determined around the ϕ resonance in the K^+K^- invariant mass spectra for both final states.

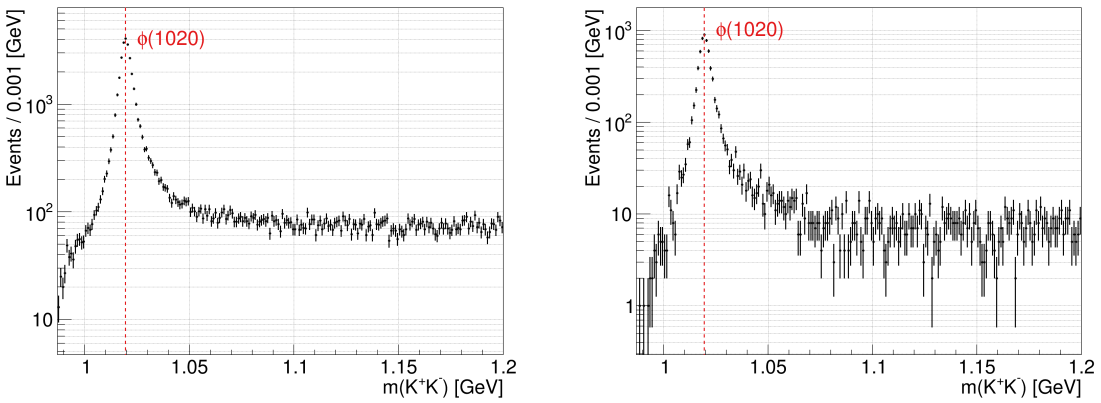

(a) $K^+K^-\pi^+\pi^-$ (b) $K^+K^-\pi^0\pi^0$

Figure 6.3: K^+K^- invariant mass spectra of both final states. The dashed line indicates the mass of the ϕ resonance according to the PDG [31, Summary Tables].

Before discussing the methods used to determine the signal region, it is important to mention that, chronologically, the signal regions were determined first, and then the remaining background reactions were investigated, leading to the veto of events in the vicinity of the $K^*(892)$ resonance. After the veto region was chosen, the determination of the signal region was repeated, benefiting from the lower background level. There is no advantage in presenting the signal selection before and after the veto, but the motivation for implementing the veto becomes clearer after the selection of the signal region. Therefore, the spectra and results shown in the next sections will already use the $K^*(892)$ veto, while the veto itself will be discussed in Section 6.1.3.
In Fig. 6.3, the K^+K^- invariant mass spectra can be seen, showing a clear peak at the mass of the ϕ resonance. Multiple steps were needed to determine an optimized signal region. These steps, as well as the physical properties that could be extracted in the process, will be discussed in the following subsections.

Fit Model

The first step was to define a model with a separate signal and background part, to describe the ϕ resonance in data. Breit-Wigner distributions are suitable for the description of narrow and isolated resonances, which makes them an appropriate choice for the description of the ϕ resonance. Due to the small width of the ϕ resonance of about 4 MeV, the energy resolution of the detector could have an influence on the line shape of the peak, thus the Breit-Wigner was convolved with a Gaussian to account for possible resolution effects.

The signal probability density function (PDF) in dependency of the invariant mass m of the K^+K^- system is defined as:

$$\mathcal{P}_{\text{sig}}(m) = A \cdot N \cdot \int_{-\infty}^{+\infty} |\mathcal{A}_{\text{BW}}(M)|^2 \cdot g(m - M)\,\mathrm{d}M, \tag{6.4}$$

with the signal amplitude A, N being a normalization factor, $\mathcal{A}_{\text{BW}}(m)$ being the Breit-Wigner amplitude and $g(m)$ being the Gaussian PDF with $\mu = 0$ (cf. Eq. (A.5)). When the ϕ meson, with a total angular momentum quantum number of $J = 1$, decays into two pseudoscalar kaons, with $J = 0$, its angular momentum is transferred to a relative orbital angular momentum of $l = 1$ between the two kaons. To account for this angular momentum excitation, the parameterization presented in Eq. (3.86) was chosen with $l = 1$:

$$\mathcal{A}_{\text{BW}}(m) = \frac{\alpha \cdot g \cdot (p/p_0) \cdot B_1(p/p_0)}{M_\phi^2 - m^2 - i \cdot M_\phi \cdot \Gamma}, \tag{6.5}$$

with the mass dependent width

$$\Gamma = \Gamma_\phi \cdot \frac{M_\phi}{m} \cdot \left(\frac{p \cdot B_1(p/p_0)}{p_\phi \cdot B_1(p_\phi/p_0)} \right)^2, \tag{6.6}$$

and the momentum

$$p = \frac{1}{2}\sqrt{m^2 - 4m_K^2}, \tag{6.7}$$

containing the mass of a charged kaon $m_K = 493.677\,\text{MeV}$ [31, Summary Tables]. p_ϕ is the momentum at $m = M_\phi$, while the momentum scale p_0 is arbitrarily chosen to be 0.33 GeV, as this value was already successfully used in Ref. [74]. The Blatt-Weisskopf factor B_1 can be found in Eq. (A.2), and M_ϕ and Γ_ϕ are the Breit-Wigner mass and width of the ϕ resonance. To be able to directly extract the number of ϕ events from the signal PDF, the normalization was chosen as:

$$N = \frac{1}{\iint_{-\infty}^{+\infty} |\mathcal{A}_{\text{BW}}(M)|^2 \cdot g(m - M)\,\mathrm{d}M\mathrm{d}m}. \tag{6.8}$$

The expression in the denominator can be simplified by using Fubini's theorem [75]:

$$\begin{aligned}
\int_{-\infty}^{+\infty} \mathcal{P}_{\text{sig}}(m)\,dm &= \int_{-\infty}^{\infty} (|\mathcal{A}_{\text{BW}}|^2 * g)(m)\,dm && (6.9)\\
&= \left(\int_{-\infty}^{\infty} |\mathcal{A}_{\text{BW}}(m)|^2\,dm \right) \cdot \left(\int_{-\infty}^{\infty} g(m)\,dm \right) && (6.10)\\
&= \int_{-\infty}^{\infty} |\mathcal{A}_{\text{BW}}(m)|^2\,dm. && (6.11)
\end{aligned}$$

The Gaussian PDF is already normalized, so the integration over it becomes one, leaving only the integration of the Breit-Wigner distribution. Using this result, Eq. (6.8) can be written as:

$$N = \frac{1}{\int_{-\infty}^{+\infty} |\mathcal{A}_{\text{BW}}(m)|^2\,\mathrm{d}m}. \tag{6.12}$$

Because no analytical solution exists for this integration, a numeric integration was performed. The limits of the integration were chosen in such a way that increasing the integration interval did not change the significant digits of the resulting value. Since the mass spectrum is binned with a constant bin width h, it is necessary to divide the amplitude A by said width, to obtain the number of observed events:

$$N_{\phi,\text{obs}} = \frac{A}{h}. \tag{6.13}$$

Due to the position of the ϕ resonance close to the two-kaon production threshold, the background sharply rises on the left flank of the resonance and only slightly changes, when reaching higher masses. To describe this special shape, the ARGUS distribution was chosen, as it was specifically defined for the description of continuum background at thresholds for the analyses of data from the ARGUS experiment [76]. The PDF of the ARGUS distribution is defined as follows:

$$\text{ARGUS}(x) = \frac{\chi^3}{\sqrt{2\pi}\Psi(\chi)} \cdot \frac{x}{c^2}\sqrt{1-\frac{x^2}{c^2}} \cdot \exp\left[-\frac{1}{2}\chi^2\left(1-\frac{x^2}{c^2}\right)\right], \tag{6.14}$$

containing the function

$$\Psi(\chi) = G(\chi) - \chi \cdot g(\chi) - \frac{1}{2}, \tag{6.15}$$

with $G(\chi)$ being the cumulative distribution function (CDF) of the Gaussian distribution, and $g(\chi)$ being the PDF of the Gaussian distribution with $\mu = 0$, and $\sigma = 1$ (cf. Eqs. (A.5) and (A.6)). The ARGUS distribution is only defined for values of x between zero and the positive cut-off parameter c, while the positive parameter χ is connected to the curvature of the distribution. In this form, the function is not suitable to describe the background at the ϕ resonance, so the distribution was mirrored, shifted, and a background amplitude B was multiplied. To facilitate the mirroring and shifting, the variable x was redefined as:

$$x \to x'(m) = c - (m - 2m_{KK}), \tag{6.16}$$

resulting in the invariant mass dependent PDF for the background:

$$\mathcal{P}_{\text{bkg}}(m) = B \cdot \frac{\chi^3}{\sqrt{2\pi}\Psi(\chi)} \cdot \frac{x'(m)}{c^2}\sqrt{1-\frac{x'(m)^2}{c^2}} \cdot \exp\left[-\frac{1}{2}\chi^2\left(1-\frac{x'(m)^2}{c^2}\right)\right], \tag{6.17}$$

which is defined for invariant masses between the two-kaon production threshold $2m_{KK}$ and $c + 2m_{KK}$.

The full model can now be constructed as the sum of Eqs. (6.4) and (6.17):

$$f(m;\vec{\theta}) = \mathcal{P}_{\text{sig}}(m;\vec{\theta}_{\text{sig}}) + \mathcal{P}_{\text{bkg}}(m;\vec{\theta}_{\text{bkg}}), \tag{6.18}$$

where $\vec{\theta} = \vec{\theta}_{\text{sig}} + \vec{\theta}_{\text{bkg}}$ is a vector containing all parameters of the model, with $\vec{\theta}_{\text{sig}} = (A, M_\phi, \Gamma_\phi, \sigma)$ being the signal parameters, and $\vec{\theta}_{\text{bkg}} = (B, \chi, c)$ being the background parameters. Now that the model is defined, in the next step, a fit function will be derived to optimize the aforementioned parameters.

Fit Method

To fit the parameters $\vec{\theta}$ to the data, it is necessary to define a fit function, which can be numerically optimized. For the fit on the K^+K^- invariant mass histogram, the negative logarithmic likelihood $-\ln\mathcal{L}$ was minimized. The likelihood function gives the probability that a model, with a given set of parameters $\vec{\theta}$, describes a data sample. For a data set with N bins of equal width h, where the contents of each bin are distributed by a probability function P, the likelihood is defined as:

$$\mathcal{L}(\vec{n}, \vec{f}(\vec{\theta})) = \prod_{i=1}^{N} P(n_i, f_i(\vec{\theta})). \tag{6.19}$$

This function has two variables, the vector $\vec{n}$ with the number of data events for each bin, and the vector $\vec{f}$ with the number of events per bin, predicted by the model. For a given bin i, the number of data events is directly given by the histogram. To get the predicted number of events in a bin i, one has to integrate the model function (Eq. (6.18)) over the interval of the bin:

$$f_i(\vec{\theta}) = \int_{m_0+h(i-1)}^{m_0+h\cdot i} f(m;\vec{\theta})\,\mathrm{d}m, \tag{6.20}$$

with m_0 being the invariant mass at the lower edge of the first bin ($i = 1$). The bin content, being a discrete result of a counting experiment, is expected to follow a Poisson distribution. As such, Eq. (A.10) was used as the probability function P resulting in the following likelihood:

$$\mathcal{L}(\vec{n}, \vec{f}) = \prod_{i=1}^{N} \frac{f_i^{n_i}}{n_i!} \cdot e^{-f_i}. \tag{6.21}$$

As previously stated, the likelihood was not maximized, but the negative logarithmic likelihood minimized to avoid the numerical problem of reaching the float limit. Both methods yield the same results, due to the continuous and monotonic nature of the logarithmic function. Neglecting all constant terms, the negative logarithmic likelihood can be written as:

$$\mathcal{F}(\vec{\theta}) = -\ln\mathcal{L} = -\sum_{i=1}^{N} [n_i \ln(f_i) - f_i] \tag{6.22}$$

This function $\mathcal{F}$ is the fit function, containing the data, and the parameter dependent model.

The next step was to minimize the fit function to get the optimal parameters for the model, from which the distribution of signal and background events could be determined. Bins within an invariant mass interval, starting at two times the charged kaon mass and ending at 1.2 GeV, were used for the fit. For both final states the parameters $\vec{\theta} = (A, M_\phi, \Gamma_\phi, \sigma, B, \chi, c)^T$ were included in the fit. Due to the low background levels in the K^+K^- invariant mass spectrum of the $\pi^0\pi^0$ final state, the fit had trouble converging when using all background parameters for the fit. Thus, the cut-off value c was fixed to the size of the K^+K^- phase space using the masses of the $\psi(2S)$, π^0, and $K^\pm$ mesons from the PDG [31, Summary Tables], resulting in a value of $c \approx 2.43$ GeV. Both the width of the Breit-Wigner, and the standard deviation of the Gaussian contribute to the total width of the peak, leading to a strong correlation between the

two parameters. To improve the performance of the fit for both final states, the Breit-Wigner width of the ϕ resonance was fixed to the well determined PDG value $\Gamma_\phi = (4.24 \pm 0.01)\,\mathrm{MeV}$ [31, Summary Tables], while the unknown detector resolution σ was left as a free fit parameter.

Fit Results

Now the results of the fit on the K^+K^- invariant mass spectra shall be presented and discussed. Plots containing the solutions of the fits for both final states can be seen in Fig. 6.4, while the optimized fit parameters with their corresponding uncertainties can be found in Table 6.1.

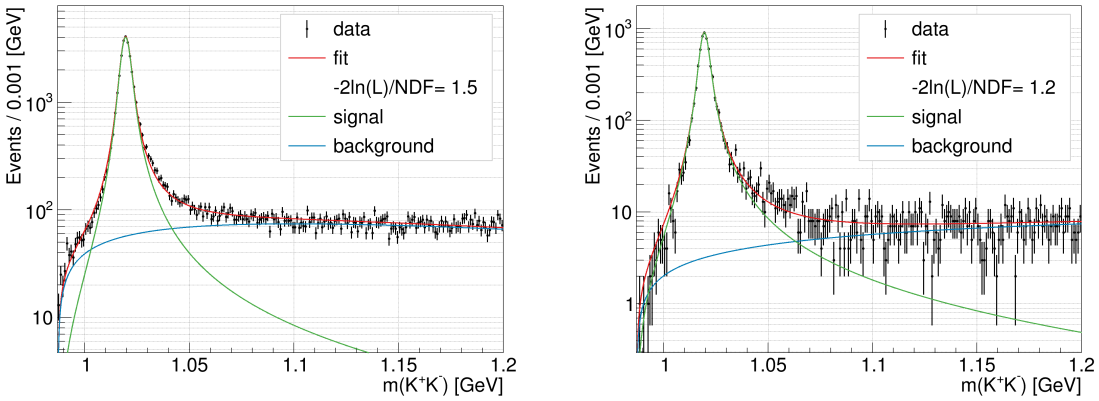

(a) $K^+K^-\pi^+\pi^-$ (b) $K^+K^-\pi^0\pi^0$

Figure 6.4: Fits of Eq. (6.18) onto the K^+K^- invariant mass spectra for both final states. The signal and background part of the fit function are drawn separately, and the goodness-of-fit ($-2\ln(\mathcal{L})/\mathrm{NDF}$) is given for both fits.

In the legends of the plots, the $-2\ln(\mathcal{L})/\mathrm{NDF}$ value can be seen, which is related to the χ^2/NDF value describing the goodness-of-fit for a least-squares fit. For large mean values λ, the Poisson distribution can be approximated by the Gaussian distribution, leading to the likelihood function:

$$\mathcal{L}(\vec{n},\vec{f}) = \prod_{i=1}^{N} e^{-\frac{(n_i-f_i)^2}{2\sigma^2}} = \exp\left(-\sum_{i=1}^{N}\frac{(n_i-f_i)^2}{2\sigma^2}\right) \overset{Eq.\ (A.12)}{=} \exp\left(-\chi^2/2\right). \tag{6.23}$$

Taking $-2\ln\mathcal{L}$ of this function results in the χ^2 function, making the two definitions equivalent for high statistic data samples.

In the following, the fit results shall be discussed. In comparison to the PDG value for the mass of the ϕ meson $m_{\phi,\mathrm{PDG}} = (1.019461 \pm 0.000016)\,\mathrm{GeV}$ [31, Summary Tables], the Breit-Wigner masses resulting from the fits are both shifted towards higher masses not within the uncertainty of the PDG value. This deviation could be caused by the detector calibration. Another possibility is, that the deviation results from the distortion of the resonances line shape, due to its position at the K^+K^- production threshold, and the influence of the angular momentum transfer in the decay. As mentioned in Section 3.2.4, these circumstances lead to

differences between the Breit-Wigner mass, and the physical mass of the particle. Both fits agree with an energy resolution of about 1 MeV, resulting in a relative energy resolution of $\sim 0.1\,\%$ for two charged kaons at the energy of the ϕ resonance.

Table 6.1: Parameter values and uncertainties resulting from the fit of Eq. (6.18) onto the K^+K^- invariant mass histogram for both final states.

Parameter	$K^+K^-\pi^+\pi^-$	$K^+K^-\pi^0\pi^0$
A	32.3 ± 0.2	6.97 ± 0.08
M_ϕ	(1.01981 ± 0.00002) GeV	(1.01979 ± 0.00004) GeV
σ	(1.10 ± 0.03) MeV	(0.91 ± 0.08) MeV
B	36 ± 5	16.1 ± 0.4
χ	2.0 ± 0.7	0 ± 1
c	(1.1 ± 0.6) GeV	-

When looking at the results for the background parameters, one notices that all of them have high relative uncertainties, especially χ for the fit to the $\pi^0\pi^0$ final state. The parameterization of the background was primarily chosen because it describes the behavior at the production threshold and was already proven to be reliable in previous works (cf. Ref. [74, 77]). For the description of the background in this work however, the combination of the highly correlated parameters, and the generally low background level led to very unstable fits, resulting in large uncertainties for the fit parameters. But, assuming that the general shape of the background is well described, these high uncertainties are not expected to impair the results of the following analysis. For subsequent analyses however, other background parameterizations should be tried, e.g. those used in Refs. [78, 79].

With the resulting amplitudes A it is now possible to determine the branching ratios for the processes $\psi(2S) \to \phi\pi^+\pi^-$ and $\psi(2S) \to \phi\pi^0\pi^0$ by using the following equations:

$$\mathrm{BR}(\psi(2S) \to \phi\pi^+\pi^-) = \frac{N_{\phi,\mathrm{obs}}^{(\pi^+\pi^-)}}{\epsilon^{(\pi^+\pi^-)} \cdot \mathrm{BR}(\phi \to K^+K^-) \cdot N_{\psi(2S)}}, \tag{6.24}$$

$$\mathrm{BR}(\psi(2S) \to \phi\pi^0\pi^0) = \frac{N_{\phi,\mathrm{obs}}^{(\pi^0\pi^0)}}{\epsilon^{(\pi^0\pi^0)} \cdot \mathrm{BR}(\phi \to K^+K^-) \cdot \mathrm{BR}(\pi^0 \to \gamma\gamma)^2 \cdot N_{\psi(2S)}}. \tag{6.25}$$

These equations contain the number of observed ϕ events $N_{\phi,\mathrm{obs}}^{(\pi\pi)}$ and the efficiency $\epsilon^{(\pi\pi)}$ of the respective channels, as well as the branching ratios $\mathrm{BR}(\phi \to K^+K^-)$ and $\mathrm{BR}(\pi^0 \to \gamma\gamma)$, and the number of $\psi(2S)$ events $N_{\psi(2S)}$ in the data sample. Using Eq. (6.13), the number of observed ϕ events can directly be calculated with the fit results for the amplitude A.
Due to correlations between fit parameters, it is possible that the likelihood distribution around the fit result is asymmetric, leading to asymmetric uncertainties. These uncertainties are not directly given by the fitting tool; thus, they were determined separately for the $\pi^+\pi^-$ final state. To determine the asymmetric uncertainties, the fit was repeated for 160 different

amplitude values. These amplitude values were chosen equidistant from each other, in an interval of $(A \pm 4 \cdot u(A))$, where $u(A)$ is the symmetric uncertainty resulting from the fit. Relative likelihoods were determined by dividing the likelihoods of the 160 fits by the likelihood of the original fit, where the amplitude was optimized. Then an asymmetric Gaussian (cf. Appendix A.1.5) was used to fit the resulting relative likelihood values, using the least-square minimization method (cf. Appendix A.1.7). The mean μ of the Gaussian was fixed to the number of observed events calculated from the optimized amplitude. Due to the instability of the fit for the $\pi^0\pi^0$ final state, this method did not yield reliable results, and thus the symmetric uncertainties from the fit were used for the determination of the branching ratio. The results for the $\pi^+\pi^-$ final state can be seen in Fig. 6.5. The resulting asymmetry does not influence the significant digit of the uncertainty, and thus the uncertainty of the number of observed events was also assumed to be symmetrical.

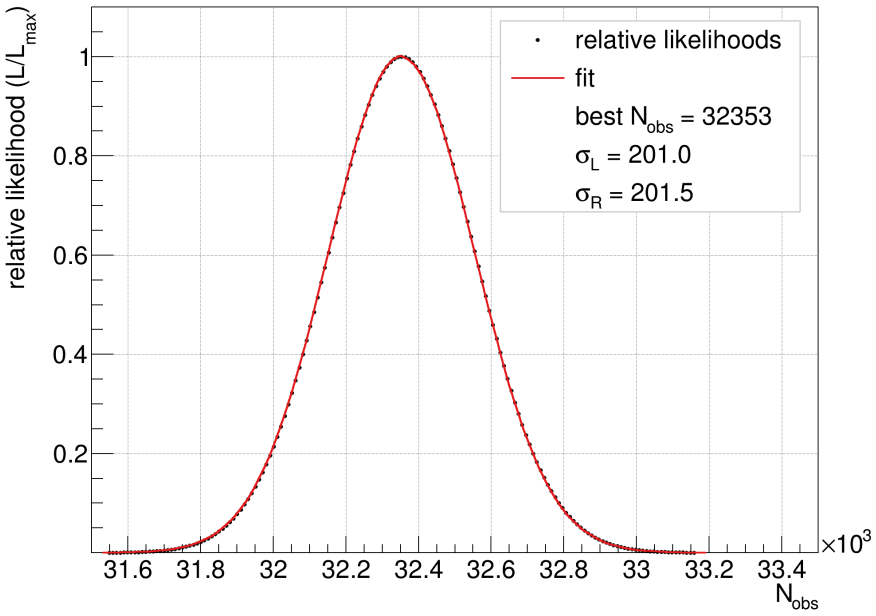

Figure 6.5: Plotted as black points are the relative likelihoods determined by fits on the K^+K^- invariant mass spectrum of the $K^+K^-\pi^+\pi^-$ final state, for different fixed amplitudes. The number of observed events N_{obs} corresponding to the amplitudes are given on the abscissa. The fitted asymmetric Gaussian is shown as a red line, and the fit results for the left and right standard deviations can be seen in the legend. The number of observed events resulting from the optimized amplitude can also be seen in the legend.

The efficiency was calculated by dividing the number of accepted signal Monte-Carlo events $N_{\mathrm{MC,acc}}$ after the selection criteria, by the number of generated signal Monte-Carlo events $N_{\mathrm{MC,gen}}$:

$$\epsilon = \frac{N_{\mathrm{MC,acc}}}{N_{\mathrm{MC,gen}}}. \tag{6.26}$$

The resulting efficiencies are:

$$\epsilon^{(\pi^+\pi^-)} = (23.19 \pm 0.02)\,\%,$$
$$\epsilon^{(\pi^0\pi^0)} = (13.02 \pm 0.01)\,\%.$$

Their uncertainties were determined using uncertainty propagation of the statistical uncertainties of the numbers of accepted Monte-Carlo events. As expected, the efficiency of the $\pi^0\pi^0$ final state is lower than that of the $\pi^+\pi^-$ final state, due to the reconstruction of every π^0 meson from two photons.
The branching ratios for $\phi \to K^+K^-$, and $\pi^0 \to \gamma\gamma$, with their corresponding uncertainties, were taken from the PDG [31, Summary Tables], and the number of $\psi(2S)$ events, and its uncertainty, was taken from Ref. [63]. By inserting all aforementioned values into Eqs. (6.24) and (6.25), and using uncertainty propagation to calculate the statistical uncertainty, shown first, and systematic uncertainty, shown second, the following branching ratios were determined:

$$\mathrm{BR}(\psi(2S) \to \phi\pi^+\pi^-) = (1.252 \pm 0.007 \pm 0.012) \times 10^{-4}$$
$$\mathrm{BR}(\psi(2S) \to \phi\pi^0\pi^0) = (0.492 \pm 0.006 \pm 0.005) \times 10^{-4}$$

All values used, as well as their uncertainties are listed in Table A.5. The branching ratio for $\psi(2S) \to \phi\pi^+\pi^-$ lies within the uncertainties of the PDG value of $(1.18 \pm 0.26) \times 10^{-4}$ [31, Summary Tables], whereas no branching ratio is listed yet in the PDG for the reaction $\psi(2S) \to \phi\pi^0\pi^0$.
From perturbative QCD follows the so called "12% rule", which predicts [80]:

$$\frac{\mathrm{BR}(\psi(2S) \to ggg)}{\mathrm{BR}(J/\psi \to ggg)} = (12.2 \pm 2.4)\%. \tag{6.27}$$

This hypothesis was tested by using the presented results, and the branching ratios for the J/ψ decays, with their corresponding uncertainties from the PDG [31, Summary Tables]. Using Eq. (6.27) and uncertainty propagation, the following values could be determined:

$$\frac{\mathrm{BR}(\psi(2S) \to \phi\pi^+\pi^-)}{\mathrm{BR}(J/\psi \to \phi\pi^+\pi^-)} = \frac{(1.25 \pm 0.01) \times 10^{-4}}{(9.4 \pm 1.5) \times 10^{-4}} = (13 \pm 2)\%$$
$$\frac{\mathrm{BR}(\psi(2S) \to \phi\pi^0\pi^0)}{\mathrm{BR}(J/\psi \to \phi\pi^0\pi^0)} = \frac{(0.492 \pm 0.007) \times 10^{-4}}{(5 \pm 1) \times 10^{-4}} = (10 \pm 2)\%.$$

Both values agree within their uncertainties with the theoretical value, providing further experimental confirmation of the 12% rule.

Due to isospin symmetry, one would expect that the decay into $\pi^+\pi^-$ is two times more likely than that into $\pi^0\pi^0$. This factor can be derived from the Clebsch-Gordan coefficients for the transition of a $|I = 0, I_3 = 0\rangle$ isospin state to the two pion states. The Clebsch-Gordan coefficient for the transition to $\pi^+\pi^-$ reads:

$$\langle 0, 0|1, 1/2; 1, -1/2\rangle + \langle 0, 0|1, -1/2; 1, 1/2\rangle = 2/\sqrt{3},$$

while the coefficient for the transition to $\pi^0\pi^0$ is

$$\langle 0, 0|1, 0; 1, 0\rangle = -1/\sqrt{3}.$$

These coefficients appear in the transition matrix element for the processes, leading to the aforementioned factor of two, if the isospin is conserved (cf. Eq. (6.36)). Between the branching ratios, which were experimentally determined in this work, lies a factor of 2.54 ± 0.04, which does not agree with the previous considerations. The disparity between the experimental result and the theoretical expectation can have multiple reasons, three of which will now be discussed.

One of the reasons could be that part of the detected signal events result from electromagnetic transitions, which do not conserve isospin. For example, electromagnetic processes of the kind $\psi(2S) \to \gamma^* \to$ hadrons, containing a virtual photon γ^* make up $(1.73 \pm 0.14)\,\%$[31, Summary Tables] of all $\psi(2S)$ decays, while the decay into hadrons over three gluons makes up $(10.6 \pm 1.6)\,\%$ of all $\psi(2S)$ decays.

Another reason for the discrepancy could be the method used for the determination of the efficiency. The efficiency was determined using Monte-Carlo samples, which are evenly distributed in phase space, and do not contain intermediate resonances. These approximations can lead to a difference between the efficiency determined with the signal Monte-Carlo sample, and the ”real” efficiency. This deviation can also differ between the final states, which would influence the ratio between the branching ratios.

The third possible reason is, that the uncertainties of the branching ratios are underestimated because they do not incorporate the systematic uncertainties, e.g., resulting from the choice of selection criteria.

Now that the results of the fit were presented, the next section will show how the signal regions were determined.

Determination of the Signal Region

The results of the fit give information about the signal and background distribution in the invariant mass region of the ϕ resonance. With this information it is possible to determine an optimized signal region, using a method analogously to the one presented in Section 6.1.1. Due to the asymmetric line shape of the resonance, the left and right limit of the signal region, m_{L} and m_{R}, were optimized separately using the following definitions for the number of signal, and data events:

$$S_{\mathrm{L}} = \int_{m_{\mathrm{L}}}^{M_\phi} \mathcal{P}_{\mathrm{sig}}(m;\vec{\theta}_{\mathrm{fit}})\,\mathrm{d}m \tag{6.28}$$

$$N_{\mathrm{L}} = \int_{m_{\mathrm{L}}}^{M_\phi} f(m;\vec{\theta}_{\mathrm{fit}})\,\mathrm{d}m \tag{6.29}$$

$$S_{\mathrm{R}} = \int_{M_\phi}^{m_{\mathrm{R}}} \mathcal{P}_{\mathrm{sig}}(m;\vec{\theta}_{\mathrm{fit}})\,\mathrm{d}m \tag{6.30}$$

$$N_{\mathrm{R}} = \int_{M_\phi}^{m_{\mathrm{R}}} f(m;\vec{\theta}_{\mathrm{fit}})\,\mathrm{d}m, \tag{6.31}$$

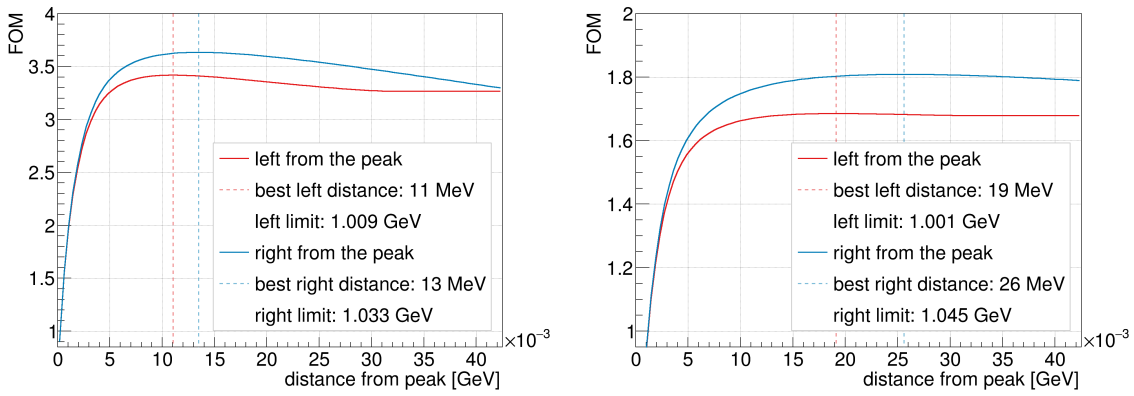

(a) $K^+K^-\pi^+\pi^-$ (b) $K^+K^-\pi^0\pi^0$

Figure 6.6: Results of Eq. (6.1) in dependence of the left distance from the peak (red), and right distance from the peak (blue), for both final states. The maxima of the curves are indicated by the dashed lines, and the distances at which the maxima are located are given in the legend. Also included in the legend are the positions of both limits in the respective K^+K^- invariant mass spectra.

These quantities were determined by integrating over the signal and fit model functions (cf. Eqs. (6.4) and (6.18)), with $\vec{\theta}_{\mathrm{fit}}$ being the optimized parameters. These definitions were inserted into Eq. (6.1), and the invariant mass, at which the FOM reaches its maximum, was determined. The plots showing the FOMs for the different lower and upper mass limits can be seen in Fig. 6.6. The resulting signal regions in the K^+K^- invariant mass spectra can be seen in Fig. 6.7. For both final states the FOMs for the right limit runs into a plateau. This behavior is caused by the kinematic limit in the K^+K^- spectra but does not seem to influence

the results as the peak appears beforehand. Only events within this signal region were used for further analysis.

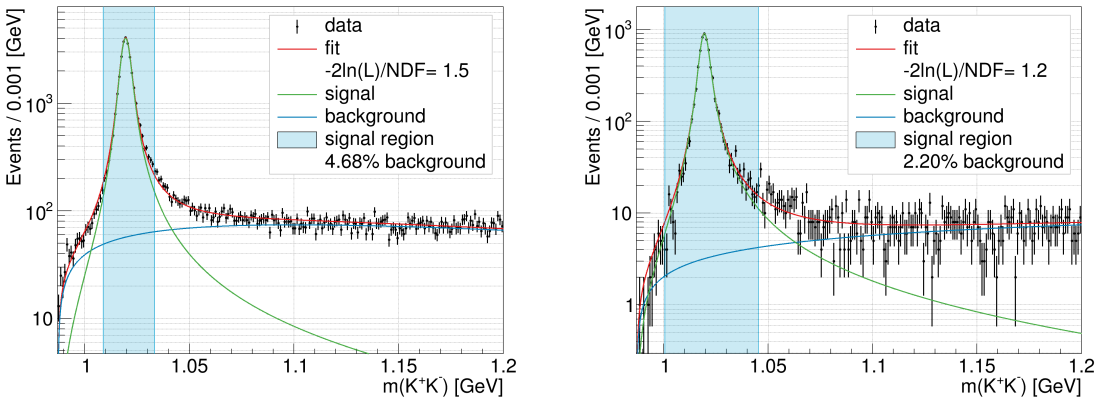

(a) $K^+K^-\pi^+\pi^-$ (b) $K^+K^-\pi^0\pi^0$

Figure 6.7: Shown are the same plots as in Fig. 6.4, but with the inclusion of the optimized signal region. Also, the background percentage, being the number of background events divided by the total number of events in the signal region is given for both final states.

6.1.3 K*(892) Veto

After the selection of the signal region the inclusive Monte-Carlo sample was used to gain insight into possible background reactions. First the reactions in the sample were split into signal reactions, which contain a ϕ resonance and decay into the selected final states, and background reactions, which are all other reactions. Then the background reactions were sorted from the highest number of events to the lowest. The results of this background separation are listed in Appendix A.2.6 and plotted in Fig. 6.8.
It can be seen, that according to the inclusive Monte-Carlo, processes containing the decay $K^*(892) \to K\pi$, contribute significantly to the background of both final states. Therefore, veto regions around the $K^*(892)$ resonance in the $K\pi$ invariant mass spectra were implemented to reduce the number of background events. All events containing a $K\pi$ combination, with an invariant mass within the interval $(m_{K^*,\mathrm{PDG}} - 2 \cdot \Gamma_{K^*,\mathrm{PDG}}) < m(K\pi) < (m_{K^*,\mathrm{PDG}} + 2 \cdot \Gamma_{K^*,\mathrm{PDG}})$, were rejected. For the $\pi^+\pi^-$ final state $m_{K^*,\mathrm{PDG}}$ and $\Gamma_{K^*,\mathrm{PDG}}$ are the mass and width of the $K^{*0}(892)/\bar{K}^{*0}(892)$ mesons, being $M_{K^{*0}} = (895.5 \pm 0.2)$ MeV and $\Gamma_{K^{*0}} = (47 \pm 1)$ MeV [31, Summary Tables], while the mass and width for the $\pi^0\pi^0$ final state corresponds to the $K^{*\pm}(892)$ mesons, being $M_{K^{*\pm}} = (891.6 \pm 0.2)$ MeV and $\Gamma_{K^{*\pm}} = (51.4 \pm 0.8)$ MeV [31, Summary Tables]. The $K\pi$ invariant mass spectra, with a red area indicating the veto interval, can be seen in Fig. 6.9.

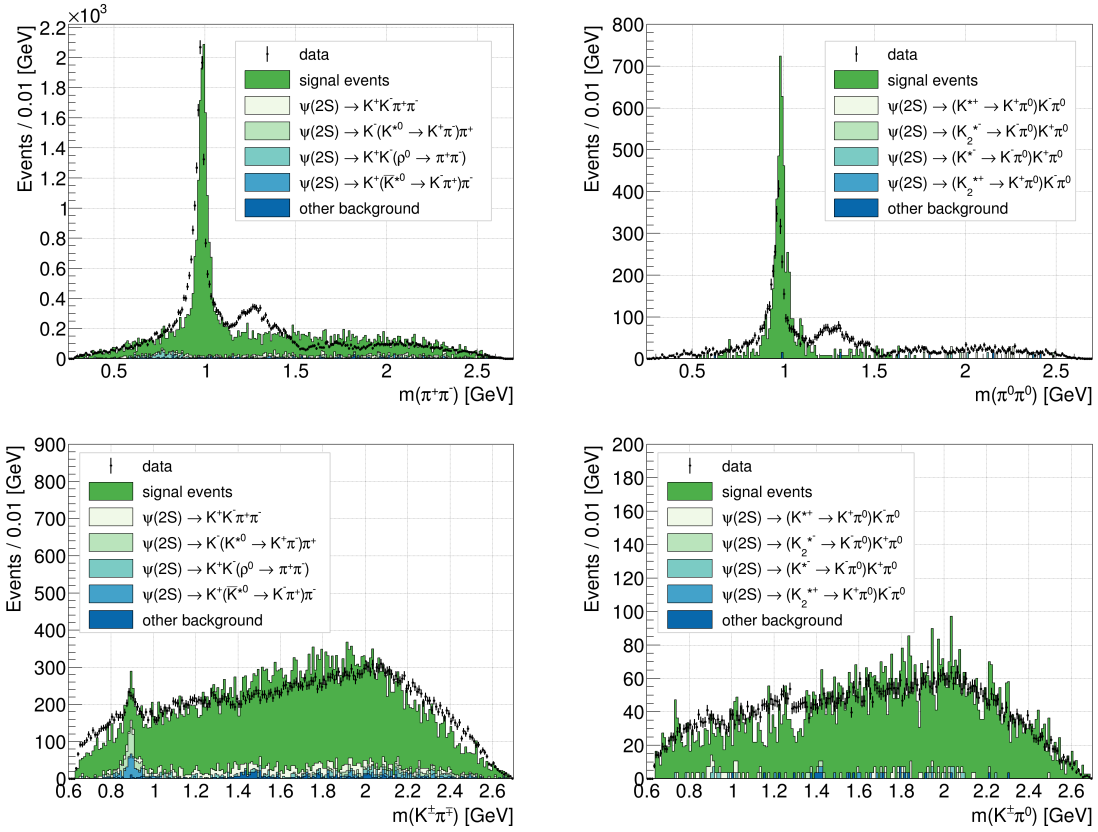

Figure 6.8: $\pi\pi$ (top), and $K\pi$ (bottom) invariant mass spectra of the data samples (black), and the scaled inclusive Monte-Carlo samples (colored) before the $K^*(892)$ veto. Spectra belonging to the $K^+K^-\pi^+\pi^-$ final state are shown on the left, and the ones belonging to the $K^+K^-\pi^0\pi^0$ final state are shown on the right. The events of the inclusive Monte-Carlo are separated into signal events, the four biggest background reactions, and other background.

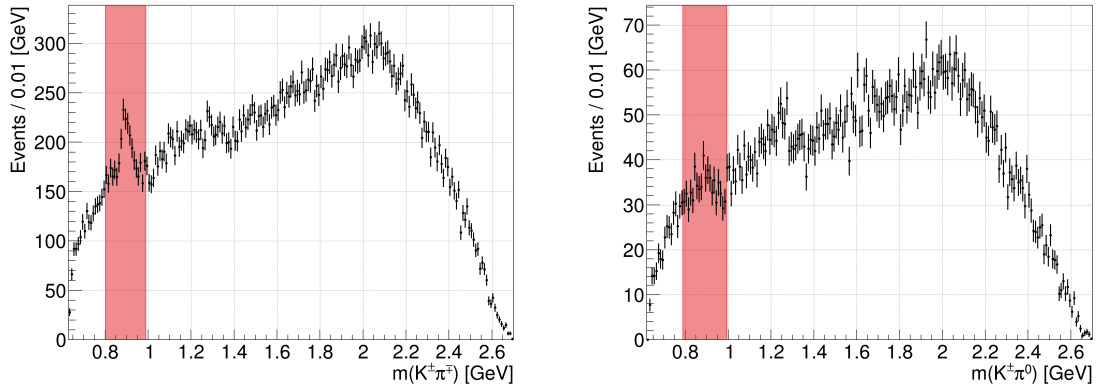

(a) $K^+K^-\pi^+\pi^-$ (b) $K^+K^-\pi^0\pi^0$

Figure 6.9: $K\pi$ invariant mass spectra of both final states. Events with $K\pi$ combinations with invariant masses within the red interval get rejected.

The same spectra shown in Fig. 6.8 can be seen after the veto in Fig. 6.10, while all corresponding signal and background reactions according to the inclusive Monte-Carlo sample are listed in Appendix A.2.6. For the $\pi^+\pi^-$ final state the most significant background reactions remaining are the direct decay into the final state particles, and the reaction $\psi(2S) \to K^+K^-(\rho^0 \to \pi^+\pi^-)$. The direct decay $\psi(2S) \to K^+K^-\pi^+\pi^-$ was integrated into the partial wave analysis, which will be discussed in Section 6.2. No reasonable approach was found to remove the background containing the ρ^0 resonance, as implementing a veto region would remove a significant amount of signal events in the $\pi^+\pi^-$ spectrum, which will be of the focus for the following analysis. An implementation into the partial wave approach was also not possible because the used partial wave model only describes two-body decays. Thus, no further steps were taken regarding the ρ^0 background and possible effects on the results of the partial wave analysis will be discussed at the end of Section 6.2.

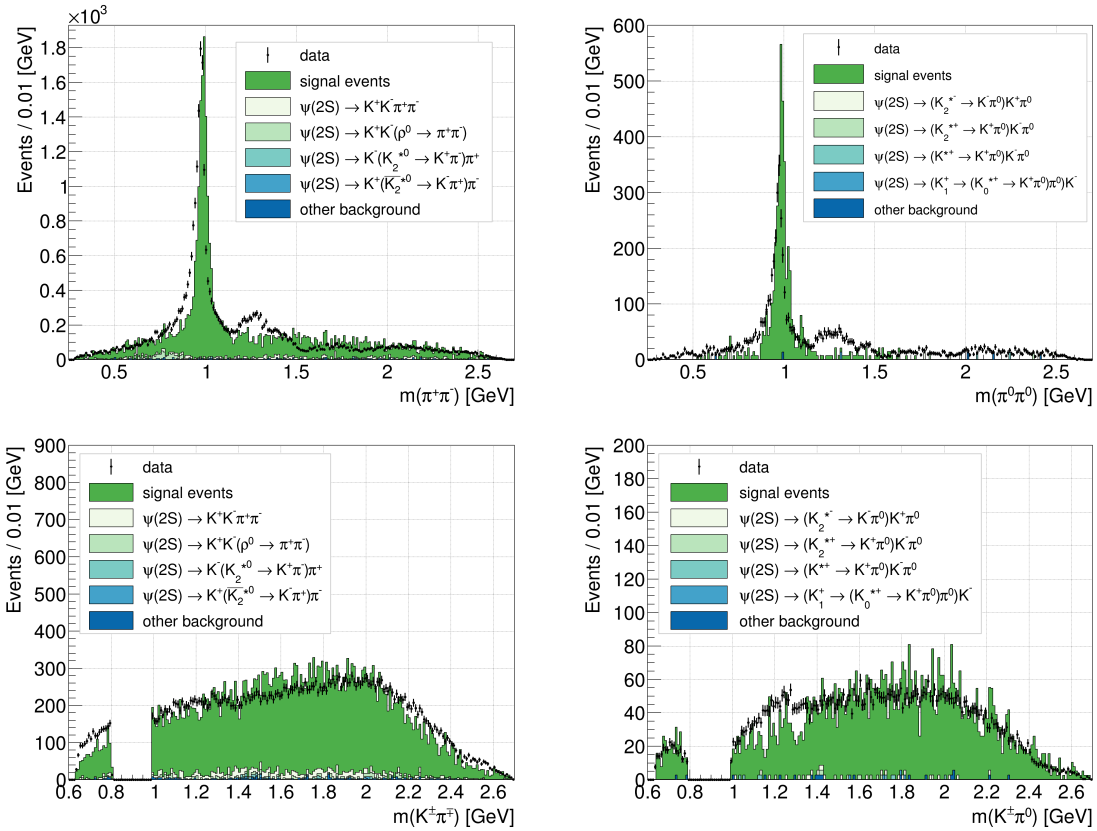

Figure 6.10: $\pi\pi$ (top), and $K\pi$ (bottom) invariant mass spectra from the data samples (black), and the scaled inclusive Monte-Carlo sample (colored) after the $K^*(892)$ veto. Spectra belonging to the $K^+K^-\pi^+\pi^-$ final state are shown on the left, and the ones belonging to the $K^+K^-\pi^0\pi^0$ final state are shown on the right. The events of the inclusive Monte-Carlo are shown separated into signal events, the events of the four biggest background reactions, and other background events.

The largest contribution to the background in the $\pi^0\pi^0$ final state, according to the inclusive Monte-Carlo, are reactions containing excited kaons, other than the $K^{*\pm}(892)$ decaying into

$K\pi$. Due to the disproportionate amount of signal events that would be rejected by implementing other vetoes at the masses of heavier excited kaons, no further selection criteria were used.
This concludes the signal selections. The selected events will be used to perform a partial wave analysis, which will be discussed in detail in the next section.

6.2 Partial Wave Analysis

After the signal selection, the next step of the analysis was to extract information about possible intermediate resonances in the $\pi\pi$ invariant mass spectra. As mentioned in the motivation for the choice of the signal reaction, one would predominantly expect f_0 and f_2 resonances in the $\pi\pi$ spectra. A lot of these resonances are already listed in the Summary Tables of the PDG [31], but their physical properties, like their masses, widths, and branching ratios, are either given with high uncertainties, or not at all. The main reasons for this are their large widths, leading to overlapping line shapes, and their positions at production the thresholds of their decay channels. These properties distort the line shapes of the resonances, making Breit-Wigner fits to the spectra of their daughter particles unreliable. For reference, the production thresholds, and the f_0 and f_2 resonances of interest, are shown in Fig. 6.11. Thus, to extract the properties of these resonances, a fully analytical approach had to be found, which incorporates interference effects, while conserving probability. The next sections will present a model which fulfills these requirements, then introduce the method used to fit the model to the data samples, and finally discuss the results of the fit. As the model relies strongly on the decomposition of the reaction into its partial waves, the kind of method is often called partial wave analysis, or PWA for short.

6.2.1 Model

As the first part of the partial wave analysis, a model had to be defined, describing the data after the signal selection, while fulfilling the requirements mentioned in the introduction of this section. After looking at the list of the remaining reactions according to the inclusive Monte-Carlos samples, and looking for other possible resonances in the spectra, it was concluded, that the vast majority of initial state $\psi(2S)$ transitions into the $K^+K^-\pi\pi$ final states happen over subsequent two-body decays. For the description of such processes the isobar model is used [81]. Two seen processes, which deviate from the isobar model, and appear often enough to justify treatment would be the three-body decay $\psi(2S) \to (\phi \to K^+K^-)\pi\pi$, and four body decay $\psi(2S) \to K^+K^-\pi\pi$. To effectively include the three-body decay into the model, a parameterization was chosen that treats the two pions as single two-pion states, which transition by non-resonant scattering into the two final state pions.

This parameterization will be shown in detail when the dynamics of the decay will be discussed. The four-body decay itself is not parameterized, but is considered by the model through the inclusion of phase space Monte-Carlo samples. How Monte-Carlo samples can be incorporated will be shown in Section 6.2.2.

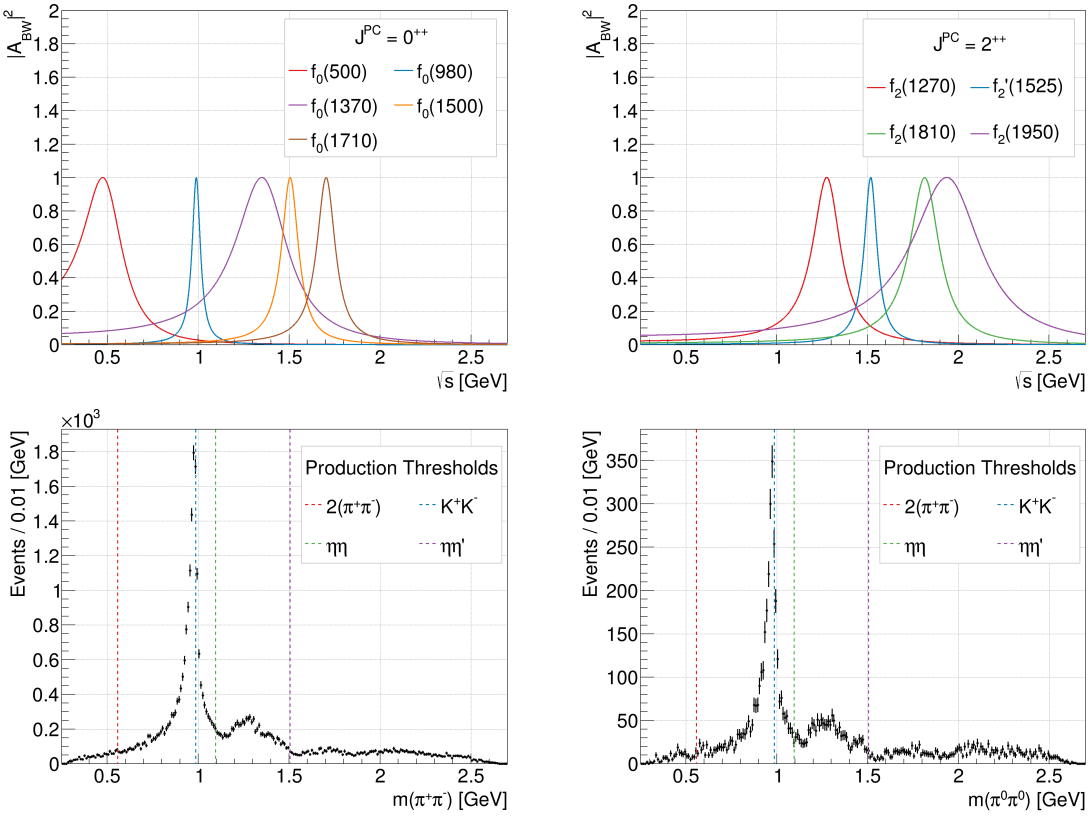

Figure 6.11: In the upper part of the figure, the different f_0 and f_2 resonances, which were considered in the analysis, are plotted as Breit-Wigner resonances (cf. Eq. (A.1)), with their masses and widths taken from the PDG [31, Summary Tables]. In the lower part of the figure, the $\pi\pi$ invariant mass spectra after the signal selection are shown, with lines indicating different production thresholds for possible decay channels of the f_J resonances.

For one of the possible decay chains for the transition between the initial and final states, the reaction amplitude can be written as the product of the production amplitudes of each decay. In the case of the process $\psi(2S) \to (\phi \to K^+K^-)(f_0(500) \to \pi\pi)$ the reaction amplitude is defined as:

$$\mathcal{A}^{(\text{reac})}_{\psi(2S)\to(\phi\to K^+K^-)(f_0(500)\to\pi\pi)} = \mathcal{A}^{(\text{prod})}_{\psi(2S)\to\phi f_0(500)} \cdot \mathcal{A}^{(\text{prod})}_{\phi\to K^+K^-} \cdot \mathcal{A}^{(\text{prod})}_{f_0(500)\to\pi\pi}. \tag{6.32}$$

Then, the total reaction amplitude can be written as the sum over all considered reaction amplitudes.

When only considering different intermediate resonances X, while assuming that the two kaons always result from the decay of a ϕ resonance, the total reaction amplitude can be expressed as follows:

$$\mathcal{A}^{(\mathrm{tot})}_{\psi(2S)\to K^+K^-\pi\pi} = \sum_X \mathcal{A}^{(\mathrm{reac})}_{\psi(2S)\to(\phi\to K^+K^-)(X\to\pi\pi)}. \tag{6.33}$$

As the next step, the production amplitudes will be parameterized. Generally, the Lorentz invariant production amplitude is dependent on the Mandelstam variables s, and t (cf. Section 3.2.1). In this work, the angular dependent part of the amplitude was parameterized using the helicity framework, which was introduced in Section 3.2.5. Using Eq. (3.106), the production amplitude for an arbitrary two-body decay can be written as:

$$\mathcal{A}^{(\mathrm{prod})}_{S_1,S_2,\lambda_1,\lambda_2,J,\tilde{\lambda}}(\theta,\varphi,s) = \mathcal{A}^{(\mathrm{ang})}_{S_1,S_2,\lambda_1,\lambda_2,J,\tilde{\lambda}}(\theta,\varphi)\cdot\mathcal{A}^{(\mathrm{dyn})}(s) \tag{6.34}$$

$$\begin{aligned} &= \sum_{L,S}\sqrt{\frac{2L+1}{4\pi}}\cdot D^{J*}_{\tilde{\lambda},\lambda}(\varphi,\theta,-\varphi)\cdot\langle L,0;S,\lambda|J,\lambda\rangle \\ &\quad\cdot\langle S_1,\lambda_1;S_2,-\lambda_2|S,\lambda\rangle\cdot A_{L,S}\cdot\mathcal{A}^{(\mathrm{dyn})}(s), \end{aligned} \tag{6.35}$$

with $\mathcal{A}^{(\mathrm{ang})}_{S_1,S_2,\lambda_1,\lambda_2,J,M}(\theta,\varphi)$ being the angular part, which is dependent on the helicity angles θ and φ (cf. Fig. 3.4), and $\mathcal{A}^{(\mathrm{dyn})}(s)$ being the dynamical part of the amplitude. J and $\tilde{\lambda}$ are the total angular momentum and corresponding helicity quantum numbers of the mother particle, while S_1, S_2, and λ_1, λ_2 are the spin and helicity quantum numbers of its daughter particles, with $\lambda = \lambda_2 - \lambda_1$. The sum in the amplitude runs over all possible combinations of orbital momentum L and spin S quantum numbers for the decay process. For a specific pair of L and S quantum numbers, the strength and phase of a decay is given by the constant complex canonical amplitude $A_{L,S}$.

Equation (6.35) can now be inserted into Eq. (6.33), using the known quantum numbers of the different initial and final states, and summing over all unknown quantum numbers of the entire process. Thus, the total reaction amplitude for the reactions $\psi(2S)\to K^+K^-\pi\pi$ can be written as:

$$\begin{aligned} \mathcal{A}^{(\mathrm{tot})} = &\sum_X\sum_{I_3}\sum_{\lambda_{\psi(2S)}}\sum_{\lambda_\phi}\sum_{\lambda_X}\sum_L\sum_S\sqrt{\frac{2L+1}{4\pi}}\cdot D^{1*}_{\lambda_{\psi(2S)},\lambda_X-\lambda_\phi}(\varphi_X,\theta_X,-\varphi_X) \\ &\cdot\langle L,0;S,\lambda_X-\lambda_\phi|1,\lambda_X-\lambda_\phi\rangle\cdot\langle J_X,\lambda_X;1,-\lambda_\phi|S,\lambda_X-\lambda_\phi\rangle \\ &\cdot A^{(\psi(2S)\to X\phi)}_{L,S}\cdot\mathcal{A}^{(\mathrm{dyn})}_{\psi(2S)\to X\phi}(s)\cdot\langle 1,I_3^{(\pi_1)};1,I_3^{(\pi_2)}|0,0\rangle\cdot\sqrt{\frac{2J_X+1}{4\pi}} \\ &\cdot D^{J_X*}_{\lambda_X,0}(\varphi_\pi,\theta_\pi,-\varphi_\pi)\cdot\langle J_X,0;0,0|J_X,0\rangle\cdot A^{(X\to\pi\pi)}_{J_X,0,L,S}\cdot\mathcal{A}^{(\mathrm{dyn})}_{X\to\pi\pi}(m^2_{\pi\pi}) \\ &\cdot\sqrt{\frac{3}{4\pi}}\cdot D^{1*}_{\lambda_\phi,0}(\varphi_K,\theta_K,-\varphi_K)\cdot A^{(\phi\to K^+K^-)}_{1,0}\cdot\mathcal{A}^{(\mathrm{dyn})}_{\phi\to K^+K^-}(m^2_{K^+K^-}) \end{aligned} \tag{6.36}$$

The indices of each quantum number and angle indicate the particle they belong to. In general, the dynamical parts can also depend on the given quantum numbers, but the dependencies will only be shown in the concrete definitions. All possible quantum numbers, for each

part of the reaction can be seen in Fig. 6.12, and the angles corresponding to different helicity frames are depicted in Fig. 6.13. Depending on the final state, the sum over the third isospin components of the $\pi_1\pi_2$ state can either include the two possible combinations $I_3^{(\pi_1)} = \pm 1$ and $I_3^{(\pi_2)} = \mp 1$ for the $\pi^+\pi^-$ final state, or the single combination $I_3^{(\pi_1)} = 0$ and $I_3^{(\pi_2)} = 0$ for the $\pi^0\pi^0$ final state.

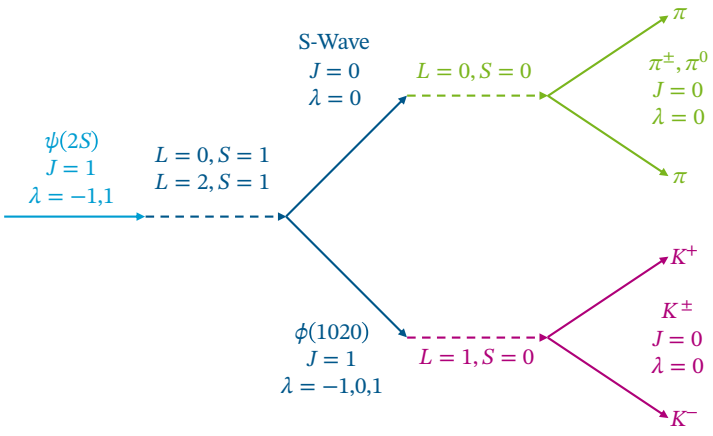

Figure 6.12: All quantum numbers needed for the construction of the total reaction amplitude (cf. Eq. (6.36)). The transition between the $\psi(2S)$ meson and the $\pi\pi$ final state was either described by a state with a total orbital momentum of $J = 0$ (S-wave) (a), or with a total angular momentum of $J = 2$ (D-wave) (b).

The last thing missing for the full parameterization of the total decay amplitude are the definitions of the dynamical amplitudes. For the description of the dynamical part of the $\psi(2S) \to \phi X$ decay, Blatt-Weisskopf factors were used:

$$\mathcal{A}^{(\mathrm{dyn})}_{\psi(2S)\to X\phi}(s) = B_L(p_{\psi(2S)}/p_0), \tag{6.37}$$

with L being the orbital angular momentum quantum number of the decay $\psi(2S) \to \phi X$ and $p_{\psi(2S)}$ being the absolute momentum of the $\psi(2S)$ meson, which results from the 22 mrad

angle between the electron and positron beams. The momentum of the $\psi(2S)$ meson in the laboratory frame is included in the data sample provided by the BESIII collaboration.

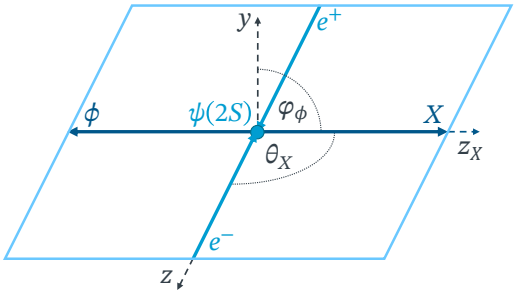

(a) Helicity frame of the decay $\psi(2S) \to \phi X$.

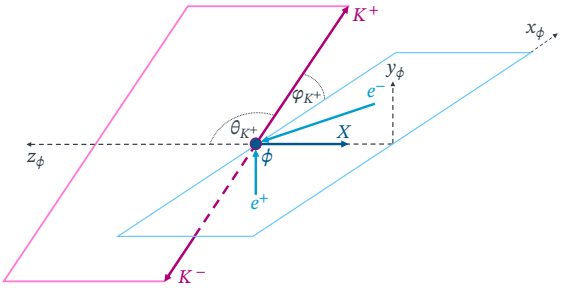

(b) Helicity from of the decay $\phi \to K^+K^-$.

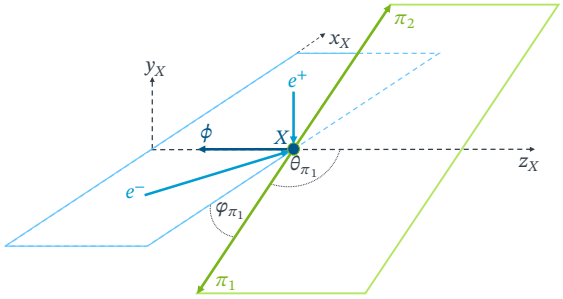

(c) Helicity frame of the decay $X \to \pi_1\pi_2$.

Figure 6.13: Helicity frames, with the corresponding helicity angles θ and φ of the three decays included in Eq. (6.36). The basis vectors for the helicity frame of the decay $\psi(2S) \to X\phi$ in (a) are chosen as follows: x is in horizontal direction in the laboratory frame; y is in vertical direction in the laboratory frame; z is in direction of the symmetry axis of the detector. The light blue border indicates the decay plain spanned by the momentum vectors of e^+ and X and can be seen in all three pictures. In (b) the helicity frame of $\phi \to K^+K^-$ is shown, where the z axis is defined to be in the direction of the ϕ meson in the helicity frame shown in (a). Analogously the z axis of the helicity frame of $X \to \pi_1\pi_2$ illustrated in (c), is defined in the direction of the X state in the helicity frame of (a). $\pi_1\pi_2$ can either be $\pi^+\pi^-$, or $\pi^0\pi^0$ dependent on the current final state. The y axis of both helicity frames in (b) and (c) is chosen to be perpendicular to the light blue decay plane.

For the parameterization of the dynamics of $\phi \to K^+K^-$, a Breit-Wigner distribution was chosen:

$$\mathcal{A}^{(\mathrm{dyn})}_{\phi\to K^+K^-}(m^2_{K^+K^-}) = \frac{m_\phi \cdot \Gamma_\phi}{m^2_\phi - m^2_{K^+K^-} - i \cdot m_\phi \cdot \Gamma(m_{K^+K^-})} \cdot \frac{B_1(p/p_0)}{B_1(p_\phi/p_0)}, \tag{6.38}$$

with $\Gamma(m_{K^+K^-})$ being defined in Eq. (6.6). In contrast to the approach taken in Section 6.1.2, the detector resolution was not considered in this definition, due to restrictions of the PAWIAN software. Possible consequences will be discussed in Section 6.2.3
. The main challenge was to parameterize the dynamics of $X \to \pi\pi$. As the first step, the state X is split into its S-wave contributions, with a total angular momentum of $J = 0$, and its D-Wave contributions, with $J = 2$. Contributions of higher total angular momentum excitations are neglected, as they are expected to be small. Thus, following from the quantum numbers,

resonances in the S-wave can only be f_0 states, while resonances in the D-wave are f_2 states. For the parameterization of the S- and D-wave, Eq. (3.95) was used.
Therefore, the dynamical part of the amplitude for the S-wave is defined as:

$$\mathcal{A}^{(\text{dyn})}_{\text{S-wave}\to\pi\pi}(m^2_{\pi\pi}) = \sum_c \left[\mathbb{1} + \Sigma^{(\text{S-wave})} \cdot K^{(\text{S-wave})}\right]^{-1}_{\pi\pi,c} \cdot P_c^{(\text{S-wave})}, \tag{6.39}$$

with the sum going over the two-body decay channels $\pi\pi$, $K\bar{K}$, $\eta\eta$, and $\eta\eta'$, as well as the 4π channel, which is treated as an effective two-body channel of two particles with two-times the pion mass. By incorporating these five channels, both the Chew-Mandelstam matrix, and the K-matrix become 5×5 matrices. For the different channels, the PDG masses were used for the calculation of the Chew-Mandelstam functions [31, Summary Tables]. For the $\pi\pi$ system, the mass of the charged pion was used, and for $K\bar{K}$ system, the mass of the charged kaon was used.
Equation (3.90), multiplied by the so-called Adler zero term was used for the parameterization of the K-matrix:

$$K^{(\text{S-wave})}_{ba}(m^2_{\pi\pi}) = f_{\text{A0}}(m^2_{\pi\pi}) \cdot \left(\sum_{f_0} \frac{g_b^{(f_0)} g_a^{(f_0)}}{m^2_{f_0} - m^2_{\pi\pi}} + b_{ba}\right), \tag{6.40}$$

$$f_{\text{A0}}(m^2_{\pi\pi}) = \frac{m^2_{\pi\pi} - s_0}{s_{\text{norm}}}. \tag{6.41}$$

In the unphysical region of the amplitude describing the S-wave, the Adler zero term is needed to describe chiral symmetry breaking [82, 83]. Using results from chiral perturbation theory, s_0 was set to $m^2_{\pi^0}/2$ [84], with m_{π^0} being the mass of the π^0 meson from the PDG [31, Summary Tables]. The sum in the resonant part of the amplitude runs over the resonances $f_0(500)$, $f_0(980)$, $f_0(1370)$, $f_0(1500)$ and $f_0(1710)$, while the non-resonant part is parameterized by the non-resonant coupling constants b_{ba}.
Equation (3.92) was chosen for the parameterization of the five elements of the P-vector:

$$P_c^{(\text{S-wave})}(m^2_{\pi\pi}) = \sum_{f_0} \frac{\alpha_{L,S}^{(f_0)} g_c^{(f_0)}}{m^2_{f_0} - m^2_{\pi\pi}} + \tilde{b}_c^{(0)} + \tilde{b}_c^{(1)} m^2_{\pi\pi} + \tilde{b}_c^{(2)} m^4_{\pi\pi}. \tag{6.42}$$

Analogously to the K-matrix, the sum over the resonant part runs over the aforementioned f_0 resonances, but the non-resonant part now includes terms up to second order in $m^2_{\pi\pi}$. The parameters $\alpha_{L,S}^{(f_0)}$ give the coupling strengths to the production process, and are therefore dependent on the quantum numbers L and S of the production process.
The parameterization for the dynamical part of the D-wave was chosen very similar to the one for the S-wave, but due to excitation of the orbital angular momentum in the process, the diagonal n-matrix must be considered in the equation:

$$\mathcal{A}^{(\text{dyn})}_{\text{D-wave}\to\pi\pi}(m^2_{\pi\pi}) = \sum_{c,c'} n_{\pi\pi,c'} \left[\mathbb{1} + \Sigma^{(\text{D-wave})} \cdot K^{(\text{D-wave})} \cdot n^2\right]^{-1}_{c',c} \cdot P_c^{(\text{D-wave})}. \tag{6.43}$$

The diagonal elements of the n-matrix are defined as Eq. (3.89) with $l = 2$. Both sums with the indices c and c' run over the decay channels $\pi\pi$, 4π, $K\bar{K}$, and $\eta\eta$, following the assumption

made in Ref. [85], that the contributions of the $\eta\eta'$ channel are negligible. The K-matrix and P-vector are defined as follows:

$$K_{ba}^{(\text{D-wave})}(m_{\pi\pi}^2) = \sum_{f_2} \frac{g_b^{(f_2)} g_a^{(f_2)}}{m_{f_2}^2 - m_{\pi\pi}^2} + b'_{ba}, \tag{6.44}$$

$$P_c^{(\text{D-wave})}(m_{\pi\pi}^2) = \sum_{f_2} \frac{\alpha_{L,S}^{(f_2)} g_c^{(f_2)}}{m_{f_2}^2 - m_{\pi\pi}^2} + \tilde{b}'_c. \tag{6.45}$$

In both the K-matrix, and the P-vector the sum in the resonant part runs over the resonances $f_2(1270)$, $f_2'(1525)$, $f_2(1810)$, and $f_2(1950)$, while the non-resonant parts are described by a constant term, respectively.
With this the model is fully parameterized and can be optimized for the given data sets. The method used for the optimization will be discussed in the following section.

6.2.2 Fitting Method

An extended likelihood fit was performed to optimize the parameters of the total reaction amplitude (cf. Eq. (6.36)). The not-extended version of the likelihood was defined in Eq. (6.19). If the number of events N is a random variable distributed by a probability density function $f(N, \vec{\theta})$, then the extended likelihood, is defined as:

$$\mathcal{L}_{\text{ext}}(\vec{\theta}) = f(N, \vec{\theta}) \prod_{i=1}^{N} P(\vec{x}_i, \vec{\theta}), \tag{6.46}$$

with $\vec{x}_i$ being a vector of random variables corresponding to the i'th event in the data sample, and $\vec{\theta}$ being a vector of parameters. For this work, the number of data events can be assumed to be large enough, that a Gaussian distribution can be used for $f(N, \vec{\theta})$. The resulting extended likelihood is defined as:

$$\mathcal{L}_{\text{ext}}(\vec{\theta}) = \frac{N_{\text{dat}}!}{\sqrt{2\pi N_{\text{dat}}}} \exp\left(-\frac{(N_{\text{mod}}(\vec{\theta}) - N_{\text{dat}})^2}{2N_{\text{data}}} \right) \prod_{i=1}^{N_{\text{dat}}} P(\vec{x}_i, \vec{\theta}). \tag{6.47}$$

The model does not describe an ordered set of data events, thus a factor of $N_{\text{dat}}!$ had to be added, to account for all possible permutations. For the variance and mean of the Gaussian, the number of data events N_{dat} was taken, while $N_{\text{mod}}(\vec{\theta})$ is the number of events predicted by the model, which depends on the model parameters $\vec{\theta}$. To get this number, the intensity $I(\vec{x}, \vec{\theta})$ of the model has to be corrected by the efficiency $\epsilon(\vec{x})$, and the resulting function must be integrated over the whole phase space of $\vec{x}$:

$$N_{\text{mod}}(\vec{\theta}) = \int I(\vec{x}, \vec{\theta}) \cdot \epsilon(\vec{x}) \, \mathrm{d}x = \int |\mathcal{A}^{(\text{tot})}(\vec{x}, \vec{\theta})|^2 \cdot \epsilon(\vec{x}) \, \mathrm{d}x. \tag{6.48}$$

For the partial wave analysis, the intensity of the model is the absolute square of the total reaction amplitude. It depends on the four four-momenta of the final state particles, contained

in $\vec{x}$, and all model parameters $\vec{\theta}$, like the bare masses, coupling strengths. For a given set of data four-momenta $\vec{x}_i$ the probability density function is defined as:

$$P(\vec{x}_i, \vec{\theta}) = \frac{I(\vec{x}_i, \vec{\theta}) \cdot \epsilon(\vec{x}_i)}{\int I(\vec{x}, \vec{\theta}) \cdot \epsilon(\vec{x}) \, \mathrm{d}x}. \tag{6.49}$$

Generally, the efficiency function $\epsilon(\vec{x})$ is unknown. To avoid this problem, one approximates the integral in Eq. (6.48) by using Monte-Carlo simulations, which include all efficiency effects:

$$\int I(\vec{x}, \vec{\theta}) \cdot \epsilon(\vec{x}) \, \mathrm{d}x \approx \frac{1}{N_{\mathrm{MC}}} \cdot \sum_{j=1}^{N_{\mathrm{MC}}} I(\vec{y}_j, \vec{\theta}), \tag{6.50}$$

with N_{MC} being the number of Monte-Carlo events, after the same selection criteria were applied, as for the data sample, and $\vec{y}_j$ being the j'th set of four-momenta of the Monte-Carlo sample. Hence, by inserting Eqs. (6.48) to (6.50) into Eq. (6.47), one gets:

$$\begin{aligned} \mathcal{L}_{\mathrm{ext}}(\vec{\theta}) = & \frac{N_{\mathrm{dat}}!}{\sqrt{2\pi N_{\mathrm{dat}}}} \exp\left[-\frac{1}{2N_{\mathrm{dat}}} \cdot \left(\frac{1}{N_{\mathrm{MC}}} \sum_{j=1}^{N_{\mathrm{MC}}} I(\vec{y}_j, \vec{\theta}) - N_{\mathrm{dat}} \right)^2 \right] \\ & \cdot \prod_{i=1}^{N_{\mathrm{dat}}} \frac{I(\vec{x}_i, \vec{\theta}) \cdot \epsilon(\vec{x}_i)}{\frac{1}{N_{\mathrm{MC}}} \cdot \sum_{j=1}^{N_{\mathrm{MC}}} I(\vec{y}_j, \vec{\theta})}. \end{aligned} \tag{6.51}$$

The values resulting from this equation are often very small, which can lead to numerical problems during the optimization. To circumvent such problems, it is common to minimize the negative logarithmic likelihood, instead of maximizing the likelihood itself. The function that was minimized to optimize the parameters can be written as follows:

$$\begin{aligned} -\ln \mathcal{L}_{\mathrm{ext}}(\vec{\theta}) = & \frac{1}{2N_{\mathrm{dat}}} \cdot \left(\frac{1}{N_{\mathrm{MC}}} \sum_{j=1}^{N_{\mathrm{MC}}} I(\vec{y}_i, \vec{\theta}) - N_{\mathrm{dat}} \right)^2 - \sum_{i=1}^{N_{\mathrm{dat}}} \ln\left[I(\vec{x}_i, \vec{\theta}) \right] \\ & + \ln\left[\sum_{j=1}^{N_{\mathrm{MC}}} I(\vec{y}_i, \vec{\theta}) \right] + \text{const.} \end{aligned} \tag{6.52}$$

All parts of the sum that do not depend on the parameters $\vec{\theta}$ are included in the "const." term because they are irrelevant for the minimization.

Now the choice of the fit parameters will be discussed. Generally, in all parts of the total reaction amplitude, which depend on a non-zero orbital angular momentum between the daughter particles, the momentum scale factor p_0 is present. There exist no precise theoretical predictions for this factor, but according to [31, review chap. 50], it should lie in a range between 0.2 GeV and 1 GeV. Changing this parameter has a negligible impact on the fit, consequentially destabilizing it, if left as a free fit parameter. Thus, it was set to 0.33 GeV, which has already been proven to be a functioning value in Ref. [74].
The description of the $X \to \pi\pi$ dynamics was done using the K-matrix formalism, which includes multiple channels. All parameters used in the K-matrix impact the behavior of the reaction amplitude for all other channels, consequently, the optimization of these parameters

is not reasonable, when only regarding one channel. Therefore, the parameters s_{norm}, $g_c^{(f_0)}$, $g_c^{(f_2)}$, m_{f_0}, m_{f_2}, b_{ba}, and b'_{ba} were taken from the analysis performed in Refs. [85, 86]. The authors of these papers used a similar model, but did a combined fit on the channels $\pi^0\pi^0$, $\eta\eta$, and K^+K^- using $p\bar{p}$ annihilation data, and $\pi\pi$ scattering data. The parameters resulting from their analysis, and which were used in this work can be found in the supplementary material of Ref. [85].

Only the mass and width of the Breit-Wigner distribution are needed for the parameterization of the ϕ resonance. Given that the description of the ϕ resonance was not the focus of the analysis, both parameters were fixed to the values given by the PDG [31, Summary Tables] to reduce the number of free fit parameters.

This only leaves the complex canonical amplitudes $A_{L,S}^{(\psi(2S)\to X\phi)}$, $A_{J_X,0,L,S}^{(X\to\pi\pi)}$, and $A_{1,0}^{(\phi\to K^+K^-)}$, as well as the production coupling strengths $\alpha_{L,S}^{(f_0)}$, and $\alpha_{L,S}^{(f_2)}$, and non-resonant coupling constants $\tilde{b}_c^{(i)}$, and $\tilde{b}'_c$ of the P-vectors, as possible fit parameters. In every element of the sum, which amounts to the total reaction amplitude, is a product of all three canonical amplitudes multiplied by either one of the production coupling strengths, or one of the non-resonant coupling constants. Thus, each element of the sum is depending solely on the product of the parameters, rather than the parameters themselves, leading to a very unstable fit, if all of them are used for the optimization. Therefore, only the coupling constants of the P-vectors, and the phases of the complex canonical amplitudes $A_{J_X,0,L,S}^{(X\to\pi\pi)}$ are left to be optimized by the fit. The magnitudes of $A_{J_X,0,L,S}^{(X\to\pi\pi))}$, as well as all other canonical amplitudes are set to one. Not the absolute phases, but only the relative phases between the different partial waves influence the model. In order to obtain the relative phase information directly and to simplify the fit, the arbitrarily chosen phase of $A_{2,0,0,1}^{(\text{D-wave}\to\pi^0\pi^0)}$ was set to zero, meaning that every other phase is relative to this one. Also, only the non-resonant couplings for the channel $\pi\pi$ were used, for every other channel they were set to zero.

Until now, all discussion was done for a general $K^+K^-\pi\pi$ final state, but for this work, a coupled channel fit was performed, using the data sets and phase space Monte-Carlo samples for the $K^+K^-\pi^+\pi^-$ and $K^+K^-\pi^0\pi^0$ final states. For the coupled channel fit, the sum of the negative logarithmic likelihoods for both final states were minimized:

$$-\ln\mathcal{L}_{\text{tot}}(\vec{\theta}_{\pi^+\pi^-},\vec{\theta}_{\pi^0\pi^0}) = -\ln\mathcal{L}_{\text{ext}}(\vec{\theta}_{\pi^+\pi^-}) - \ln\mathcal{L}_{\text{ext}}(\vec{\theta}_{\pi^0\pi^0}), \tag{6.53}$$

with $\vec{\theta}_{\pi^+\pi^-}$ being the model parameters for the $\pi^+\pi^-$ final state, and $\vec{\theta}_{\pi^0\pi^0}$ being the parameters for the $\pi^0\pi^0$ final state. Most parameters, like the production coupling strength $\alpha_{L,S}^{(f_0)}$, are shared between the two models, the only final state exclusive parameters are the canonical amplitudes $A_{L,S}^{X\to\pi^+\pi^-}$ and $A_{L,S}^{X\to\pi^0\pi^0}$. Also, a factor W was multiplied to the amplitude for the $\pi^+\pi^-$ final state, to account for scaling effects, which are independent from both the angles and the energies. Such scaling effects can for example result from the fact that the branching ratio of $\pi^0\to\gamma\gamma$. After this discussion, the 246 possible parameters of the model were reduced to a total of 48 free fit parameters. The results of the fit will be presented and discussed in the next section.

6.2.3 Results

In this section, the results of the coupled channel fit to the two final states $K^+K^-\pi^+\pi^-$ and $K^+K^-\pi^0\pi^0$, will be presented and discussed. To visualize the fit result, multiple histograms containing angular and invariant mass distributions of the data, and the projection of the optimized model, will be shown. To get a projection of the total reaction amplitude onto different spectra, each event of the accepted phase space Monte-Carlo samples was weighted by the intensity of the total reaction amplitude for the four-momenta of the event. With these weighted events, the different histograms were first filled, and then scaled by the ratio between data and Monte-Carlo events. The results of this projection method are drawn as red histograms. Additionally, this projection method was repeated using only the intensity of the S-wave contributions in the total reaction amplitude, and again only using the D-wave contributions. S-wave contributions are drawn in blue, while the D-wave contributions are drawn in green.

The results for the angular distributions of the helicity angles can be seen in Fig. 6.14 for the $K^+K^-\pi^+\pi^-$ final state particles, and in Fig. 6.15 for the $K^+K^-\pi^0\pi^0$ final state particles. Overall, the model describes the general shapes of the angular distributions remarkably well. It correctly incorporates efficiency effects resulting from the geometry of the multilayer drift chamber, leading to the decrease of events for higher $|\cos\theta_X|$. This reduction in efficiency is more drastic in the $\pi^0\pi^0$ final state because the photons, from which the π^0 mesons are reconstructed, have to be detected in the electromagnetic calorimeter. Photons resulting from the decay of a π^0 meson are boosted in the direction of its momentum, leading to a correlation between their angular distributions and the angular distribution of the π^0 meson. Thus, due to the lower detection efficiency of the EMC at its end-caps, it is expected, that the detection efficiency of π^0 states is also reduced for higher $|\cos\theta_X|$. Additionally, the probability that one of the π^0 meson's daughter photons has an angle outside the detection range, increases for higher $|\cos\theta_X|$, leading to a further reduction in efficiency. Another effect, which can be seen in data, and was successfully described by the model, is the efficiency reduction resulting from the signal selection. This is especially apparent in the $\cos\theta_\pi$ spectra, where the dip around ± 0.85 results from the veto of the $K^*(892)$ mesons. Pions resulting from the decay of a $K^*(892)$ resonance seem to have a strong preference for polar angles of about 27° in the $\pi\pi$ helicity frame, leading to the sharp dip in the spectra. The reason for this behavior is unknown, but was empirical validated by looking at the spectra before and after the cut (cf. Fig. A.2).

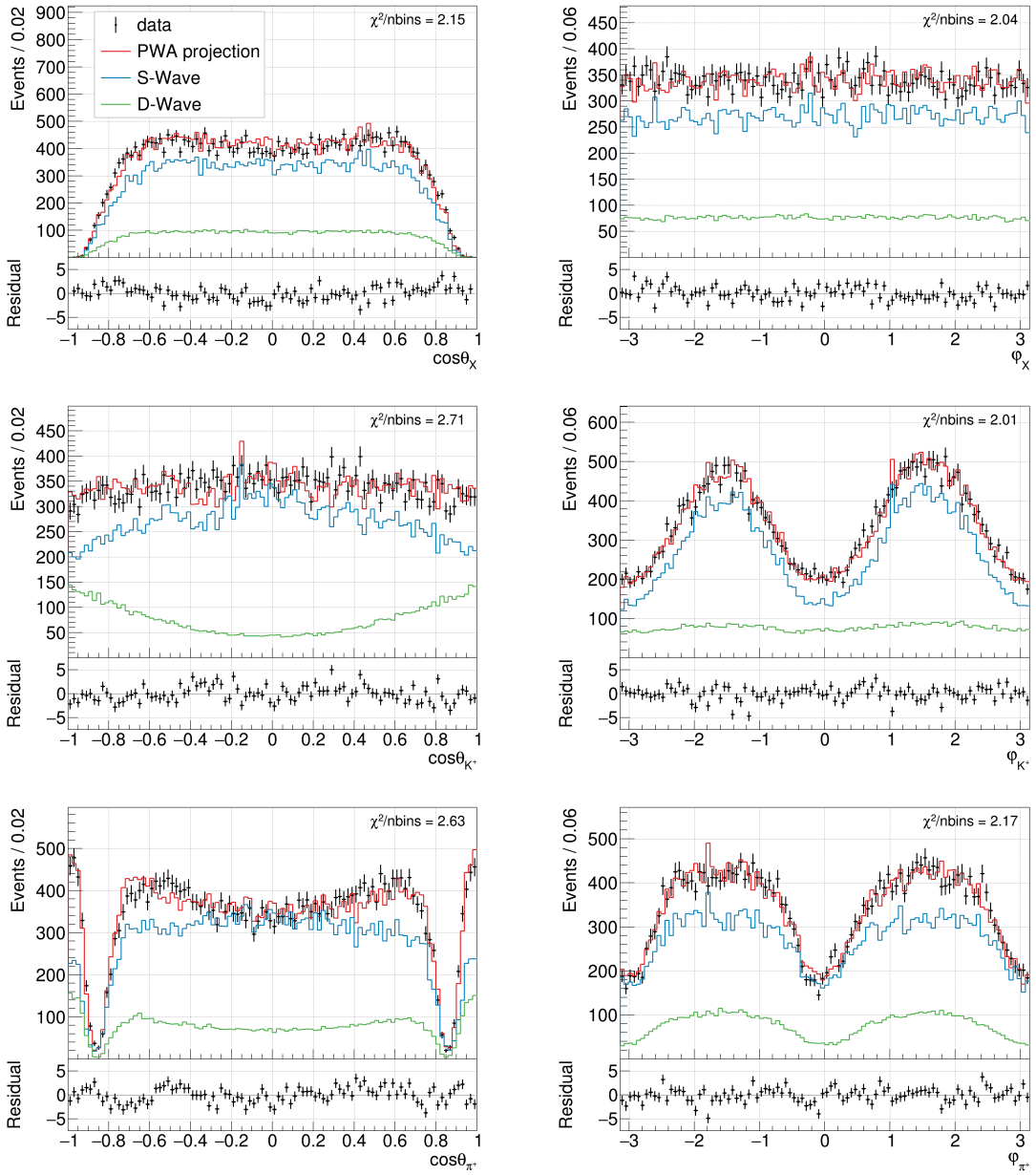

Figure 6.14: Angular distribution histograms of the azimuthal helicity angle φ (right) and cosine of the polar helicity angle θ (left), for the $K^+K^-\pi^+\pi^-$ final state particles. A depiction of the different helicity frames can be seen in Fig. 6.13. The distribution of data events is shown in black, while the projection of the fit result is shown in red. The projection was split into the contribution of the S-wave (blue), and the contribution of the D-wave (green). Below the graphs the residuals between the data and the fit projection are shown, with error bars in y direction, which are the size of the standard deviation σ. At the top right of each histogram, the χ^2 value of the projection, divided by the number of non-empty bins in the histogram can be seen.

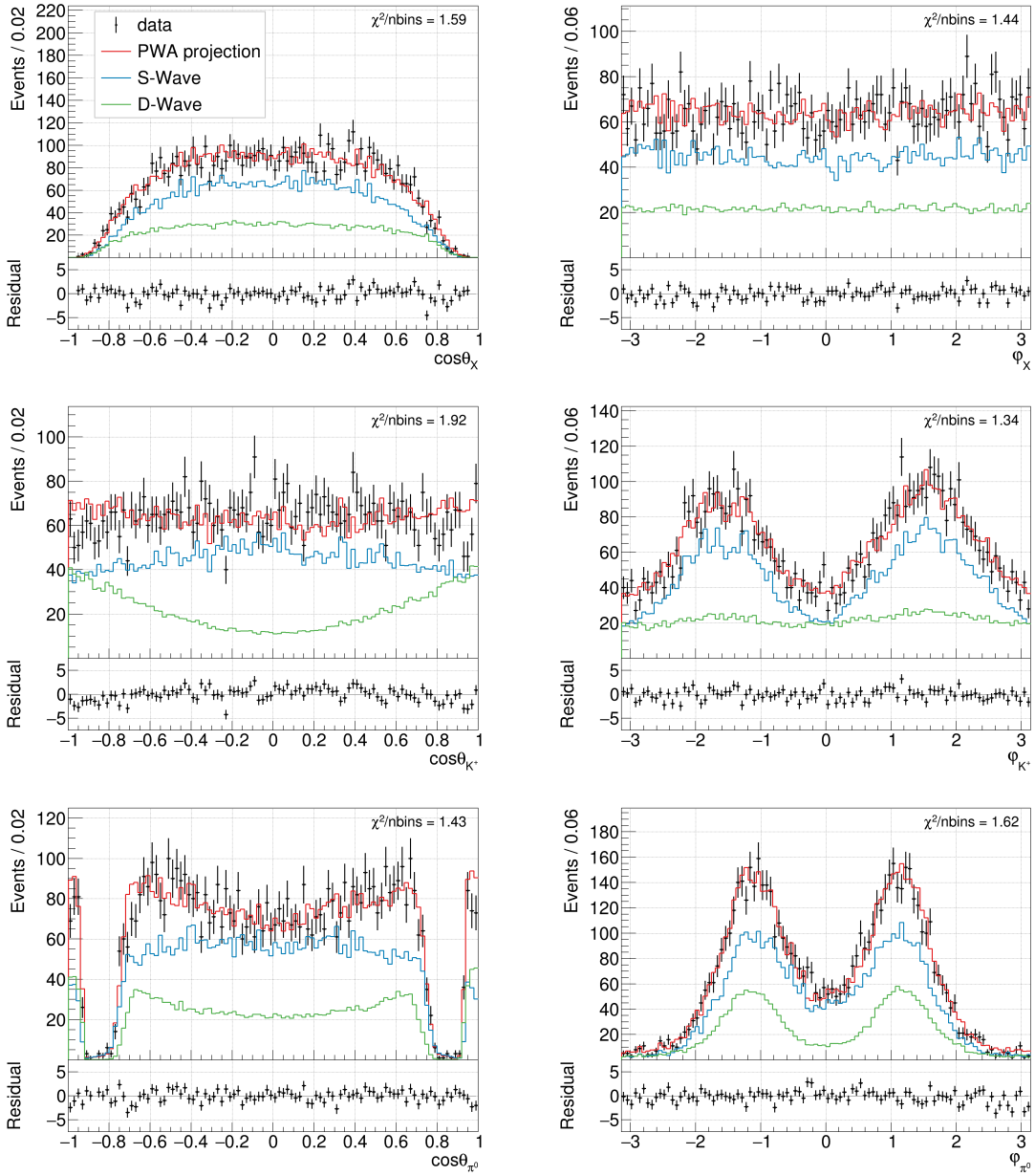

Figure 6.15: Angular distribution histograms of the azimuthal helicity angle φ (right) and cosine of the polar helicity angle θ (left), for the $K^+K^-\pi^0\pi^0$ final state particles. A depiction of the different helicity frames can be seen in Fig. 6.13. The distribution of data events is shown in black, while the projection of the fit result is shown in red. The projection was split into the contribution of the S-wave (blue), and the contribution of the D-wave (green). Below the graphs the residuals between the data and the fit projection are shown, with error bars in y direction, which are the size of the standard deviation σ. At the top right of each histogram, the χ^2 value of the projection, divided by the number of non-empty bins in the histogram can be seen.

Next, the invariant mass spectra shown in Fig. 6.17 for the $K^+K^-\pi^+\pi^-$ final state particles, and in Fig. 6.18 for the $K^+K^-\pi^0\pi^0$ final state particles, will be discussed. Generally, the model seems to describe the invariant mass distributions of the $K\pi$, $\pi\pi K$, and $KK\pi$ systems well, without the incorporation of resonances decaying into these subsystems. In all $K\pi$ and $KK\pi$ spectra a dip can be observed, which results from the $K^*(892)$ veto. This efficiency effect resulting from the signal selection is also incorporated by the fit. The only notable deviation between the model and the data can be seen around 1.25 GeV in the $K^\pm\pi^0$ mass spectrum. No resonance is expected for the $K^\pm\pi^0$ system in this mass region, and it does not seem like a reflection from other spectra, thus it is unclear what causes this deviation.
One shortcoming of the current model is the description of the ϕ resonance. Unlike the model used for the one-dimensional fit of the ϕ resonance in Section 6.1.2, the description in this model does not include effects resulting from the energy resolution of the detector. This results in an underestimation of the data at the flanks and an overestimation around the maximum. The lacking description is especially evident in the K^+K^- spectrum of the $K^+K^-\pi^+\pi^-$ final state. The reason for this could be the higher background content in said channel, which is not included in the model, e.g. background containing a ρ^0 resonance, which will be discussed in the next paragraph. Incorporating a convolution with a Gaussian is unfortunately not possible within the PAWIAN framework. Possible solutions and alternatives will be presented in Chapter 7.
Now the $\pi\pi$ invariant mass spectra will be discussed. The main feature of the spectra is the peaking $f_0(980)$ resonance. Its asymmetry and general shape is well described, but larger deviations can be seen at the left flank of the peak. One reason for the systematic underestimation of the data by the optimized model would be the missing description of possible ρ^0 resonances in the $\pi^+\pi^-$ spectrum. The corresponding background reaction would be $\psi(2S) \to K^+K^-(\rho^0 \to \pi^+\pi^-)$, which is listed as the second highest background contribution in the inclusive Monte-Carlo sample (cf. Table A.9). The inclusion of the ρ^0 resonance in the model is not possible without extending the isobar approach, as it requires the description of the three-body decay $\psi(2S) \to K^+K^-\rho^0$.
Between 1 GeV and 2 GeV the model is able to describe the rough shape of the data, but fails at the description of the finer substructures. However, considering that most of the parameterization of the $\pi\pi$ dynamics was not optimized by the fit, but comes from an analysis, which investigated completely different production channels, the model works remarkably well. This also highlights the model independent character of the parameterization. There are multiple reasons for the deviations of the model from the data. It is possible, that there are contributions of other resonances in the spectra, like the ρ^0 in the $\pi^+\pi^-$ spectrum, which are not included in the model. No resonances above 2 GeV are currently included in the model, which could also affect the rest of the spectra when the fit tries to compensate for the lacking description. Candidates for the inclusion of heavier states would be for example other f_2 resonances, like the $f_2(2300)$, or the $J^{PC} = 4^{++}$ resonance $f_4(2050)$. To compare models including different resonances, or other non-resonant contributions, hypothesis tests need to be performed, like

in Ref. [86]. Another possible source for the deviations comes from using the parameters from Ref. [85]. The analysis is much more extensive than this work, testing different hypothesis and including three decay channels, but the analyzed data has a much smaller phase space and excluded two channels of the S-wave model, and one channel of the D-wave model. To use the full potential of the parameterization, all channels have to be considered, and the decay channel couplings, $g_b^{f_0}$ and $g_b^{f_2}$, as well as the bare resonance's masses, m_{f_0} and m_{f_2}, should be used as free fit parameters.

The results for the fit parameters are listed in Tables A.14 and A.15. It is difficult to interpret these values for the same reasons mentioned before. Their correlations to the decay channel couplings $g_a^{(R)}$ leads to high variance for resonances with small couplings to the $\pi\pi$ decay channel. In a fit incorporating all channels this effect would be compensated by the contributions of other decay channels.

Independent from the fit, the production preference for resonances with high $s\bar{s}$ content due to the chosen signal condition containing a ϕ meson can be seen very well in the $\pi\pi$ invariant mass spectra. The effect becomes especially apparent when comparing the invariant mass distributions of the $\pi\pi$ system to $\pi\pi$ spectra from an analysis, using $J/\psi \to \omega\pi\pi$ as the signal hypotheses. The $\pi\pi$ invariant mass spectra of said reaction where e.g. extracted in Refs. [79, 87], and both the $\pi^+\pi^-$ spectrum resulting from this work, as well as the $\pi\pi$ spectra from Ref. [87] are depicted in Fig. 6.16 for comparison. An advantage of comparing these spectra is that the coupling to the decay channel is the same for both reactions, but the coupling to the production is different. Assuming that exchanging the $\psi(2S)$ meson with an J/ψ meson only effects the size of the phase space, all differences between the spectra can be accounted to the choice of either the ϕ meson, or the ω meson in the signal hypothesis. No contributions of the $f_0(980)$ resonance can be seen in the $\pi\pi$ spectra using the ω meson hypothesis, but significant contributions likely coming from the $f_0(500)$ and $f_2(1270)$. This observation is in strong contrast to the spectra presented in this work, where the $f_0(980)$ resonance is dominant, while no $f_0(500)$ contributions are visible, and the $f_2(1270)$ seems to be strongly suppressed, even though its branching ratio to $\pi\pi$ is $(84.2^{+2.9}_{-0.9})\%$, according to the PDG [31, Summary Tables]. The $f_0(500)$ is assumed to be a state, which only contains $u\bar{u}$ and $d\bar{d}$ content (cf. Sections 2.3 and 2.4), while also high $u\bar{u}$ and $d\bar{d}$ content is predicted for the $f_2(1270)$ [88, 89]. This supports the hypothesis that the spectra presented in this work predominantly show resonances with a high $s\bar{s}$ content, and which have a reasonable coupling to two pions. The second part of this statement is especially important when searching for the $f_2'(1525)$, which is assumed to have a high $s\bar{s}$ content [88, 89], but has, according to the PDG [31, Summary Tables], a branching ratio of $(8.3 \pm 1.6) \times 10^{-3}$ for the decay into two pions, which explains its lacking contribution in the spectra. From this argument follows, that the $f_0(980)$ should have large $s\bar{s}$ contributions, due to its dominance in the spectra of this work, which was already proposed, e.g., in Ref. [90].

This assumption is further reinforced when comparing the spectra to the results of the scalar pion form factor, resulting from dispersion theory [91], which can be seen in Fig. 6.19. The non-strange form factor incorporates a broad $f_0(500)$ resonance, while the strange form factor clearly shows a peak corresponding to the $f_0(980)$.
This concludes the discussion of the analysis performed in this work. The next chapter will summarize the results and give an outlook of possible next steps, for improving and continuing the analysis.

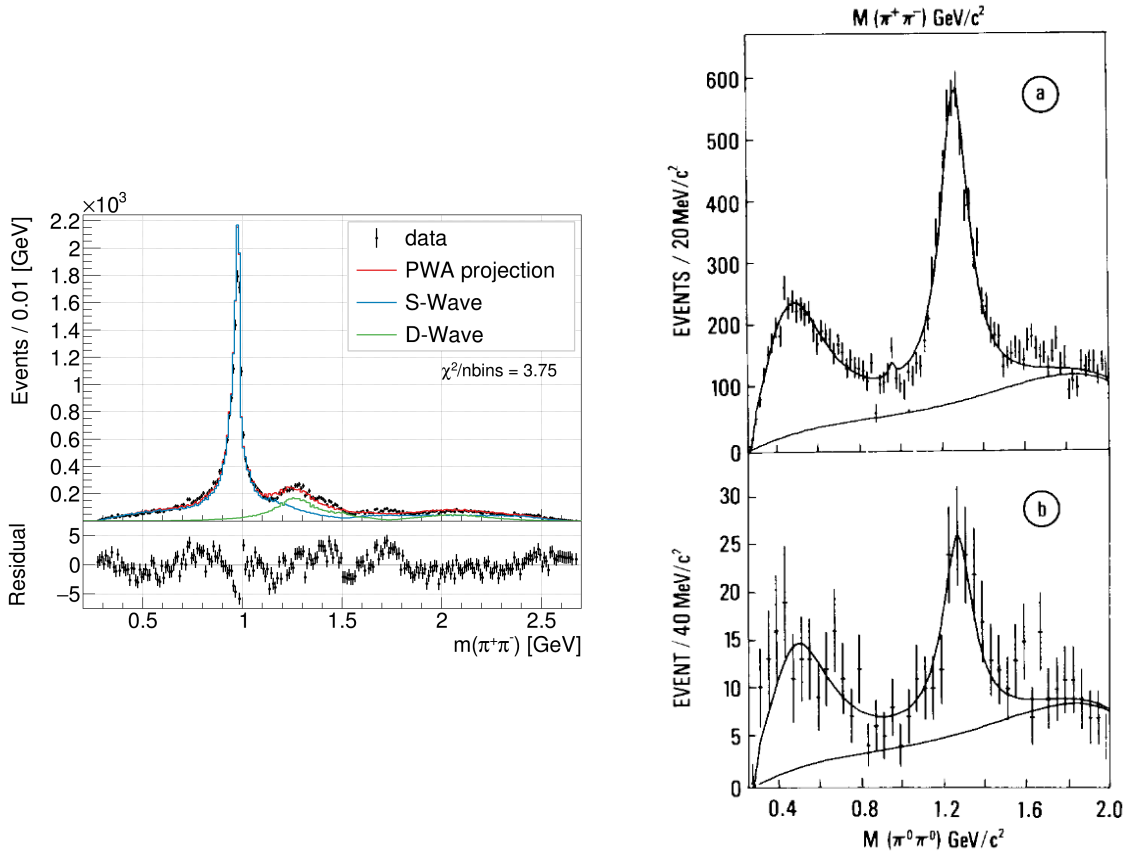

Figure 6.16: **Left**: $\pi^+\pi^-$ invariant mass spectrum with projections of the partial wave analysis, resulting from the analysis of the reaction $\psi(2S) \to \phi\pi^+\pi^-$ in this work. **Right**: $\pi\pi$ invariant mass spectra with plotted fit results from the analysis of the reactions $J/\psi \to \omega\pi\pi$ performed in Ref. [87].

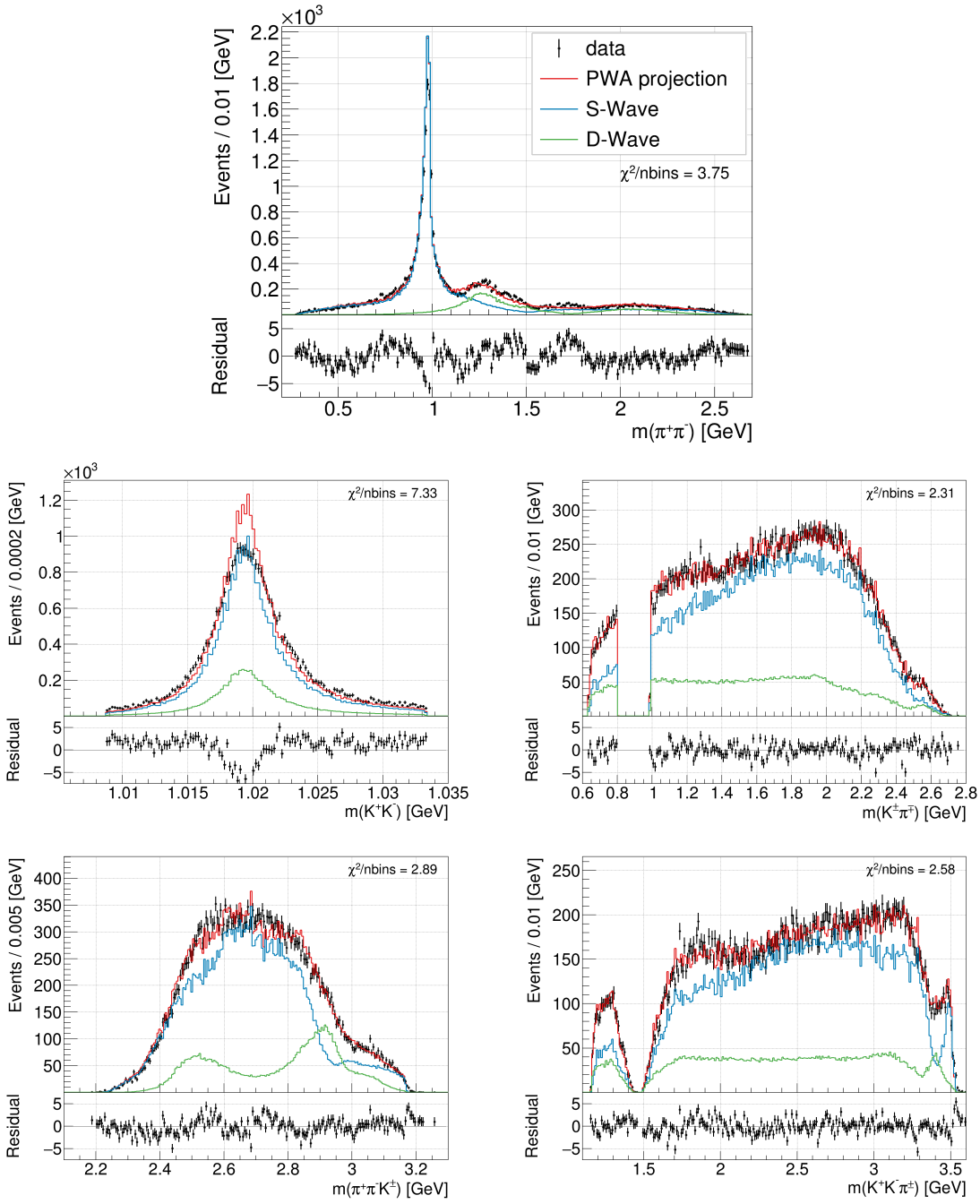

Figure 6.17: Invariant mass histograms for the $K^+K^-\pi^+\pi^-$ final state particles. The distribution of data events is shown in black, while the projection of the fit result is shown in red. The projection was split into the contribution of the S-wave (blue), and the contribution of the D-wave (green). Below the graphs, the residuals between the data and the fit projection are shown, with error bars in y direction, which are the size of the standard deviation σ. At the top right of each histogram, the χ^2 value of the projection, divided by the number of non-empty bins in the histogram can be seen.

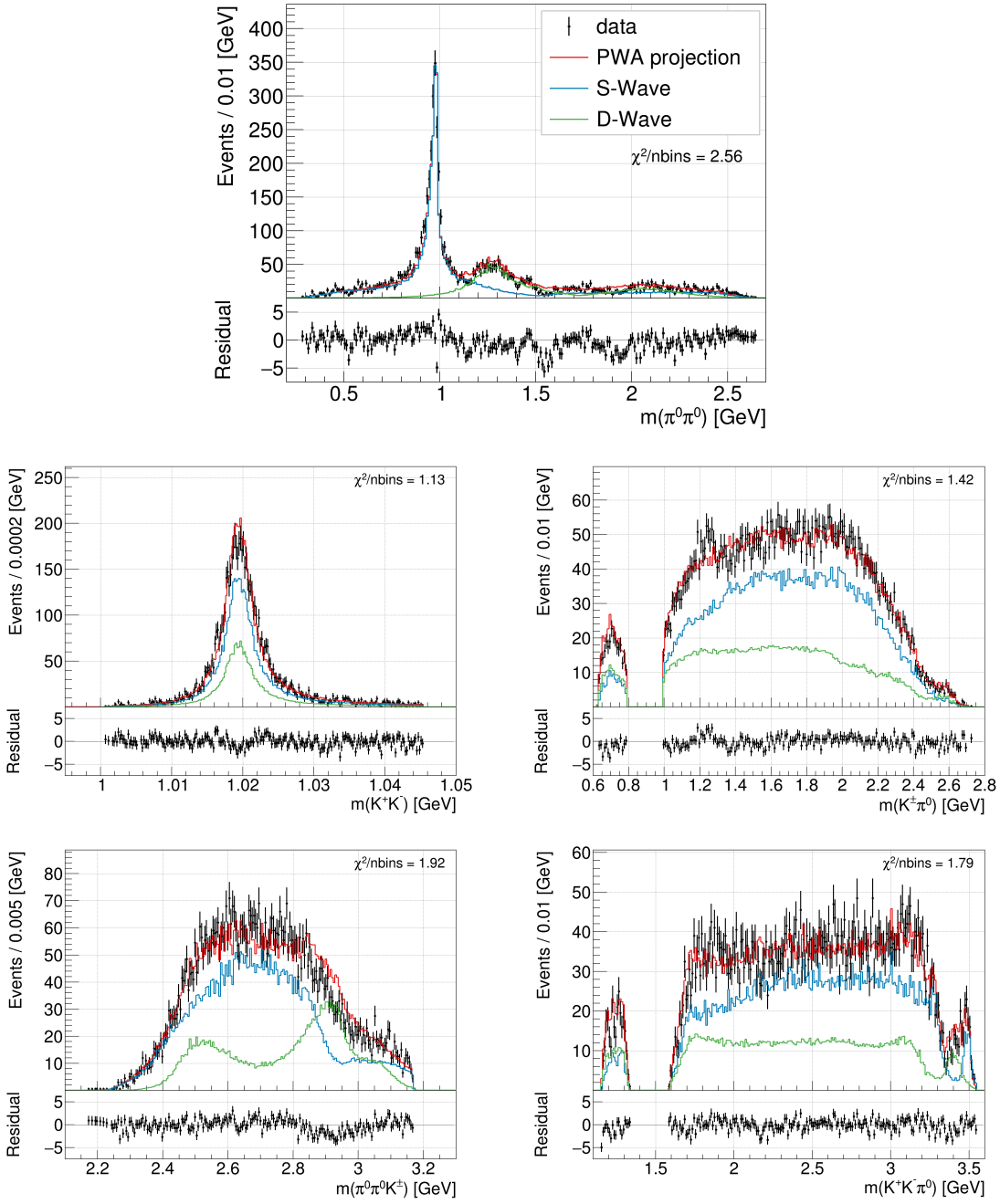

Figure 6.18: Invariant mass histograms for the $K^+K^-\pi^0\pi^0$ final state particles. The distribution of data events is shown in black, while the projection of the fit result is shown in red. The projection was split into the contribution of the S-wave (blue), and the contribution of the D-wave (green). Below the graphs, the residuals between the data and the fit projection are shown, with error bars in y direction, which are the size of the standard deviation σ. At the top right of each histogram, the χ^2 value of the projection, divided by the number of non-empty bins in the histogram can be seen.

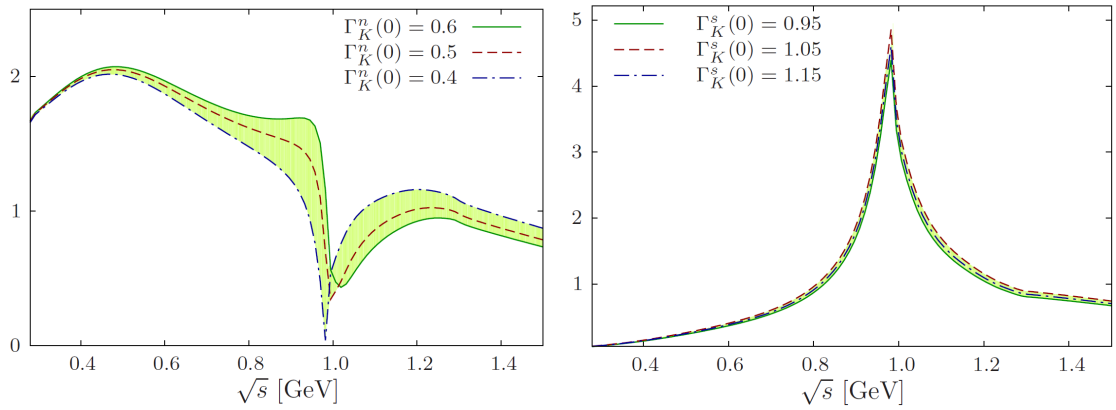

Figure 6.19: Absolute values of the scalar pion form factors plotted against the center-of-mass energies $\sqrt{s}$ of two scattered pions. On the left, the form factor corresponding to the scattering of non-strange quark content is plotted, while the form factor, which is plotted on the right, corresponds to the scattering of strange quark content. For both form factors the results for three different normalizations are plotted. The green uncertainty band indicates the allowed range for different normalizations. Figures taken from Ref. [91].

7. Conclusion and Outlook

In this chapter the results of this work will be summarized, and an outlook will be given for further analysis.

As the first part of the analysis, the information provided by the detector systems of BESIII and the results of kinematic and vertex fits were successfully used to select events containing the two final states $K^+K^-\pi^+\pi^-$ and $K^+K^-\pi^0\pi^0$ from the 2021 $\psi(2S)$ data set provided by the BESIII collaboration. From the resulting data samples, events containing the signal reactions $\psi(2S) \to \phi\pi\pi$ and $\psi(2S) \to \phi(X \to \pi\pi)$ were extracted by setting various restrictions on the properties of the events. Selection criteria were applied to the χ^2_{NC} value of the kinematic fit, only events were accepted within a signal region around the invariant mass of the ϕ resonance, and all events were rejected in a veto region around the invariant mass of the $K^*(892)$ resonance. After all selection criteria were applied, a background to data ratios of 4.67% for the $\pi^+\pi^-$ and 2.20% for the $\pi^0\pi^0$ channel were archived.

For the optimization of the signal region, a fit to the ϕ resonance in the K^+K^- invariant mass spectra was performed. These fits provided information about the distributions of signal and background events and enabled the extraction of the number of observed signal events. With the number of observed signal events, the branching ratios $\mathrm{BR}(\psi(2S) \to \phi\pi^+\pi^-) = (1.25 \pm 0.01) \times 10^{-4}$ and $\mathrm{BR}(\psi(2S) \to \phi\pi^0\pi^0) = (0.492 \pm 0.007) \times 10^{-4}$ were successfully determined. The branching ratio of the process $\psi(2S) \to \phi\pi^+\pi^-$ agrees with the value given by the PDG [31, summary tables], but up to this point in the analysis, the result has an uncertainty that is more than one order of magnitude lower. For $\psi(2S) \to \phi\pi^0\pi^0$ no branching ratio was listed thus far. Both branching ratios were compared to their J/ψ counter parts, $J/\psi \to \phi\pi^+\pi^-$ and $J/\psi \to \phi\pi^0\pi^0$, and it was found that both decays are in agreement, within their uncertainties, with the "12% rule" derived from perturbative QCD. Due to isospin symmetry, a factor of two was expected between the branching ratios determined in this work, but the results yield a factor of 2.54 ± 0.04. Contributions from electromagnetic decays, which do not conserve isospin, could be responsible for the deviation. Another source contributing to the deviation could result from the method used to determine the efficiency. It did not account for the effects of different angular momentum transitions, and intermediate resonances in the $\pi\pi$ channel, onto the distribution of events in the phase space. To improve the accuracy of the efficiency calculation, the results of the partial wave analysis can be used, to determine weights for the

events of the generated, and accepted Monte-Carlo sample. Generally, comprehensive studies of the systematic uncertainties resulting from the selection criteria and choice of fit model have to be performed to be fully able to discuss the resulting branching ratios.
For subsequent analyses, the approx. 447 million $\psi(2S)$ events provided by the 2009 and 2012 BESIII data sets should be added to the analysis, to reduce the statistical uncertainty. Also, instead of the 500 million inclusive Monte-Carlo events, which were available at the time of the analysis, the recently published full 2.3 billion inclusive Monte-Carlo events from 2021, as well as the newly reconstructed 447 million inclusive events from 2009 and 2012, should be used to gain further inside into the background reactions. Generally, all data and simulations should be reconstructed again, using the recently released BOSS version 7.0.9, to improve the data quality and ensure consistency between the samples.

In the second part of the analysis a partial wave analysis was performed, with the objective to model the complex $\pi\pi$ invariant mass spectra. A fully analytical and unitary model was successfully implemented, which describes the distribution of the four-momenta of the $K^+K^-\pi^+\pi^-$ and $K^+K^-\pi^0\pi^0$ final states. Then the model was fit to said four-momenta of both final states simultaneously using the extended negative logarithmic likelihood method. This method also allowed for the proper incorporation of efficiency effects, by using phase space distributed Monte-Carlo samples.
The helicity angle distributions in the three different helicity frames were described exceptionally well by the model. Generally, the description of the invariant mass distributions was also satisfactory. A systematic deviation of the data from the model was found in the invariant mass spectrum of the $K^\pm\pi^0$ system around 1.25 GeV, whose origin is unknown. Additionally, the model could not fully describe the line shape of the comparatively narrow ϕ resonance due to its increased width resulting from the energy resolution of the detector. Therefore, the model should be improved by convoluting the used Breit-Wigner distribution with a Gaussian. The general shape of the $\pi\pi$ spectra was reproduced by the model, providing a good description of the $f_0(980)$ resonance, but it was unable to describe the finer substructures between 1 GeV and 2 GeV. The performance of the model is still impressive, respecting that most of the parameters were taken from a previous work, which used different data samples, with smaller phase space, additional resonances, and other production mechanisms. This highlights the versatility of the approach, and the model independent character of the parameters.
For future analysis, the aim should be to perform a multi-channel fit to all channels considered by the model, namely the 4π, $K\bar{K}$, $\eta\eta$, and $\eta\eta'$ channels, to be able to optimize all model parameters. Being independent from the results of previous works also has the advantage that the model itself can be chosen more freely. Different parts of the model could be changed, like the number of resonances, or adding another decay channel. A starting point could be to add another f_2 resonance, like the $f_2(2300)$, and the $\eta\eta'$ decay channel to the description of the D-wave. It is also feasible to change the order of the non-resonant terms or add entirely new decay processes. Another approach would be to test different scattering models. A good contender would be a model using dispersion theory to derive the scalar pion form

factor, presented in Refs. [91, 92]. A comparison between the amplitudes resulting from this approach and the results of this analysis, as well as the analysis of $\psi(2S) \to \phi K\bar{K}$ performed in the thesis of Johannes Bloms [74], can be seen in Fig. 7.1. Although the moduli of the form factors were determined using a different production process, they appear to be similar to the spectra resulting from this and J. Bloms's analyses, providing motivation to implement this parameterization for future analyses. A different way to improve the model is to change the description of the 4π system, which was incorporated into the isobar model, by treating it as a state consisting out of two particles which have the mass and quantum numbers of a pion pair. An improvement to this approximation can be done by describing the channel as an effective two ρ or two σ channel, as it was done in Ref. [92].

All different models should then be compared, by using for example the Bayesian information criterion [93], or Akaike information criterion [94], which use the likelihood value resulting from the fit, but are expected to be less dependent on the number of degrees of freedom. After a good model has been found, the next step should be to determine the poles of the dynamical part of the amplitude on the complex $\sqrt{s}$ plane. The physical mass and width of a resonance is defined by the position of the pole, and it is possible to get information like the partial width by calculating the residue of a pole (cf. Section 3.2.3). This information can then be used to gain further inside into the constituents making up the different scalar and tensor particles.

Independent from the physical model, it is advised to compare the used PAWIAN software package to other available packages. PAWIAN allows for an easy and fast way to optimize an amplitude model, even allowing for coupled channel analyses, and providing methods to plot the results. But the options to customize the model, or include new parameterizations are very limited, and when looking at the computation performance, the optimization itself appears to be rather slow, even when using a high level of parallelization and adjusting the resource management. For an analysis using advanced models and more channels, leading to higher statistics, benchmark test should be performed, comparing PAWIAN to other packages, as slow optimization could strongly impair the progress of the analysis. Possible alternative software for the implementation and optimization of amplitude and partial wave models are listed in Ref. [95].

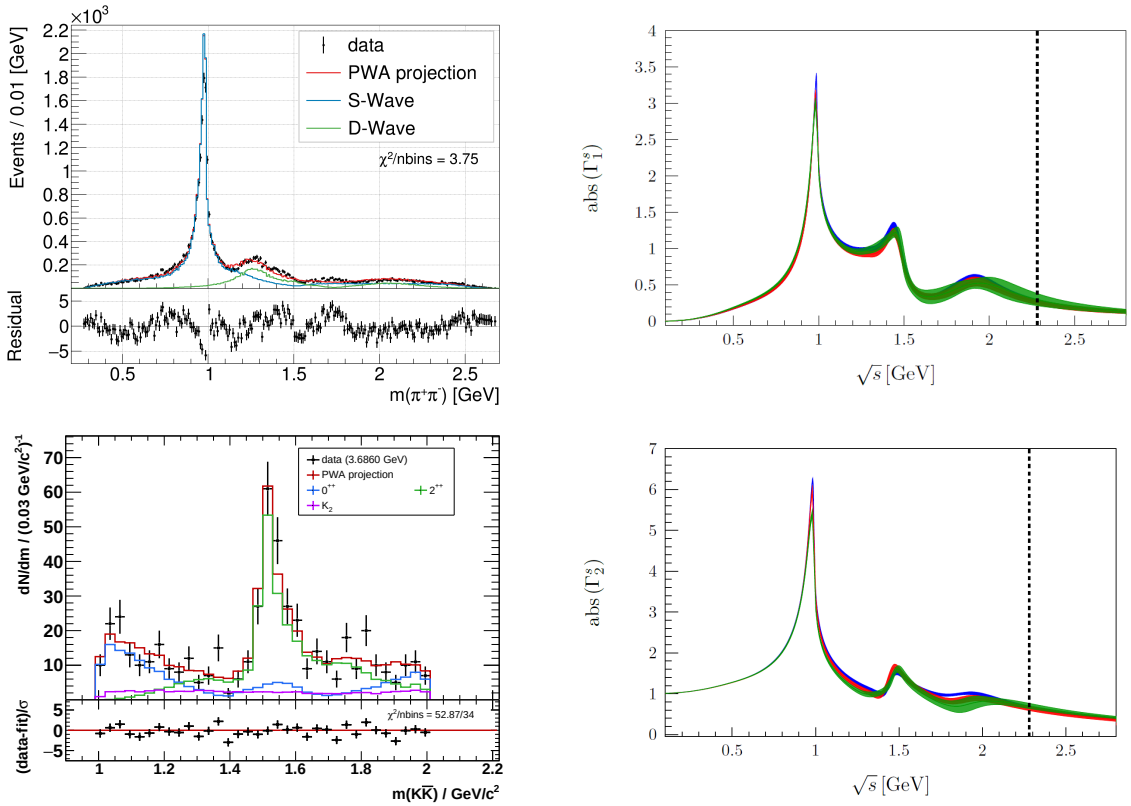

Figure 7.1: On the left, the $\pi\pi$ invariant mass spectrum with the results of the partial wave analysis performed in this work (top), and the $K\bar{K}$ invariant mass spectrum with the results from the analysis performed in the thesis of J. Bloms [74] (bottom) can be seen. As a comparison, the absolute form factors determined by fits on $\bar{B}_s^0 \to J/\psi\pi^+\pi^-$ (top) and $\bar{B}_s^0 \to J/\psi K^+K^-$ (bottom) data, taken from Ref. [92], are shown on the right. The dashed black lines in the figures on the right indicate the kinematic limit of the $\bar{B}_s^0$ decay, and the results of the three different fits are drawn in three different colors.

A. Appendix

A.1 Equations and Relations

A.1.1 Normalized Breit-Wigner Distribution

The normalized relativistic Breit-Wigner probability density function, derived from Ref. [96]:

$$\mathcal{A}_{\mathrm{BW}} = \frac{M \cdot \Gamma}{s^2 - M^2 - i \cdot M \cdot \Gamma} \tag{A.1}$$

with the Breit-Wigner mass M, Breit-Wigner width Γ, and s being the Mandelstam variable.

A.1.2 Blatt-Weisskopf Factors

The Blatt-Weisskopf factors for angular momentum quantum numbers up to $l = 4$, taken from [97]:

$$\begin{aligned}
B_0(z) &= 1, \\
B_1(z) &= \sqrt{\frac{2z^2}{1+z^2}}, \\
B_2(z) &= \sqrt{\frac{13z^4}{(z^2-3)^2 + 9z^2}} \\
B_3(z) &= \sqrt{\frac{277z^6}{z^2(z^2-15)^2 + 9(2z^2-5)^2}} \\
B_4(z) &= \sqrt{\frac{1274z^8}{(z^4-45z^2+105)^2 + 25z^2(2z^2-21)^2}}.
\end{aligned} \tag{A.2}$$

A.1.3 Wigner D-Matrix Identities

Identities of the Wigner D-Matrix taken from [48, 49].

$$D^{j}_{mk}(\alpha,\beta,\gamma)D^{j'}_{m'k'}(\alpha,\beta,\gamma) = \sum_{J=|j-j'|}^{j+j'} \langle jmj'm' \mid J(m+m')\rangle \cdot \langle jkj'k' \mid J(k+k')\rangle D^{J}_{(m+m')(k+k')}(\alpha,\beta,\gamma) \tag{A.3}$$

$$\langle J, M, \lambda_1', \lambda_2' | \theta, \varphi, \lambda_1, \lambda_2\rangle = \delta_{\lambda_1,\lambda_1'}\delta_{\lambda_2,\lambda_2'}\sqrt{\frac{2J+1}{4\pi}}D^{J}_{M,\lambda_1-\lambda_2}(\varphi,\theta,-\varphi) \tag{A.4}$$

A.1.4 Gaussian Distribution

The probability density function of the Gaussian distribution is defined as:

$$g(x) = \frac{1}{\sigma\sqrt{2\pi}}e^{-\frac{1}{2}\left(\frac{x-\mu}{\sigma}\right)^2}, \tag{A.5}$$

where σ^2 is the variance and μ is the mean value of the distribution.
The cumulative distribution function of the Gaussian distribution is defined as:

$$G(x) = \frac{1}{2}\left[1 + \operatorname{erf}\left(\frac{x-\mu}{\sigma\sqrt{2}}\right)\right], \tag{A.6}$$

with $\operatorname{erf}(x)$ being the Gauss error function, which is defined as:

$$\operatorname{erf}(x) = \frac{2}{\sqrt{\pi}}\int_0^x e^{-t^2}dt. \tag{A.7}$$

A.1.5 Asymmetric Gaussian

The asymmetric Gaussian is defined as:

$$g_{\text{asym}}(x) = \frac{A_{\text{G}}}{\sqrt{2\pi}\sigma_{\text{asym}}}e^{-\frac{(x-\mu)^2}{2\sigma^2_{\text{asym}}}}, \tag{A.8}$$

with an asymmetric standard deviation σ_{asym}:

$$\sigma_{\text{asym}} = \begin{cases}\sigma_{\text{L}}, & \text{for } x \le \mu \\ \sigma_{\text{R}}, & \text{for } x > \mu,\end{cases} \tag{A.9}$$

μ being the mean, and A_{G} the amplitude of the distribution.

A.1.6 Poisson Distribution

The discrete Poisson distribution gives the probability, that a discrete number of events k occurs, if the variance/mean λ of the distribution is known. The events themselves have to be independent of each other. If this is fulfilled, then the probability mass function (PMF) is defined as:

$$P(k;\lambda) = \frac{\lambda^k}{k!}\cdot e^{-\lambda}. \tag{A.10}$$

A.1.7 Least-squares Fit Method

Least-squares fitting is a method used for finding the set of parameters $\vec{\theta}$ for which a given model $f(x, \vec{\theta})$ best describes a given data sample, with N data points. Each data point $\vec{d}_i$ contains a y_i value for each independent x_i value. To fit the model function to these data points, the vertical deviation R^2 is minimized:

$$R^2 = \sum_{i=1}^{N} \left[y_i - f(x_i, \vec{\theta}) \right]^2 . \tag{A.11}$$

For y_i values with uncertainties σ_i, that can be assumed to be Gaussian distributed, Eq. (A.11) can be redefined as the χ^2 function

$$\chi^2 = \sum_{i=1}^{N} \frac{\left[y_i - f(x_i, \vec{\theta}) \right]^2}{\sigma_i^2}, \tag{A.12}$$

which still uses the vertical deviation, but also incorporates the uncertainty of the data, allowing for an estimation of the parameter uncertainty. The minimized χ^2 value can be divided by the degrees of freedom of the fit, which is the number of data points minus the number of free fit parameters, to get the reduced χ^2_r. For Gaussian distributed y_i values, the χ^2_r value gives the goodness-of-fit, which, for a model fully describing the data within its uncertainties, would be equal to 1. If χ^2_r is significantly larger than 1, then the model does not describe every aspect of data, which means it lacks parameters, or uses the wrong parameterization. In this case, it is also possible that the uncertainty of the data was underestimated. For χ^2_r values significantly below 1, the model is over-determined, which means, that either the model incorporates to many parameters, or the uncertainty of the data is overestimated.

A.2 Tables

A.2.1 BESIII Experiment Design Parameters

Table A.1: Design parameters of the BEPCII according to [51].

Parameter	Value
Center of mass energy [GeV]	$2-4.6$
Circumference [m]	237.5
Number of rings	2
RF frequency f_{rf} [MHz]	499.8
Peak luminosity [$\mathrm{cm}^{-2}\mathrm{s}^{-1}$]	$1 \cdot 10^{33}$
Number of bunches	2×93
Beam current [A]	2×0.91
Bunch spacing [m], [ns]	2.4, 8
Bunch length [cm]	1.5
Bunch width [μm]	~ 380
Bunch height [μm]	~ 5.7
Relative energy spread	5×10^{-4}
Crossing angle [mrad]	± 11

A.2.2 Monte-Carlo Simulations

Table A.2: Number of generated Monte-Carlo events, as well as the BesEvtGen [60] generation models used for the corresponding reactions.

Reaction	Model	Generated Events ($\times 10^6$)
$\psi(2S) \to (\phi \to K^+K^-)\pi^+\pi^-$	PHSP	5
$\psi(2S) \to (\phi \to K^+K^-)\pi^0\pi^0$	PHSP	5
$\psi(2S) \to K^+K^-\pi^+\pi^-$	PhspStepf	10.055
$\psi(2S) \to K^+K^-\pi^+\pi^-$	PHSP	41
$\psi(2S) \to K^+K^-\pi^0\pi^0$	PhspStepf	9.855

A.2.3 Charged Track Selection Criteria

Table A.3: Selection criteria for charged tracks. Tracks have to fulfill the following conditions to get accepted.

Parameter	Condition
radial distance V_r between the interaction point and the primary vertex	$V_r < 1\,\text{cm}$
axial distance V_z between the interaction point and the primary vertex	$V_z < 10\,\text{cm}$
polar angle θ in the detector frame	$\lvert\cos\theta\rvert < 0.93$
probability p for the particle hypothesis	$p > 10^{-5}$

A.2.4 Neutral Particle Selection Criteria

Table A.4: Selection criteria for neutral particle. Tracks have to fulfill the following conditions to get accepted.

Parameter	Condition
shower time τ	$\tau < 700\,\text{ns}$
shower energy E_γ in the barrel of the EMC	$E_\gamma > 25\,\text{MeV}$
shower energy E_γ in the end-caps of the EMC	$E_\gamma > 50\,\text{MeV}$
angle α to the next charged track	$\alpha > 10°$

A.2.5 Calculation of the Branching Ratio

Table A.5: Parameters and their uncertainties used for the calculation of the branching ratios of $\psi(2S) \to \phi\pi^+\pi^-$ and $\psi(2S) \to \phi\pi^0\pi^0$. The branching ratios for $\phi \to K^+K^-$ and $\pi^0 \to \gamma\gamma$ were taken from the PDG [31, summary tables]

Parameter	$K^+K^-\pi^+\pi^-$	$K^+K^-\pi^0\pi^0$
A	32.3 ± 0.2	6.97 ± 0.08
h	1 MeV	1 MeV
$N_{\phi,\text{obs}}$	32353±201	6971±86
$N_{\text{MC,gen}}$	5×10^6	5×10^6
$N_{\text{MC,acc}}$	1159929 ± 1077	651270 ± 807
ϵ	$(23.19 \pm 0.02)\,\%$	$(13.02 \pm 0.01)\,\%$
$\text{BR}(\phi \to K^+K^-)$	$(49.1 \pm 0.5)\,\%$	
$\text{BR}(\pi^0 \to \gamma\gamma)$	$(98.820 \pm 0.034)\,\%$	
$N_{\psi(2S)}$	$(2264 \pm 9) \times 10^6$	
BR	$(1.25 \pm 0.01) \times 10^{-4}$	$(0.492 \pm 0.007) \times 10^{-4}$

A.2.6 Inclusive Reactions

$K^+K^-\pi^+\pi^-$ Final State

Table A.6: Signal reactions, according to the inclusive MC sample for the $K^+K^-\pi^+\pi^-$ final state, with their corresponding number of events after all selection criteria described in this work, except for the $K^*(892)$ veto.

Reaction	Number of Events
$\psi(2S) \to (\phi \to K^+K^-)\pi^+\pi^-$	3010
$\psi(2S) \to (f_0 \to \pi^+\pi^-)(\phi \to K^+K^-)$	2464
$\psi(2S) \to (f_0(1710) \to \pi^+\pi^-)(\phi \to K^+K^-)$	86
$\psi(2S) \to (f_0 \to \pi^+\pi^-\gamma_{\text{FSR}})(\phi \to K^+K^-)$	27
$\psi(2S) \to (f_2' \to \pi^+\pi^-)(\phi \to K^+K^-)$	13
$\psi(2S) \to (\phi \to K^+K^-)\pi^+\pi^-\gamma_{\text{FSR}}$	6
$\psi(2S) \to (f_0(1710) \to \pi^+\pi^-\gamma_{\text{FSR}})(\phi \to K^+K^-)$	3
$\psi(2S) \to (f_2' \to \pi^+\pi^-\gamma_{\text{FSR}})(\phi \to K^+K^-)$	1
Total number of signal events	5610

Table A.7: Signal reactions, according to the inclusive MC sample for the $K^+K^-\pi^+\pi^-$ final state, with their corresponding number of events after all selection criteria described in this work.

Reaction	Number of Events
$\psi(2S) \to (\phi \to K^+K^-)\pi^+\pi^-$	2580
$\psi(2S) \to (f_0 \to \pi^+\pi^-)(\phi \to K^+K^-)$	2229
$\psi(2S) \to (f_0(1710) \to \pi^+\pi^-)(\phi \to K^+K^-)$	79
$\psi(2S) \to (f_0 \to \pi^+\pi^-\gamma_{\mathrm{FSR}})(\phi \to K^+K^-)$	25
$\psi(2S) \to (f_2' \to \pi^+\pi^-)(\phi \to K^+K^-)$	9
$\psi(2S) \to (\phi \to K^+K^-)\pi^+\pi^-\gamma_{\mathrm{FSR}}$	5
$\psi(2S) \to (f_0(1710) \to \pi^+\pi^-\gamma_{\mathrm{FSR}})(\phi \to K^+K^-)$	3
$\psi(2S) \to (f_2' \to \pi^+\pi^-\gamma_{\mathrm{FSR}})(\phi \to K^+K^-)$	1
Total number of signal events	4931

Table A.8: Background reactions, according to the inclusive MC sample for the $K^+K^-\pi^+\pi^-$ final state, with their corresponding number of events after all selection criteria described in this work, except for the $K^*(892)$ veto.

Reaction	Number of Events
$\psi(2S) \to K^+K^-\pi^+\pi^-$	345
$\psi(2S) \to K^-(K^{*+} \to K^+\pi^-)\pi^+$	138
$\psi(2S) \to K^+K^-(\rho^0 \to \pi^+\pi^-)$	127
$\psi(2S) \to K^+(\bar{K}^{*+} \to K^-\pi^+)\pi^-$	123
$\psi(2S) \to K^-(K_2^{*+} \to K^+\pi^-)\pi^+$	24
$\psi(2S) \to K^+(\bar{K}_2^{*+} \to K^-\pi^+)\pi^-$	19
$\psi(2S) \to (\bar{K}_2^{*+} \to K^-\pi^+)(K^{*+} \to K^+\pi^-)$	5
$\psi(2S) \to (K_1^- \to K^-(\rho^0 \to \pi^+\pi^-))K^+$	5
$\psi(2S) \to (K_2^{*+} \to K^+\pi^-)(\bar{K}_2^{*+} \to K^-\pi^+)$	4
$\psi(2S) \to (K_1^- \to (\bar{K}_0^{*+} \to K^-\pi^+)\pi^-)K^+$	3
$\psi(2S) \to (a_0^0 \to K^+K^-)\pi^+\pi^-$	2
$\psi(2S) \to K^+K^-(\omega \to \pi^+\pi^-)$	2
$\psi(2S) \to K^+K^-(\rho^0 \to \pi^+\pi^-\gamma_{\mathrm{FSR}})$	2
$\psi(2S) \to (\bar{K}_0^{*+} \to K^-\pi^+)(K_2^{*+} \to K^+\pi^-)$	1
$\psi(2S) \to (\bar{K}_0^{*+} \to K^-\pi^+)K^+\pi^-$	1
$\psi(2S) \to (K^{*+} \to K^+\pi^-)(\bar{K}^{*+} \to K^-\pi^+)$	1
$\psi(2S) \to (K_0^{*+} \to K^+\pi^-)K^-\pi^+$	1
$\psi(2S) \to (K_1^+ \to (K_0^{*+} \to K^+\pi^-)\pi^+)K^-$	1
$\psi(2S) \to (K_1^+ \to K^+(\rho^0 \to \pi^+\pi^-))K^-$	1
$\psi(2S) \to K^+(\bar{K}_2^{*+} \to K^-\pi^+\gamma_{\mathrm{FSR}})\pi^-$	1
Total number of background events	806

Table A.9: Background reactions, according to the inclusive MC sample for the $K^+K^-\pi^+\pi^-$ final state, with their corresponding number of events after all selection criteria described in this work.

Reaction	Number of Events
$\psi(2S) \to K^+K^-\pi^+\pi^-$	291
$\psi(2S) \to K^+K^-(\rho^0 \to \pi^+\pi^-)$	116
$\psi(2S) \to K^-(K_2^{*0} \to K^+\pi^-)\pi^+$	24
$\psi(2S) \to K^+(\bar{K}_2^{*0} \to K^-\pi^+)\pi^-$	19
$\psi(2S) \to K^+(\bar{K}^{*0} \to K^-\pi^+)\pi^-$	18
$\psi(2S) \to K^-(K^{*0} \to K^+\pi^-)\pi^+$	16
$\psi(2S) \to (K_2^{*0} \to K^+\pi^-)(\bar{K}_2^{*0} \to K^-\pi^+)$	4
$\psi(2S) \to (K_1^- \to K^-(\rho^0 \to \pi^+\pi^-))K^+$	2
$\psi(2S) \to K^+K^-(\omega \to \pi^+\pi^-)$	2
$\psi(2S) \to K^+K^-(\rho^0 \to \pi^+\pi^-\gamma_{\mathrm{FSR}})$	2
$\psi(2S) \to (\bar{K}_0^{*0} \to K^-\pi^+)(K_2^{*0} \to K^+\pi^-)$	1
$\psi(2S) \to (\bar{K}_0^{*0} \to K^-\pi^+)K^+\pi^-$	1
$\psi(2S) \to (K^{*0} \to K^+\pi^-)(\bar{K}^{*0} \to K^-\pi^+)$	1
$\psi(2S) \to (K_0^{*0} \to K^+\pi^-)K^-\pi^+$	1
$\psi(2S) \to (K_1^+ \to (K_0^{*0} \to K^+\pi^-)\pi^+)K^-$	1
$\psi(2S) \to (K_1^- \to (\bar{K}_0^{*0} \to K^-\pi^+)\pi^-)K^+$	1
$\psi(2S) \to (a_0^0 \to K^+K^-)\pi^+\pi^-$	1
$\psi(2S) \to K^+(\bar{K}_2^{*0} \to K^-\pi^+\gamma_{\mathrm{FSR}})\pi^-$	1
$\psi(2S) \to K^-(K^{*0} \to K^+\pi^-\gamma_{\mathrm{FSR}})\pi^+$	1
Total number of background events	503

$K^+K^-\pi^0\pi^0$ Final State

Table A.10: Signal reactions, according to the inclusive MC sample for the $K^+K^-\pi^0\pi^0$ final state, with their corresponding number of events after all selection criteria described in this work, except for the $K^*(892)$ veto.

Reaction	Number of Events
$\psi(2S) \to (f_0 \to \pi^0\pi^0)(\phi \to K^+K^-)$	667
$\psi(2S) \to (f_0(1710) \to \pi^0\pi^0)(\phi \to K^+K^-)$	39
$\psi(2S) \to (f_2' \to \pi^0\pi^0)(\phi \to K^+K^-)$	5
Total number of signal events	711

Table A.11: Signal reactions, according to the inclusive MC sample for the $K^+K^-\pi^0\pi^0$ final state, with their corresponding number of events after all selection criteria described in this work.

Reaction	Number of Events
$\psi(2S) \to (f_0 \to \pi^0\pi^0)(\phi \to K^+K^-)$	561
$\psi(2S) \to (f_0(1710) \to \pi^0\pi^0)(\phi \to K^+K^-)$	29
$\psi(2S) \to (f_2' \to \pi^0\pi^0)(\phi \to K^+K^-)$	5
Total number of signal events	595

Table A.12: Background reactions, according to the inclusive MC sample for the $K^+K^-\pi^0\pi^0$ final state, with their corresponding number of events after all selection criteria described in this work, except for the $K^*(892)$ veto.

Reaction	Number of Events
$\psi(2S) \to (K^{*+} \to K^+\pi^0)K^-\pi^0$	14
$\psi(2S) \to (K_2^{*+} \to K^-\pi^0)K^+\pi^0$	6
$\psi(2S) \to (K^{*+} \to K^-\pi^0)K^+\pi^0$	5
$\psi(2S) \to (K_2^{*+} \to K^+\pi^0)K^-\pi^0$	3
$\psi(2S) \to (\chi_{c1} \to (J/\psi \to K^+K^-\pi^0)\gamma)\gamma$	1
$\psi(2S) \to (\chi_{c1} \to K^+K^-\pi^0\pi^0)\gamma$	1
$\psi(2S) \to (J/\psi \to K^+K^-\pi^0)\pi^0$	1
$\psi(2S) \to (K_1^+ \to (K_0^{*+} \to K^+\pi^0)\pi^0)K^-$	1
$\psi(2S) \to (K_2^{*+} \to K^+\pi^0)(K_2^{*+} \to K^-\pi^0)$	1
Total number of background events	33

Table A.13: Background reactions, according to the inclusive MC sample for the $K^+K^-\pi^0\pi^0$ final state, with their corresponding number of events after all selection criteria described in this work.

Reaction	Number of Events
$\psi(2S) \to (K_2^{*+} \to K^-\pi^0)K^+\pi^0$	6
$\psi(2S) \to (K_2^{*+} \to K^+\pi^0)K^-\pi^0$	3
$\psi(2S) \to (K^{*+} \to K^+\pi^0)K^-\pi^0$	2
$\psi(2S) \to (\chi_{c1} \to (J/\psi \to K^+K^-\pi^0)\gamma)\gamma$	1
$\psi(2S) \to (\chi_{c1} \to K^+K^-\pi^0\pi^0)\gamma$	1
$\psi(2S) \to (J/\psi \to K^+K^-\pi^0)\pi^0$	1
$\psi(2S) \to (K^{*+} \to K^-\pi^0)K^+\pi^0$	1
$\psi(2S) \to (K_1^+ \to (K_0^{*+} \to K^+\pi^0)\pi^0)K^-$	1
$\psi(2S) \to (K_2^{*+} \to K^+\pi^0)(K_2^{*+} \to K^-\pi^0)$	1
Total number of background events	17

A.2.7 PWA Fit Results

Table A.14: Parameter values and uncertainties resulting from the fit presented in Section 6.2. $\vartheta_{L,S}^{X\to\pi\pi}$ is the phase of the complex canonical amplitude $A_{J_X,0,L,S}^{X\to\pi\pi}$.

Partial Wave	Parameter	Fit Result
S-wave $L=0\ S=1$	$\vartheta_{0,1}^{\text{S-wave}\to\pi^0\pi^0}$	4.190 ± 0.09
	$\vartheta_{0,1}^{\text{S-wave}\to\pi^+\pi^-}$	3.57 ± 0.04
	$\alpha_{0,1}^{f_0(500)}$	$(0 \pm 1) \times 10^{-4}$ GeV
	$\alpha_{0,1}^{f_0(980)}$	(4.79 ± 0.06) GeV
	$\alpha_{0,1}^{f_0(1370)}$	(-2.8 ± 0.1) GeV
	$\alpha_{0,1}^{f_0(1500)}$	(-0.2 ± 0.1) GeV
	$\alpha_{0,1}^{f_0(1710)}$	(-1.8 ± 0.1) GeV
S-wave $L=2\ S=1$	$\vartheta_{2,1}^{\text{S-wave}\to\pi^0\pi^0}$	1.58 ± 0.08
	$\vartheta_{2,1}^{\text{S-wave}\to\pi^+\pi^-}$	0.93 ± 0.04
	$\alpha_{2,1}^{f_0(500)}$	(1.18 ± 0.01) GeV
	$\alpha_{2,1}^{f_0(980)}$	$(0 \pm 2) \times 10^{-4}$ GeV
	$\alpha_{2,1}^{f_0(1370)}$	(-6.5 ± 0.1) GeV
	$\alpha_{2,1}^{f_0(1500)}$	(-2.1 ± 0.1) GeV
	$\alpha_{2,1}^{f_0(1710)}$	(-2.0 ± 0.1) GeV
D-wave $L=0\ S=1$	$\vartheta_{0,1}^{\text{D-wave}\to\pi^+\pi^-}$	5.7 ± 0.1
	$\alpha_{0,1}^{f_2(1270)}$	(0.0 ± 0.4) GeV
	$\alpha_{0,1}^{f_2'(1525)}$	(0.00 ± 0.01) GeV
	$\alpha_{0,1}^{f_2(1810)}$	(-12.6 ± 0.8) GeV
	$\alpha_{0,1}^{f_2(1950)}$	$(0 \pm 1) \times 10^{-3}$ GeV
D-wave $L=2\ S=1$	$\vartheta_{2,1}^{\text{D-wave}\to\pi^0\pi^0}$	7.2 ± 0.1
	$\vartheta_{2,1}^{\text{D-wave}\to\pi^+\pi^-}$	-24.65 ± 0.06
	$\alpha_{2,1}^{f_2(1270)}$	(-1.06 ± 0.03) GeV
	$\alpha_{2,1}^{f_2'(1525)}$	$(0 \pm 2) \times 10^{-3}$ GeV
	$\alpha_{2,1}^{f_2(1810)}$	(14.5 ± 0.5) GeV
	$\alpha_{2,1}^{f_2(1950)}$	$(0 \pm 9) \times 10^{-4}$ GeV

Table A.15: Parameter values and uncertainties resulting from the fit presented in Section 6.2. $\vartheta_{L,S}^{X\to\pi\pi}$ is the phase of the complex canonical amplitude $A_{J_X,0,L,S}^{X\to\pi\pi}$.

Partial Wave	Parameter	Fit Result
D-wave $L=2\ S=2$	$\vartheta_{2,2}^{\text{D-wave}\to\pi^0\pi^0}$	8.3 ± 0.1
	$\vartheta_{2,2}^{\text{D-wave}\to\pi^+\pi^-}$	0.95 ± 0.07
	$\alpha_{2,2}^{f_2(1270)}$	(0.61 ± 0.04) GeV
	$\alpha_{2,2}^{f_2'(1525)}$	(5.3 ± 0.3) GeV
	$\alpha_{2,2}^{f_2(1810)}$	(0.00 ± 0.01) GeV
	$\alpha_{2,2}^{f_2(1950)}$	(0.99 ± 0.09) GeV
D-wave $L=2\ S=3$	$\vartheta_{2,3}^{\text{D-wave}\to\pi^0\pi^0}$	4.0 ± 0.1
	$\vartheta_{2,3}^{\text{D-wave}\to\pi^+\pi^-}$	3.63 ± 0.09
	$\alpha_{2,3}^{f_2(1270)}$	(0.53 ± 0.07) GeV
	$\alpha_{2,3}^{f_2'(1525)}$	(-0.9 ± 0.8) GeV
	$\alpha_{2,3}^{f_2(1810)}$	(13 ± 1) GeV
	$\alpha_{2,3}^{f_2(1950)}$	(0.0 ± 0.2) GeV
D-wave $L=4\ S=3$	$\vartheta_{4,3}^{\text{D-wave}\to\pi^0\pi^0}$	5.2 ± 0.1
	$\vartheta_{4,3}^{\text{D-wave}\to\pi^+\pi^-}$	-7.98 ± 0.08
	$\alpha_{4,3}^{f_2(1270)}$	(-3.04 ± 0.07) GeV
	$\alpha_{4,3}^{f_2'(1525)}$	$(0 \pm 1) \times 10^{-3}$ GeV
	$\alpha_{4,3}^{f_2(1810)}$	(0.00 ± 0.02) GeV
	$\alpha_{4,3}^{f_2(1950)}$	(2.7 ± 0.1) GeV
Non-resonant S-wave	$\tilde{b}_{\pi\pi}^{(0)}$	-0.106 ± 0.006
	$\tilde{b}_{\pi\pi}^{(1)}$	(-0.017 ± 0.004) GeV^{-2}
	$\tilde{b}_{\pi\pi}^{(2)}$	(-0.0184 ± 0.0007) GeV^{-4}
Non-resonant D-wave	$\tilde{b}'_{\pi\pi}$	0.08 ± 0.04
Scaling factor	W	0.621 ± 0.008
Negative logarithmic likelihood	$-\ln\mathcal{L}_{\pi^+\pi^-}$	-38201
	$-\ln\mathcal{L}_{\pi^0\pi^0}$	-10245
	$-\ln\mathcal{L}_{\text{tot}}$	-48446

A.3 Figures

A.3.1 3D Complex Square Root

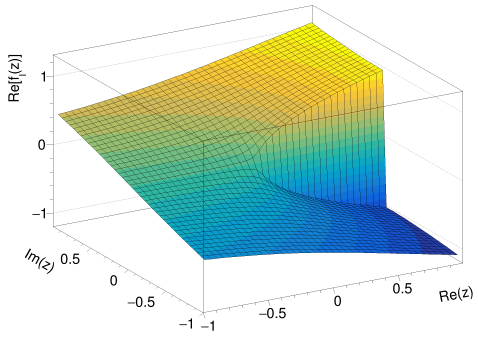

(a) 1st branch - real part

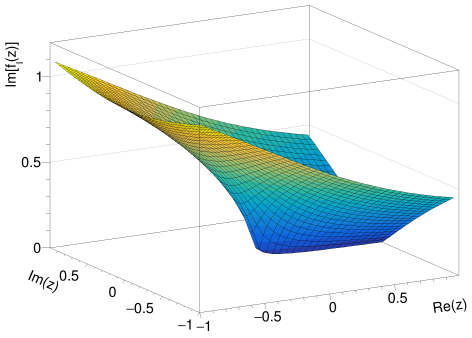

(b) 1st branch - imaginary part

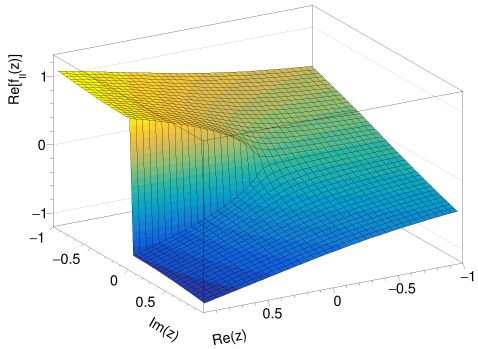

(c) 2nd branch - real part

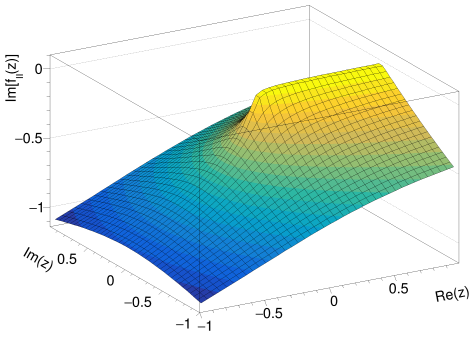

(d) 2nd branch - imaginary part

Figure A.1: 3d depiction of the real and imaginary part of the two branches $f_{\mathrm{I}}(z)$ and $f_{\mathrm{II}}(z)$ of the square root functions for complex arguments. The 2d projection can be seen in Fig. 3.3.

A.3.2 Polar Angle of π^+ in the $\pi^+\pi^-$ Helicity Frame

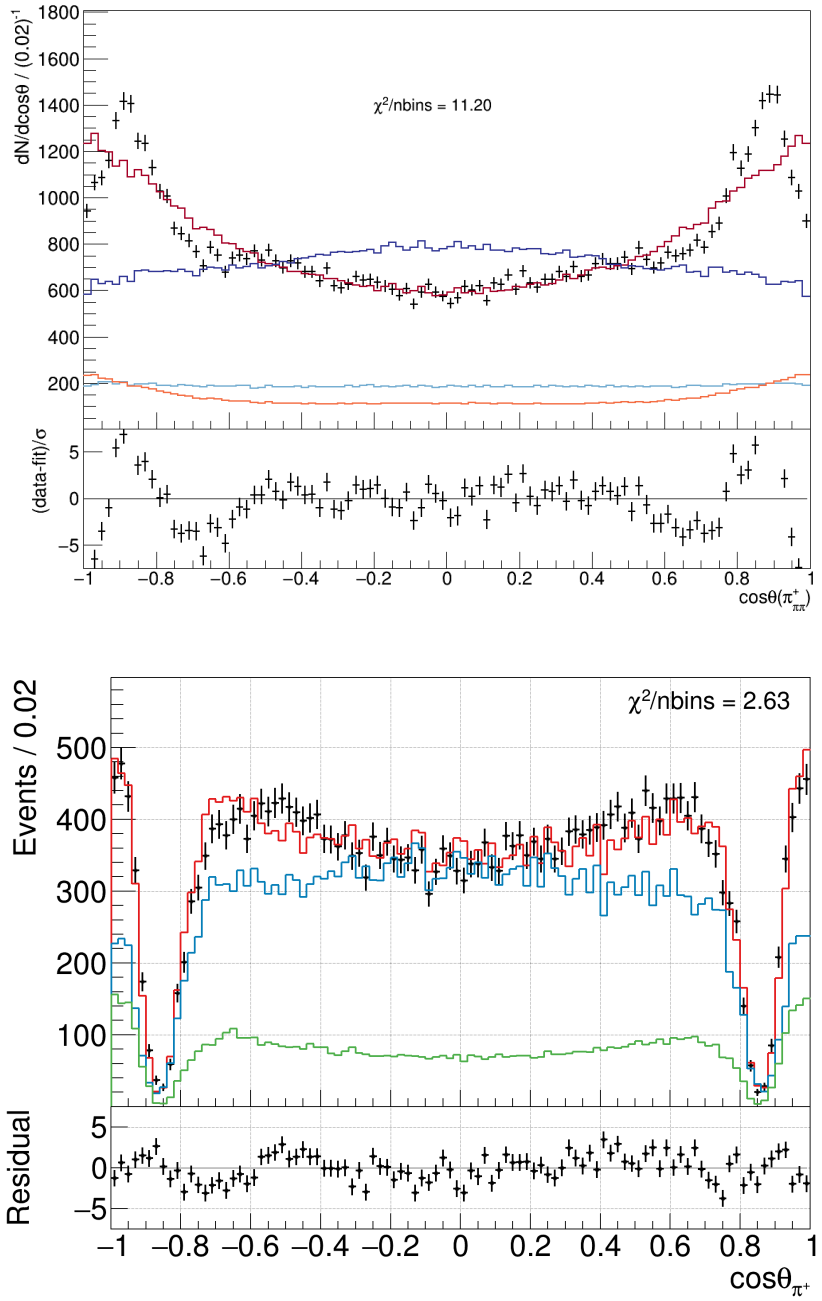

Figure A.2: Distribution of the cosine of the polar helicity angle θ in the $\pi^+\pi^-$ helicity frame, before (left) and after (right) the implementation of the $K^*(892)$ veto. Data is shown in black, while the projections of two partial wave analyses, which are redundant for this comparison, are shown in color.

Bibliography

[1] S. Berryman. *Ancient Atomism (Stanford Encyclopedia of Philosophy/Fall 2008 Edition)*. Oct. 18, 2005. URL: https://plato.stanford.edu/archives/fall2008/entries/atomism-ancient/ (visited on 02/06/2023).

[2] J.J. Thomson. "XL. Cathode Rays." In: *The London, Edinburgh, and Dublin Philosophical Magazine and Journal of Science* 5.44 (Oct. 1897), pp. 293–316. URL: https://books.google.de/books?id=orp%5C_EP-lkzoC.

[3] J.J. Thomson. "XXIV. On the structure of the atom: an investigation of the stability and periods of oscillation of a number of corpuscles arranged at equal intervals around the circumference of a circle; with application of the results to the theory of atomic structure." In: *The London, Edinburgh, and Dublin Philosophical Magazine and Journal of Science* 7.39 (Mar. 1904), pp. 237–265. DOI: 10.1080/14786440409463107. URL: http://dx.doi.org/10.1080/14786440409463107.

[4] E. Rutherford. "LXXIX. The scattering of α and β particles by matter and the structure of the atom." In: *The London, Edinburgh, and Dublin Philosophical Magazine and Journal of Science* 21.125 (May 1911), pp. 669–688. DOI: 10.1080/14786440508637080. URL: http://dx.doi.org/10.1080/14786440508637080.

[5] A. Romer. "Proton or prouton?: Rutherford and the depths of the atom." In: *American Journal of Physics* 65.8 (Aug. 1997), pp. 707–716. DOI: 10.1119/1.18640. URL: http://dx.doi.org/10.1119/1.18640.

[6] J. Chadwick. "The existence of a neutron." In: *Proceedings of the Royal Society of London. Series A, Containing Papers of a Mathematical and Physical Character* 136.830 (June 1932), pp. 692–708. DOI: 10.1098/rspa.1932.0112. URL: http://dx.doi.org/10.1098/rspa.1932.0112.

[7] H. Yukawa. "On the Interaction of Elementary Particles. I." In: *Proceedings of the Physico-Mathematical Society of Japan. 3rd Series* 17 (1935), pp. 48–57. DOI: 10.11429/ppmsj1919.17.0_48.

[8] C. Lattes et al. “Processes Involving Charged Mesons.” In: *Nature* 159.4047 (May 1947), pp. 694–697. DOI: 10.1038/159694a0. URL: http://dx.doi.org/10.1038/159694a0.

[9] G.D. Rochester and C.C. Butler. “Evidence for the Existence of New Unstable Elementary Particles.” In: *Nature* 160.4077 (Dec. 1947), pp. 855–857. DOI: 10.1038/160855a0. URL: http://dx.doi.org/10.1038/160855a0.

[10] V.D. Hopper and S. Biswas. “Evidence Concerning the Existence of the New Unstable Elementary Neutral Particle.” In: *Physical Review* 80.6 (Dec. 15, 1950), pp. 1099–1100. DOI: 10.1103/physrev.80.1099. URL: http://dx.doi.org/10.1103/physrev.80.1099.

[11] M. Gell-Mann. “Isotopic Spin and New Unstable Particles.” In: *Physical Review* 92.3 (Nov. 1, 1953), pp. 833–834. DOI: 10.1103/physrev.92.833. URL: http://dx.doi.org/10.1103/physrev.92.833.

[12] T. Nakano and K. Nishijima. “Charge Independence for V-particles.” In: *Progress of Theoretical Physics* 10.5 (Nov. 1953), pp. 581–582. DOI: 10.1143/ptp.10.581. URL: http://dx.doi.org/10.1143/ptp.10.581.

[13] M. Gell-Mann. “The Eightfold Way: A Theory of Strong Interaction Symmetry.” In: *Technical Report* (Mar. 15, 1961). DOI: 10.2172/4008239. URL: http://dx.doi.org/10.2172/4008239.

[14] M. Gell-Mann. “A schematic model of baryons and mesons.” In: *Physics Letters* 8.3 (Feb. 1964), pp. 214–215. DOI: 10.1016/s0031-9163(64)92001-3. URL: http://dx.doi.org/10.1016/s0031-9163(64)92001-3.

[15] J.J. Aubert et al. “Experimental Observation of a Heavy Particle J.” In: *Physical Review Letters* 33.23 (Dec. 2, 1974), pp. 1404–1406. DOI: 10.1103/physrevlett.33.1404. URL: http://dx.doi.org/10.1103/physrevlett.33.1404.

[16] J.E. Augustin et al. “Discovery of a Narrow Resonance in e^+e^- Annihilation.” In: *Physical Review Letters* 33.23 (Dec. 2, 1974), pp. 1406–1408. DOI: 10.1103/physrevlett.33.1406. URL: http://dx.doi.org/10.1103/physrevlett.33.1406.

[17] B. Bjørken and S. Glashow. “Elementary particles and SU(4).” In: *Physics Letters* 11.3 (Aug. 1964), pp. 255–257. DOI: 10.1016/0031-9163(64)90433-0. URL: http://dx.doi.org/10.1016/0031-9163(64)90433-0.

[18] *BES3 Collaboration Information*. URL: https://docbes3.ihep.ac.cn/bes3shift_db/bes3member/institution.php (visited on 02/07/2023).

[19] Y. Wang. “Preface: special topic on physics of the BESIII experiment.” In: *National Science Review* 8.11 (Nov. 2021). DOI: 10.1093/nsr/nwab201. URL: http://dx.doi.org/10.1093/nsr/nwab201.

[20] M.H. Johnson and E. Teller. "Classical Field Theory of Nuclear Forces." In: *Physical Review* 98.3 (May 1, 1955), pp. 783–787. DOI: 10.1103/physrev.98.783. URL: http://dx.doi.org/10.1103/physrev.98.783.

[21] J.R. Peláez. "From controversy to precision on the sigma meson: A review on the status of the non-ordinary $f_0(500)$ resonance." In: *Physics Reports* 658 (Nov. 2016), pp. 1–111. DOI: 10.1016/j.physrep.2016.09.001. URL: http://dx.doi.org/10.1016/j.physrep.2016.09.001.

[22] G. 't Hooft et al. "A theory of scalar mesons." In: *Physics Letters B* 662.5 (May 2008), pp. 424–430. DOI: 10.1016/j.physletb.2008.03.036. URL: http://dx.doi.org/10.1016/j.physletb.2008.03.036.

[23] T. Kojo and D. Jido. "Sigma meson in pole-dominated QCD sum rules." In: *Physical Review D* 78.11 (Dec. 4, 2008). DOI: 10.1103/physrevd.78.114005. URL: http://dx.doi.org/10.1103/physrevd.78.114005.

[24] Y. Chen et al. "Glueball spectrum and matrix elements on anisotropic lattices." In: *Physical Review D* 73.1 (Jan. 26, 2006). DOI: 10.1103/physrevd.73.014516. URL: http://dx.doi.org/10.1103/physrevd.73.014516.

[25] R.M. Dreizler, T. Kirchner, and C.S. Lüdde. *Streutheorie in der nichtrelativistischen Quantenmechanik. Eine Einführung*. New York, United States: Springer Publishing, 2018.

[26] I.J.R. Aitchison. "Unitarity, Analyticity and Crossing Symmetry in Two- and Three-hadron Final State Interactions." In: *arXiv: High Energy Physics - Phenomenology* (July 9, 2015). URL: https://arxiv.org/pdf/1507.02697.pdf.

[27] S. Scherer. *Symmetrien und Gruppen in der Teilchenphysik*. New York, United States: Springer Publishing, 2015.

[28] O. Philipsen. *Quantenfeldtheorie und das Standardmodell der Teilchenphysik. Eine Einführung*. New York, United States: Springer Publishing, 2018.

[29] W. Demtröder. *Experimentalphysik 4. Kern-, Teilchen- und Astrophysik*. New York, United States: Springer Publishing, 2017.

[30] MissMJ and Cush. *Standard Model of Elementary Particles*. Sept. 17, 2019. URL: https://commons.wikimedia.org/w/index.php?curid=4286964 (visited on 12/29/2022).

[31] R.L. Workman et al. "Review of Particle Physics." In: *Progress of Theoretical and Experimental Physics* 2022.8 (Aug. 2022). DOI: 10.1093/ptep/ptac097. URL: http://dx.doi.org/10.1093/ptep/ptac097.

[32] C. Berger. *Elementarteilchenphysik: Von den Grundlagen zu den modernen Experimenten (Springer-Lehrbuch)*. 3rd ed. Springer Spektrum, Sept. 3, 2014.

[33] W. Lee and D. Weingarten. "Scalar quarkonium masses and mixing with the lightest scalar glueball." In: *Physical Review D* 61.1 (Dec. 10, 1999). DOI: 10.1103/physrevd.61.014015. URL: http://dx.doi.org/10.1103/physrevd.61.014015.

[34] C.J. Morningstar and M. Peardon. "Efficient glueball simulations on anisotropic lattices." In: *Physical Review D* 56.7 (Oct. 1, 1997), pp. 4043–4061. DOI: 10.1103/physrevd.56.4043. URL: http://dx.doi.org/10.1103/physrevd.56.4043.

[35] G.S. Bali et al. "A comprehensive lattice study of SU(3) glueballs." In: *Physics Letters B* 309.3-4 (July 15, 1993), pp. 378–384. DOI: 10.1016/0370-2693(93)90948-h.

[36] W.I. Eshraim and C.S. Fischer. "Hadronic decays of the (pseudo-)scalar charmonium states η_c and χ_{c0} in the extended Linear Sigma Model." In: *The European Physical Journal A* 54.8 (Aug. 2018). DOI: 10.1140/epja/i2018-12569-3. URL: http://dx.doi.org/10.1140/epja/i2018-12569-3.

[37] F. Close and A. Kirk. "Scalar glueball-$q\bar{q}$ mixing above 1 GeV and implications for lattice QCD." In: *The European Physical Journal C* 21.3 (July 2001), pp. 531–543. DOI: 10.1007/s100520100748. URL: http://dx.doi.org/10.1007/s100520100748.

[38] C. Huygens. *Traité de la lumière (Treatise on Light). In which are explained the causes of that which occurs in reflexion, & in refraction and particularly in the strange refraction of Iceland crystal*. Van der Aa, Jan. 18, 2005. URL: https://www.gutenberg.org/ebooks/14725.

[39] M. Abramowitz and I.A. Stegun. *Handbook of Mathematical Functions (Dover Books on Mathematics): With Formulas, Graphs, and Mathematical Tables*. 9th Revised ed. Dover Publications Inc., June 30, 1965.

[40] J.R. Taylor. *Scattering Theory: The Quantum Theory of Nonrelativistic Collisions (Dover Books on Engineering)*. Dover Publications Inc., May 26, 2006.

[41] M. Born and V. Fock. "Beweis des Adiabatensatzes." In: *Zeitschrift für Physik* 51.3-4 (Mar. 1928), pp. 165–180. DOI: 10.1007/bf01343193. URL: http://dx.doi.org/10.1007/bf01343193.

[42] S. Mandelstam. "Determination of the Pion-Nucleon Scattering Amplitude from Dispersion Relations and Unitarity. General Theory." In: *Physical Review* 112.4 (Nov. 15, 1958), pp. 1344–1360. DOI: 10.1103/physrev.112.1344. URL: http://dx.doi.org/10.1103/physrev.112.1344.

[43] R. Sinha. *Real and Complex Analysis: Volume 2 (English Edition)*. 1st ed. 2018. Springer, Nov. 22, 2018.

[44] J. Eells. *Complex Analysis: Proceedings of the Summer School. Held at the International Centre for Theoretical Physics, Trieste, July 5 - 30, 1980 (Lecture Notes in Mathematics, 950, Band 950)*. 1982nd ed. Springer, Feb. 22, 2009.

[45] L. Kaldamäe and S. Groote. "Virtual and real processes, the Källén function, and the relation to dilogarithms." In: *Journal of Physics G: Nuclear and Particle Physics* 42.8 (July 10, 2015), p. 085003. DOI: 10.1088/0954-3899/42/8/085003. URL: http://dx.doi.org/10.1088/0954-3899/42/8/085003.

[46] S. Flatté. "Coupled-channel analysis of the $\pi\eta$ and $K\bar{K}$ systems near $K\bar{K}$ threshold." In: *Physics Letters B* 63.2 (July 1976), pp. 224–227. DOI: 10.1016/0370-2693(76)90654-7. URL: http://dx.doi.org/10.1016/0370-2693(76)90654-7.

[47] J.L. Basdevant and E.L. Berger. "Unitary coupled-channel analysis of diffractive production of the A_1 resonance." In: *Physical Review D* 16.3 (Aug. 1, 1977), pp. 657–678. DOI: 10.1103/physrevd.16.657. URL: http://dx.doi.org/10.1103/physrevd.16.657.

[48] J. Richman. "An Experimenter's Guide to the Helicity Formalism." In: *DOE reasearch and development report* (June 1, 1984). URL: https://inspirehep.net/literature/202987.

[49] S. Chung. *Spin formalisms; 3nd. updated version*. NY, us: Brookhaven Nat. Lab., 2013. URL: https://cds.cern.ch/record/1561144.

[50] *Beijing Electron Positron Collider (BEPCII)*. URL: lssf.cas.cn/en/facilities-view.jsp?id=ff8080814ff56599014ff5a8f2680059 (visited on 01/09/2023).

[51] M. Ablikim et al. "Design and construction of the BESIII detector." In: *Nuclear Instruments and Methods in Physics Research Section A: Accelerators, Spectrometers, Detectors and Associated Equipment* 614.3 (Mar. 2010), pp. 345–399. DOI: 10.1016/j.nima.2009.12.050. URL: http://dx.doi.org/10.1016/j.nima.2009.12.050.

[52] M. Ablikim et al. "Future Physics Programme of BESIII *." In: *Chinese Physics C* 44.4 (Mar. 26, 2020), p. 040001. DOI: 10.1088/1674-1137/44/4/040001. URL: https://doi.org/10.1088/1674-1137/44/4/040001.

[53] C. Yu et al. "BEPCII Performance and Beam Dynamics Studies on Luminosity." In: *7th International Particle Accelerator Conference (IPAC'16), Busan, Korea, May 8-13, 2016* (June 16, 2016), pp. 1014–1018. DOI: 10.18429/jacow-ipac2016-tuya01. URL: http://inspirehep.net/record/1469857.

[54] F.A. Harris. "BEPCII and BESIII." In: *International Journal of Modern Physics A* 24.02n03 (Jan. 30, 2009), pp. 377–384. DOI: 10.1142/s0217751x09043705. URL: http://dx.doi.org/10.1142/s0217751x09043705.

[55] X. Li et al. "Study of MRPC technology for BESIII endcap-TOF upgrade." In: *Radiation detection technology and methods* 1.2 (Dec. 1, 2017). DOI: 10.1007/s41605-017-0014-2.

[56] X. Jiang et al. "Supporting Multiple Concurrent Usage Patterns on the HTCondor-Based HTC Computing System at IHEP." In: *Proceedings of International Symposium on Grids* (Sept. 28, 2022). DOI: 10.22323/1.415.0010. URL: http://dx.doi.org/10.22323/1.415.0010.

[57] G. Barrand et al. “GAUDI — A software architecture and framework for building HEP data processing applications.” In: *Computer Physics Communications* 140.1-2 (Oct. 2001), pp. 45–55. DOI: 10.1016/s0010-4655(01)00254-5. URL: http://dx.doi.org/10.1016/s0010-4655(01)00254-5.

[58] W.D. Li, Y.J. Mao, and Y.F. Wang. “Chapter 2 The BES-III Detector and Offline Software.” In: *International Journal of Modern Physics A* 24.supp01 (May 2009), pp. 9–21. DOI: 10.1142/s0217751x09046424. URL: http://dx.doi.org/10.1142/s0217751x09046424.

[59] S. Jadach, B. Ward, and Z. Wąs. “The precision Monte Carlo event generator for two-fermion final states in collisions.” In: *Computer Physics Communications* 130.3 (Aug. 2000), pp. 260–325. DOI: 10.1016/s0010-4655(00)00048-5. URL: http://dx.doi.org/10.1016/s0010-4655(00)00048-5.

[60] P. Rong-Gang. “Event generators at BESIII.” In: *Chinese Physics C* 32.8 (Aug. 2008), pp. 599–602. DOI: 10.1088/1674-1137/32/8/001. URL: http://dx.doi.org/10.1088/1674-1137/32/8/001.

[61] S. Agostinelli et al. “Geant4—a simulation toolkit.” In: *Nuclear Instruments and Methods in Physics Research Section A: Accelerators, Spectrometers, Detectors and Associated Equipment* 506.3 (July 2003), pp. 250–303. DOI: 10.1016/s0168-9002(03)01368-8. URL: http://dx.doi.org/10.1016/s0168-9002(03)01368-8.

[62] Z. Deng et al. “Object-oriented BESIII detector simulation system.” In: *Chinese Physics C* 30.5 (May 5, 2006), pp. 371–377. URL: http://cpc.ihep.ac.cn/article/id/283d17c0-e8fa-4ad7-bfe3-92095466def1.

[63] C. Lui, W. Song, and Z. Wang. *Determination of the number of psi(3686) events taken in 2021 at BESIII*. Nov. 22, 2022. URL: https://docbes3.ihep.ac.cn/cgi-bin/DocDB/ShowDocument?docid=1204 (visited on 01/02/2023).

[64] D.J. Lange. “The EvtGen particle decay simulation package.” In: *Nuclear Instruments and Methods in Physics Research Section A: Accelerators, Spectrometers, Detectors and Associated Equipment* 462.1-2 (Apr. 2001), pp. 152–155. DOI: 10.1016/s0168-9002(01)00089-4. URL: http://dx.doi.org/10.1016/s0168-9002(01)00089-4.

[65] R.L. Yang, R.G. Ping, and H. Chen. “Tuning and Validation of the Lundcharm Model with J/psi Decays.” In: *Chinese Physics Letters* 31.6 (June 2014), p. 061301. DOI: 10.1088/0256-307x/31/6/061301. URL: http://dx.doi.org/10.1088/0256-307x/31/6/061301.

[66] J.C. Chen et al. “Event generator for J/ψ and $\psi(2S)$ decay.” In: *Physical Review D* 62.3 (June 23, 2000). DOI: 10.1103/physrevd.62.034003. URL: http://dx.doi.org/10.1103/physrevd.62.034003.

[67] R. Brun and F. Rademakers. "ROOT — An object oriented data analysis framework." In: *Nuclear Instruments and Methods in Physics Research Section A: Accelerators, Spectrometers, Detectors and Associated Equipment* 389.1-2 (Apr. 1997), pp. 81–86. DOI: 10.1016/s0168-9002(97)00048-x. URL: http://dx.doi.org/10.1016/s0168-9002(97)00048-x.

[68] *ROOT*. Comp. software. Version v6.22/02. Aug. 17, 2020. URL: https://github.com/root-project/root/tree/v6-22-02.

[69] B. Kopf et al. "Partial wave analysis for $\bar{p}p$ and e^+e^- annihilation processes." In: *Hyperfine Interactions* 229.1-3 (Feb. 19, 2014), pp. 69–74. DOI: 10.1007/s10751-014-1039-2. URL: http://dx.doi.org/10.1007/s10751-014-1039-2.

[70] F. James and M. Roos. "Minuit - a system for function minimization and analysis of the parameter errors and correlations." In: *Computer Physics Communications* 10.6 (Dec. 1975), pp. 343–367. DOI: 10.1016/0010-4655(75)90039-9. URL: http://dx.doi.org/10.1016/0010-4655(75)90039-9.

[71] F. James and M. Winkler. *MINUIT2*. Comp. software. Version 5.34.14. Nov. 5, 2018. URL: https://github.com/GooFit/Minuit2.

[72] M.L. Mangano. "Introduction to QCD." In: *2001 CERN - CLAF School of High-energy Physics* (2001), pp. 41–84. DOI: 10.5170/CERN-1999-004.53. URL: 10.5170/CERN-2003-003.41.

[73] A. Deur, S. J. Brodsky, and G. F. de Téramond. "The QCD running coupling." In: *Progress in Particle and Nuclear Physics* 90 (Sept. 2016), pp. 1–74. DOI: 10.1016/j.ppnp.2016.04.003. URL: http://dx.doi.org/10.1016/j.ppnp.2016.04.003.

[74] J. Bloms. "From Exotic Charmonia to Scalar Glueballs."

[75] G. Fubini. "Sugli integrali multipli." Italian. In: *Rom. Acc. L. Rend. (5)* 16.1 (1907), pp. 608–614. ISSN: 0001-4435.

[76] H. Albrecht et al. "Search for hadronic $b \to u$ decays." In: *Physics Letters B* 241.2 (May 1990), pp. 278–282. DOI: 10.1016/0370-2693(90)91293-k. URL: http://dx.doi.org/10.1016/0370-2693(90)91293-k.

[77] M. Ablikim et al. "Study of $J/\psi \to p\bar{p}\phi$ at BESIII." In: *Physical Review D* 93.5 (Mar. 18, 2016). DOI: 10.1103/physrevd.93.052010. URL: http://dx.doi.org/10.1103/physrevd.93.052010.

[78] M. Ablikim et al. "Search for η and $\eta' \to \pi^+e^-\bar{\nu}_e + c.c.$ decays in $J/\psi \to \phi\eta$ and $\phi\eta'$." In: *Physical Review D* 87.3 (Feb. 15, 2013). DOI: 10.1103/physrevd.87.032006. URL: http://dx.doi.org/10.1103/physrevd.87.032006.

[79] M. Ablikim et al. "Observation of the electromagnetic doubly OZI-suppressed decay $J/\psi \to \phi\pi^0$." In: *Physical Review D* 91.11 (June 1, 2015). DOI: 10.1103/physrevd.91.112001. URL: http://dx.doi.org/10.1103/physrevd.91.112001.

[80] L. Wu. "Charmonium at BESIII." In: *EPJ Web of Conferences* 212 (2019). Ed. by M. Achasov, F. Ignatov, and P. Krokovny, p. 02007. DOI: 10.1051/epjconf/201921202007. URL: http://dx.doi.org/10.1051/epjconf/201921202007.

[81] A. V. Anisovich et al. *Three-Particle Physics and Dispersion Relation Theory*. World Scientific, 2013. DOI: 10.1142/8779. eprint: https://www.worldscientific.com/doi/pdf/10.1142/8779. URL: https://www.worldscientific.com/doi/abs/10.1142/8779.

[82] J. Link et al. "Dalitz plot analysis of the $D^+ \to K^-\pi^+\pi^+$ decay in the FOCUS experiment." In: *Physics Letters B* 653.1 (Sept. 2007), pp. 1–11. DOI: 10.1016/j.physletb.2007.06.070. URL: http://dx.doi.org/10.1016/j.physletb.2007.06.070.

[83] V. Bernard, N. Kaiser, and U.G. Meißner. "πK scattering in chiral perturbation theory to one loop." In: *Nuclear Physics B* 357.1 (June 1991), pp. 129–152. DOI: 10.1016/0550-3213(91)90461-6. URL: http://dx.doi.org/10.1016/0550-3213(91)90461-6.

[84] G. Rupp. "Scalar mesons and Adler zeros." In: *AIP Conference Proceedings* (2005). DOI: 10.1063/1.1920993. URL: http://dx.doi.org/10.1063/1.1920993.

[85] B. Kopf et al. "Investigation of the lightest hybrid meson candidate with a coupled-channel analysis of $\bar{p}p$-, $\pi^- p$- and $\pi\pi$-Data." In: *The European Physical Journal C* 81.12 (Dec. 2021). DOI: 10.1140/epjc/s10052-021-09821-2. URL: http://dx.doi.org/10.1140/epjc/s10052-021-09821-2.

[86] M. Albrecht et al. "Coupled channel analysis of $\bar{p}p \to \pi^0\pi^0\eta$, $\pi^0\eta\eta$ and $K^+K^-\pi^0$ at 900 MeV/c and of $\pi\pi$-scattering data." In: *The European Physical Journal C* 80.5 (May 2020). DOI: 10.1140/epjc/s10052-020-7930-x. URL: http://dx.doi.org/10.1140/epjc/s10052-020-7930-x.

[87] J. Augustin et al. "Study of the J/ψ decay into five pions." In: *Nuclear Physics B* 320.1 (June 1989), pp. 1–19. DOI: 10.1016/0550-3213(89)90208-3. URL: http://dx.doi.org/10.1016/0550-3213(89)90208-3.

[88] D.M. Li, H. Yu, and Q.X. Shen. "Properties of the tensor mesons $f_2(1270)$ and $f_2'(1525)$." In: *Journal of Physics G: Nuclear and Particle Physics* 27.4 (Mar. 14, 2001), pp. 807–813. DOI: 10.1088/0954-3899/27/4/305. URL: http://dx.doi.org/10.1088/0954-3899/27/4/305.

[89] R.A. Briceño et al. "Isoscalar $\pi\pi$, $K\bar{K}$, $\eta\eta$ scattering and the σ, f_0, f_2 mesons from QCD." In: *Physical Review D* 97.5 (Mar. 23, 2018). DOI: 10.1103/physrevd.97.054513. URL: http://dx.doi.org/10.1103/physrevd.97.054513.

[90] A. Deandrea et al. "The $s\bar{s}$ and $K\bar{K}$ nature of $f_0(980)$ in D_s decays." In: *arXiv: High Energy Physics - Phenomenology* (Dec. 11, 2000). URL: https://arxiv.org/pdf/hep-ph/0012120.

[91] J.T. Daub, C. Hanhart, and B. Kubis. "A model-independent analysis of final-state interactions in $\bar{B}^0_{d/s} \to J/\psi\pi\pi$." In: *Journal of High Energy Physics* 2016.2 (Feb. 2016). DOI: 10.1007/jhep02(2016)009. URL: http://dx.doi.org/10.1007/jhep02(2016)009.

[92] S. Ropertz, C. Hanhart, and B. Kubis. "A new parametrization for the scalar pion form factors." In: *The European Physical Journal C* 78.12 (Dec. 2018). DOI: 10.1140/epjc/s10052-018-6416-6. URL: http://dx.doi.org/10.1140/epjc/s10052-018-6416-6.

[93] A.A. Neath and J.E. Cavanaugh. "The Bayesian information criterion: background, derivation, and applications." In: *WIREs Computational Statistics* 4.2 (Dec. 14, 2011), pp. 199–203. DOI: 10.1002/wics.199. URL: http://dx.doi.org/10.1002/wics.199.

[94] J.E. Cavanaugh and A.A. Neath. "The Akaike information criterion: Background, derivation, properties, application, interpretation, and refinements." In: *WIREs Computational Statistics* 11.3 (Mar. 14, 2019). DOI: 10.1002/wics.1460. URL: http://dx.doi.org/10.1002/wics.1460.

[95] *PWA Frameworks — Partial Wave Analysis*. URL: https://pwa.readthedocs.io/software.html.

[96] G. Breit and E. Wigner. "Capture of Slow Neutrons." In: *Physical Review* 49.7 (Apr. 1, 1936), pp. 519–531. DOI: 10.1103/physrev.49.519. URL: http://dx.doi.org/10.1103/physrev.49.519.

[97] S.U. Chung et al. "Partial wave analysis in K-matrix formalism." In: *Annalen der Physik* 507.5 (1995), pp. 404–430. DOI: 10.1002/andp.19955070504. URL: http://dx.doi.org/10.1002/andp.19955070504.

Danksagung

An dieser Stelle möchte ich einmal bei all denjenigen bedanken die diese Arbeit möglich gemacht haben.

Zuerst möchte ich allen meinen Eltern für ihre Unterstützung danken, ohne die weder diese Arbeit noch mein Studium in dieser Form möglich gewesen wäre. Ich kann euch nicht genug danken für die Freiheit, die ihr mir gegeben habt und hoffe nur das ihr wisst, wie großartig ihr seid.

Ebenso möchte ich mich bei all den tollen Menschen aus der Arbeitsgruppe bedanken. Der Austausch mit euch hat mich stehts weitergebracht und gute Stimmung, die ihr verbreitet habt, hat mir immer geholfen neue Motivation zu finden. Ich habe meine Zeit in der Gruppe sehr genossen, und freu mich auch weiterhin mit euch zusammenarbeiten zu dürfen.

Besonders bedanken möchte ich an dieser Stelle bei Prof. Alfons Khoukaz, der mich in die Arbeitsgruppe aufgenommen hat und mich seit der Bachelorarbeit unterstützt. Vielen Dank, dass sie stehts ein offenes Ohr für mich hatten und mir die Zeit und die Freiheit gegeben haben, die die Erstellung dieser Arbeit möglich gemacht haben.

Ein großes Dankeschön gebührt auch sowohl Anja als auch Frederik, die mir nicht nur immer mit Rat und Tat zur Seite standen, sondern auch maßgeblich durch ihre Korrekturen zu dieser Arbeit beigetragen haben.

Abschließend möchte ich mich noch ganz herzlich bei meinen Freunden bedanken, die mich stehts unterstützt haben und mir die Möglichkeit gegeben haben mal Abzuschalten und an was anderes zu denken als die Uni. Das ihr trotz (teilweise) größerer Distanzen und meiner Verplantheit an meiner Seite geblieben seid bedeutet mir die Welt. Und danke Lois.

Declaration of Academic Integrity

I hereby confirm that this thesis on "*Partial Wave Analysis of f_J-Resonances via the $\phi\pi\pi$ Final State in $\psi(2S)$ Decays at BESIII*" is solely my own work and that I have used no sources or aids other than the ones stated. All passages in my thesis for which other sources, including electronic media, have been used, be it direct quotes or content references, have been acknowledged as such and the sources cited.

_____

(date and signature of student)

I agree to have my thesis checked in order to rule out potential similarities with other works and to have my thesis stored in a database for this purpose.

_____

(date and signature of student)